NUMERICAL MODELING OF THE ARTIFICIAL DESTRATIFICATION OF THE THERMALLY STRATIFIED WATER COLUMN BY AIR DIFFUSERS

A Thesis Submitted to
the Graduate School of
İzmir Institute of Technology
in Partial Fulfillment of the Requirements for Degree of

MASTER OF SCIENCE

In Civil Engineering

by

Nisa BAHADIROĞLU

December 2021
İZMİR

dedicated to my lovely mom and dad,

Naciye & Hakan Bahadıroğlu

ACKNOWLEDGMENT

I would like to express my sincere thanks to my advisor Prof. Dr. Şebnem Elçi. She has always been patient and understanding and has never lost her faith in me. I realized how lucky I am that she guided me and was always by my side.

I would like to thank Mr. Oğuz Hazar and Ms. Derya Karakaya for their contributions to experimental studies.

I would like to express my heartfelt thanks to my beloved mom (Mrs. Naciye Bahadıroğlu) and dad (Mr. Hakan Bahadıroğlu). I will never be able to express in words my gratitude and love for them. I have never felt alone in a minute, even though we have been miles apart for years. And also, I want to thank my not so little brother Mr. Elçibey Bahadıroğlu who always cheer me up with his energy.

I would also like to thank Ms. Ezgi Yavuz, who I love very much, for always listening and calming me down. She is more than a sister to me, and I know that even the most terrible times mean nothing when we have each other.

My dear friend Mr. Bahadır Öztürk, whose existence is very meaningful to me, I am so lucky to have a friend like you. He had always been there, and I know that he always will be for me when I need him. Also, I would like to thank my lovely friend Ms. Merve Özkahya. She has always tried her best to support me and be by my side.

ABSTRACT

NUMERICAL MODELING OF THE ARTIFICIAL DESTRATIFICATION OF THE THERMALLY STRATIFIED WATER COLUMN BY AIR DIFFUSERS

Reservoirs have essential roles in water management due to the large areas of use. In a reservoir, the structure of the temperature profile in the vertical water column mainly controls the vertical distribution of heat, dissolved substances, and nutrients. Thermal stratification in the water column can lead to an anoxic and poor quality water source. Artificial destratification has been widely used to improve water quality in thermally stratified water sources.

This study focuses on the numerical modeling of artificial destratification of thermally stratified water columns by air diffusers to improve the water quality of reservoirs.

Firstly, destratification experiments were performed to verify the numerical models. In the experiments, the effects of air diffuser hole diameter, air flow rate, and the number and configuration of holes on the diffuser on destratification time and efficiency were observed.

The second part of the study comprised the numerical modeling of hydrodynamics during the destratification of thermally stratified water columns by air diffusers. ANSYS Fluent software is utilized for the simulation of the hydrodynamic processes. Model options for multiphase flows, boundary conditions, and turbulence; and their comparison with experimental studies are discussed. The Eulerian multiphase model and k-ω turbulence model were found to be suitable for this study.

In the final part, the numerical model was verified with the experiments. Based on the error analysis of comparisons of the model and observations, the best configuration of air diffuser is proposed, and the numerical model was found to be successful in simulating the destratification of thermally stratified water columns by air diffuser.

ÖZET

ISIL TABAKALI SU KOLONLARININ HAVA DİFÜZÖRÜ İLE YAPAY OLARAK KARIŞIMININ SAYISAL MODELLENMESİ

Rezervuarlar, geniş kullanım alanı nedeniyle su yönetiminde önemli role sahiptir. Bir rezervuarda, dikey su sütunundaki sıcaklık profilinin yapısı esas olarak sıcaklığın, çözünmüş maddelerin ve besinlerin dikey dağılımını kontrol eder. Su kolonundaki termal tabakalaşma, oksijensiz ve düşük kaliteli su kaynağına yol açabilir. Yapay katman giderme çalışmaları, ısıl tabakalı su kaynaklarında su kalitesini iyileştirmek için yaygın olarak kullanılmaktadır.

Bu çalışma, rezervuarların su kalitesini iyileştirmek için sıcaklık tabakalı su kolonlarının hava difüzörü ile yapay olarak karışımının sayısal modellemesine odaklanmaktadır.

İlk olarak, sayısal modelleri doğrulamak için destratifikasyon deneyleri yapılmıştır. Deneylerde, hava difüzörü delik çapı, hava debisi ve difüzör delik sayısının destratifikasyon süresi ve verimliliği üzerindeki etkileri gözlemlenmiştir.

Çalışmanın ikinci kısmı, ısıl tabakalı su kolonunun hava difüzörleri tarafından karıştırılması sırasındaki hidrodinamiklerin sayısal modellemesini içermektedir. Hidrodinamiklerin simülasyonu için ANSYS Fluent yazılımı kullanılmıştır. Çok fazlı akışlar, sınır koşulları ve türbülans için model seçenekleri; ve deneysel çalışmalarla karşılaştırılması tartışılmıştır. Eulerian çok fazlı modeli ve k-ω türbülans modeli bu çalışma için uygun bulunmuştur.

Son bölümde ise sayısal model deneylerle doğrulanmıştır. Model karşılaştırmalarının ve gözlemlerin hata analizine dayanarak, en iyi hava difüzörü konfigürasyonu önerilmiş ve sayısal modelin ısıl tabakalı su kolonlarının hava difüzörü ile karıştırılnasını simüle etmede başarılı olduğu kararlaştırılmıştır.

TABLE OF CONTENTS

LIST OF FIGURES

Figure **Page**

Figure **Page**

LIST OF TABLES

Tables **Page**

CHAPTER 1

INTRODUCTION

Water supplies are under growing stress worldwide as a result of climate change, population growth, human health needs, and increased awareness of the environmental consequences of water use and transfer. Reservoirs are critical components of water management in many countries, serving a variety of uses, including irrigation and municipal water supply, hydropower generation, flood control, and recreation. Apart from these many functions, ecological and legal considerations must be made, as both are highly dependent on water quality features. Reservoirs are subjected to complex time-dependent stress and exhibit nonlinear behavior. As a result, numerical models play a critical role in reservoir operation optimization. However, some reservoirs are maintained following methods that prioritize water quantity over water quality. Given the essential nature of water quality, new reservoir operation and management methods are required that incorporate water quality – including water temperature – considerations. This project seeks to close this gap by developing novel reservoir modeling techniques to enable integrated water quantity and quality management.

Wind-induced currents and the vertical water column temperature profile distribution primarily govern the vertical heating, dissolved chemicals, and nutrients in a lake/reservoir. Thermal stratification of the water column: warm and cold water separates into strata, resulting in insufficient mixing throughout the summer. The heated water of epilimnion cannot push through the cold water in the layer of hypolimnion that is dense water since the thermocline between these layers acts as a barrier. The water column can become anoxic due to insufficient mixing and a lack of light for photosynthesis in the hypolimnion. The temperature and dissolved oxygen profiles in Figure 1.1 were obtained during monthly field measurements at the buoy positioned in the main pool of the Tahtali Reservoir in Izmir, Turkey, which supplies 40% of its fresh water to the city's drinking water supply (Elçi 2008). As seen in the picture, recorded dissolved oxygen concentrations fell significantly below the standard limit of 5 mg/l in August, even reaching 0 mg/l at the thermocline.

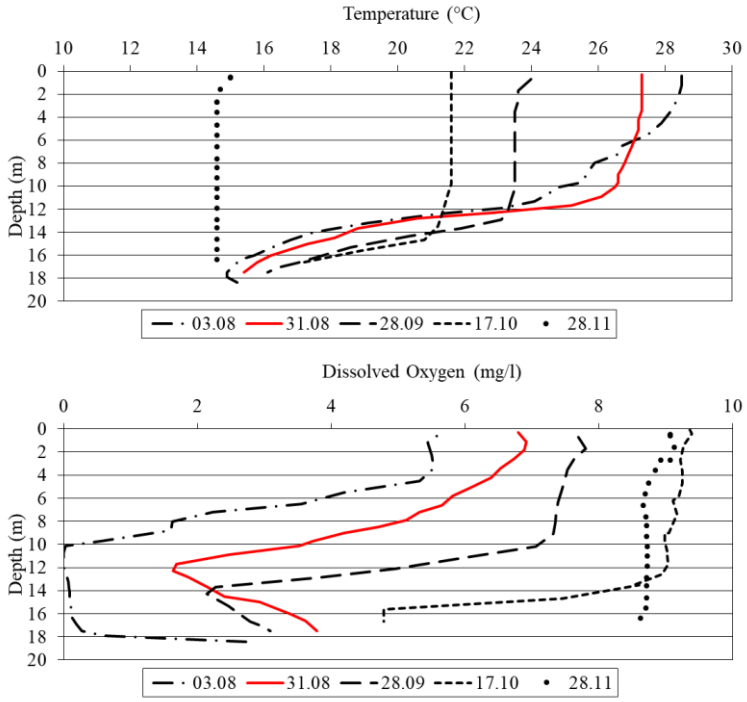

Figure 1.1 The temperature (top), dissolved oxygen (bottom) profiles observed during field measurements conducted once a month at the buoy (Source: Elçi 2008)

As oxygen loss develops to anoxia, bottom sediments release ammonia, sulfides, and oxidized metals such as iron and manganese into the water. Iron and manganese are converted to soluble compounds that are hazardous to aquatic life and a source of contamination for drinking water. In conjunction with iron reduction, phosphorus enrichment results in eutrophication of lakes and hydrogen sulfide production. The reservoir is frequently infected with blue-green algae due to nitrogen influx from the catchments combined with tropical ambient temperatures. Algal blooms degrade water quality by introducing bad smells and tastes, deoxygenating bottom waters, causing toxicity, fish mortality, and altering the food web. Constraints on nutrient input are required to control and manage cyanobacterial and other phytoplankton blooms. The kinds and magnitudes of nutrient input restrictions are determined by hydrologic, climatic, geographic, and geologic variables that interact with anthropogenic and natural nutrient input regimes. In most situations, both nitrogen and phosphorus input reductions are necessary to prevent and manage damaging blooms over the long-term effects. In some instances, nutrient reduction alone may not be adequate, and extra methods such as improved flushing and artificial mixing may be required.

Numerous reservoirs worldwide are affected by cyanobacterial blooms, which have a detrimental effect on the ecology, ultimately leading to the loss of marine biota. Cyanobacteria can be harmful to human health because they have the capacity to create toxins, and various animal and human poisonings have been described as a result of cyanobacterial toxins (Zhang, Deen, and Kuipers 2006; Cox, Banack, and Murch 2003; Griffiths and Saker 2003; Hilborn 2007). Additionally, cyanobacteria may cause other issues in drinking water supply reservoirs. Turkey has recently had difficulties due to an overpopulation of tiny algae termed phytoplankton-Mucilage in the Marmara Sea. This thick, mucus-like slimy coating is formed by a rise in seawater temperature combined with an excess of nutrients caused by pollution. Its production demonstrated the severity of the issue if water resources are subjected to eutrophication. Alternative strategies for cyanobacterial bloom suppression will aid in resolving current and future nutrient load concerns in reservoirs.

The employment of artificial destratification technologies usually addresses these water quality issues, the most popular of which is an air bubbler system. Artificial destratification has been frequently utilized to enhance water quality in thermally stratified lakes and reservoirs associated with eutrophic conditions. Numerous hypolimnetic aeration/oxygenation systems have been implemented in the past with varied degrees of effectiveness (Holland and Tate 1984; Cox, Banack, and Murch 2003). Mixing system by air diffuser, compressed air is pushed to the bottom of the reservoir and released; the resulting buoyant plume transports relatively heavy water upward to be ejected at a height where it is negatively buoyant, resulting in local mixing as the water moves back to the density field. This dismantles the density structure. The efficiency of this approach is contingent upon the bubble plume becoming sufficiently buoyant to allow for significant hypolimnion water movement. Ideally, water from the hypolimnion should pass through into the thermocline before movement; on the other hand, a plume detraining immediately below the thermocline will have little impact. Thus, the effectiveness of a bubbler system is highly dependent on stratification, the position and height of the thermocline, and the flow rate of air. However, the design techniques and strategic control for air diffusers are generally insufficient. While alternative methods of destratification, such as pumped circulation, have certain advantages, the flow mechanics are poorly known, and there is a scarcity of experimental or field data.

This thesis studied the artificial destratification of thermally stratified water column by air diffusers numerically and experimentally. Since the main focus of this study is to develop a numerical model to investigate the parameters affecting destratification by air diffuser system, observations performed in an experimental setup are used for the verification of the numerical model. In the thesis, the first brief information is given about the importance and necessity of artificial destratification in Chapter 1. Corresponding studies in the literature are introduced in Chapter 2. Chapter 3 summarizes the experimental studies performed both for verification of numerical model and for the observation of parameters effective on destratification of the water column by air diffuser system. The theoretical background of simulating the turbulence, multiphase flows, and energy concepts in both Computational Fluid Dynamics and ANSYS Fluent software is presented in Chapter 4. The modeling strategy using the Fluent software is given in detail in Chapter 5. The numerical model verification with the experimental results and the error analysis for the comparison of the model results with the observations are discussed in Chapter 6. Different sub-models in Fluent to simulate multiphase flows and turbulence and their limitations and application areas are further discussed in Chapter 7. Finally, the conclusions derived from the study and the planned future works are summarized in Chapter 8.

CHAPTER 2

LITERATURE REVIEW

The stratification mechanism is controlled by the dynamic relationship between potential and kinetic energy in the water source. Generally, different densities consist of the geophysical fluid, and they are under the effect of gravity causes the arranging in vertical layers. Air diffuser systems are generally addressed to break this vertical layer formation.

Eutrophication, the accumulation of nutrients in a water source, is a commonly reported phenomenon. Eutrophication is a natural growth process that is accelerated by human activity. Increased nutrient levels generated by the entry of industrial sewage and runoff promote the growth of a diverse array of microbes. These, in turn, can result in a variety of unfavorable situations, from "pea soup" water to blue-green algae coating the bottom of a lake to the existence of an undesirable odor and taste in drinking water. Decomposing plants, fish, and some other organic waste sink to the bottom and serve as a nutrition supply for bacteria that use oxygen. As a result, oxygen depletion is probable in a productive lake's or reservoir's bottom water layers. This might have a significant negative impact on lake biota and water quality in general (Torrest and Wen 1976).

In summer, the epilimnion, the upper region, contains warm water generally high in dissolved oxygen (DO) due to gas exchange with the atmosphere and photosynthesis. The lowest region, the hypolimnion, consists of cooler water which, because of low rates of exchange with overlying, aerated water due to thermal stratification, is often deficient in DO. Monomictic lakes that mix just once a year are found in the temperate zone extremes, the tropics, and highly frigid places. In places where winter temperatures fall below 4 ˚C, there might be two mixing episodes per year. Temperate lakes stratify in the winter as the water cools below 4 ˚C and becomes lighter. As a result, this water is prone to anoxia and the associated water quality issues.

Numerous restoration approaches have been developed to address eutrophication-related issues. They may be classified into two types: those that place a premium on

nutrient management for both external and internal, and those that place a premium on direct control or removal of biomass (Benndorf 1988).

Artificial destratification (mixing) aims to reduce algal growth by lowering the internal nutrient loading associated with anaerobic conditions but has no effect on external nutrient loading sources. Artificial circulating has had a mixed record of success. Its usage has a number of negative consequences, including the increase of algae, turbidity, and fish fatalities (Pastorok, Lorenzen, and Ginn 1962). While some unfavorable consequences can be attributed to the secondary impacts of technique, others are probably definitely the result of the insufficient evaluation of the biosphere and its incident management prior to the design of aeration systems or their incorrect use (Pastorok, Lorenzen, and Ginn 1962).

Plumes created by the expulsion of air bubbles can be used in a wide range of ways. They can be used to enhance convective heat and mass transfer in mixing technology (Kipke 1983); as pressurized barriers against density currents (Larsen 1962); in pressurized breakwater implementations; in shoaling control in estuaries and harbors (Bruun 1975); and in icing prevention(Ashton 1974).

There has been much research on bubble plumes in unstratified mediums (Kobus and Engineer 1968) and (Wilkinson 1979a). This has essentially led to the conclusion that a bubble plume may be regarded as a primary buoyant plume, with the bubbles supplying the buoyancy (Wilkinson 1979b). Although bubble plumes are often used in stratified water columns, there seems to have been a relatively limited theoretical or experimental investigation. Mcdougall (1978) and Hussain and Narang (1984) have conducted the only comprehensive studies. McDougall's work examines a highly stratified environment and demonstrates that the bubble behavior is somewhat more complicated in this situation than in an unstratified one. In brief, the bubbles contribute buoyancy to the water formed by the air plumes; consequently, comparatively heavy water is elevated by the plume until the extra buoyancy provided by the bubbles becomes insufficient. At this height, which corresponds to the water-bubble mixture's neutral buoyancy level, the heavy water is drained into the stratified environmental fluid, where it becomes locally dense. The detrained fluid descends, causing mixing to occur. The bubble plume proceeds to ascend, triggering the formation of a new buoyancy plume. This process may repeat numerous times in a substantially stratified water column, resulting in multiple incursions with a

spacing specified by the layering and the buoyancy flux supplied by the bubbles, i.e., the airflow rate. The Hussian and Narang (1983) article is geared at contexts with modest stratification, but achieves roughly the same findings.

A bubble plume can be two-dimensional (bubbles are released from a single diffuser) or axisymmetric (bubbles are released from a single diffuser). Both types of devices, "curtain" and "column" (Goossens 1979), have been demonstrated to be capable of destratification reservoirs.

Also, in literature, it was found that the bubble plume behavior can be affected by the strength (layer thickness and temperate differences) of the stratification. Mcdougall (1978) and Asaeda and Imberger (1993) discussed the many flow field configurations that might exist based on the relative intensity of the bubble plume compared to the ambient stratification.

Zic and Stefan (2009) demonstrated that practical uses of air bubble systems as destratification devices fall into the category defined by Asaeda and Imberger (1993) as having a robust air bubble plume and a relatively moderate stratification.

Recently, the number of studies incorporating numerical models to predict two-phase systems has increased. Gas-liquid systems constitute a more complicated physical system, and advances in computer technology enabled hydrodynamics, mass transport, and chemical reactions by implementing the numerical models. Computational fluid dynamics (CFD) has evolved over the past three decades as a numerical solution tool for the scale-up and design of multiphase systems (Elger, Crowe, and Roberson 1996; Zhang, Deen, and Kuipers 2006). However, because of the intrinsic complexity of multiphase systems, relevant generalized CFD programs are not accessible.

There are primarily three CFD methodologies for modeling multiphase flows: front tracking models (also known as interface tracking models) (Hirt and Nichols 1981), the Euler-Lagrange models (discrete bubble models), and Euler-Euler models (Sokolichin and Eigenberger 1994). The interface-tracking model approximates the development of interfaces between phases well but can only handle a small number of bubbles concurrently owing to its high computing cost. Individual bubbles are represented using the Euler-Lagrangian technique by recording their continuous phase movements. When

the volume percentage of the dispersed phase is more than (>10%), the cost of modeling might be substantial when employing the Euler-Lagrangian technique. The Euler- Euler technique is well suited for large scattered phase fraction systems or industrial-sized systems. Both gas and liquid phases are represented using the premise of interpenetrating continuous fluids in this technique. The disadvantage of the Euler- Euler models is that they require sophisticated interfacial closure connections to alter the phase interaction. For gas-liquid systems, the interfacial momentum transfer is constituted of many forces: drag, additional mass or virtual force, turbulent fluctuation effect, and lift forces. Numerous studies have been conducted to estimate the interfacial exchange terms in gas-liquid systems (Biesheuvel and Spoelstra 1989). Turbulence modeling is critical for multiphase flow simulation: while Large Eddy Simulation (LES) and Direct Numerical Simulation (DNS) have been successfully used to bubble fluids (Derksen and Van Den Akker 1999), their processing cost is too high. As a result, the well-known Reynolds-Averaged Navier-Stokes equation (RANS) technique has been applied for gas-liquid dynamics (Lopez De Bertodano 1998), and it is for industrial scale reactor simulations (Zhang, Deen, and Kuipers 2006).

The dispersed phase of the system undergoes changes owing to coalescence and breaking, which have a significant effect on the interfacial area and mass transfer and response rates. The bubble size distribution and population may be made using Ramkrishna's generalized population balance equations (2000). The population balance equations allow for the formulation of changes in the dispersal phase in the physical environment as well as in the space generated by the population's attributes, referred to as internal coordinates. If the population of bubbles is characterized by a single internal property/coordinate, such as the particle's length, the PBE is said to be monovarietal; if it contains two internal dimensions, it is said to be bivariate; and if it contains more than two, it is said to be multivariate. However, since the population balance equations model is a kind of partial integral-differential equation, it is difficult to solve when many bubble attributes are investigated or geographical inhomogeneities are given.

CHAPTER 3

EXPERIMENTAL STUDY

A series of experiments were carried out at the hydraulics laboratory of Izmir Institute of Technology to investigate the parameters affecting the hydrodynamics of the destratification in the water column by air diffusers

A water tank with the dimensions of 1m*1m*1m (L*W*H) was used for this purpose. The tank was made of steel panels on the sides and had a glass window having 10mm thickness in the front location for observation and measurements during the experiments. Since controlling the temperature and heat flux is important for the purposes of the study, the tank was covered with isolating materials to prevent heat transfer in and out.

Thermal stratification in the water tank was maintained with a cooling system and strip heater. A cooling system is built into the tank's bottom part. The cooling system comprises the compressor, condenser, filter, capillary tube, copper pipes as evaporator, thermostat, and monitor. The copper pipe, which measures around 20 meters in length, is spiraled into the bottom of the water tank, allowing cooling gas to pass through during operation, which is controlled by a thermostat attached to the system. The strip heater used for the heating process is designed to move to the upper surface of the tank so that the operation can be completed as desired. The aim was to maintain thermal stratification with changing temperatures of 10˚C from the bottom and 30˚C to the top to reflect typical natural phenomena, as shown in Figure 3.1.

For artificial destratification, some combination of hole diameter and number of holes of air diffusers was produced. The air diffuser system was designed as replaceable by different plates to practice the combinations of different diffuser diameters, hole numbers, and air flow rates. The plates were produced as the combinations of diffuser holes diameters of 1,2,3,4,5 mm with the 1,2,5,12 number of holes, providing 20 varieties in total. The plane views of plates and view of air diffuser in operation can be seen in Figure 3.2

.

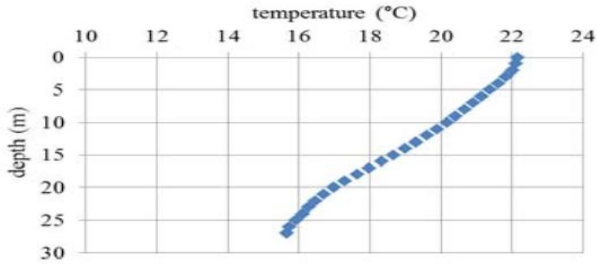

Figure 3.1. Temperature measurements of Tahtali reservoir in summer,2013 (Source: Elçi and Ekmekçi 2016)

Also, an air pump (Tetra-Tec Aps 400) was used, providing 100/h,200l/h, and 400l/h flow rates. The general view of the experimental setup is given in Figure 3.3.

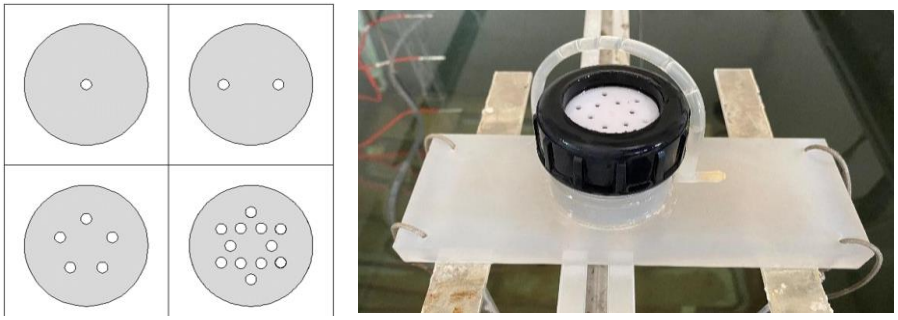

Figure 3.2 Plan views of air diffusers and view of air diffuser in operation

For each experiment, the same thermal stratification pattern was constructed using the cooling-heating system for observation of the effects of different parameters on the thermal profile of the water column. The experiments were recorded on the camera, and the data were taken for each second in 20 minutes, independent of the destratification time.

Temperature measurements were made with thermometers at the height of 5 cm, 15 cm, 30 cm, 50 cm, 70 cm, and 85 cm measured from the bottom of the tank and 30 cm distance away from the rear left corner shown in Figure 3.3 (e). And the temperature values were read from the digital panel in Figure 3.3 (b). Other measurements for the bubbles as slip velocity and bubble diameter were made from the observation window and by a ruler.

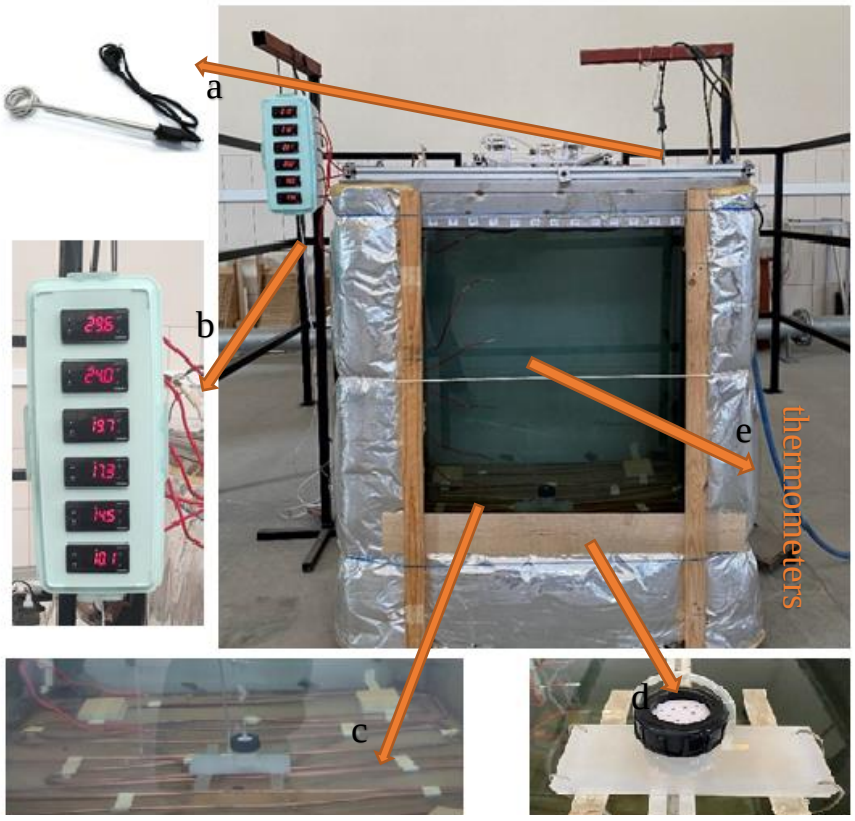

Figure 3.3 The general view of the experimental setup

Several experiments were carried out and will be discussed in this section (Table 3.1). They were selected to observe the effects of air diffuser hole diameter, air flow rate, and the number of holes on destratification efficiency.

Table 3.1 Values of the different parameters selected for the experiments

	Diameter of Air Diffuser (mm)	Number of Holes	Air Flow Rate (l/h)
2D200F	2	1	200
2D400F	2	1	400
3D400F	3	1	400
4D400F	4	1	400
2D400F5	2	5	400
2D400F12	2	12	400

3.1. Experimental Results

3.1.1. Observation of the Effects of Air Flow Rates, Diameter of Air Diffuser, and Number of Holes in the Diffuser

Results of the experiments were evaluated considering three parameters: air flow rate, the diameter of the air diffuser, and the number of holes in the diffuser. To observe the effects of these parameters, comparisons were made with different settings, which will be referred to as 2D200F and 2D400F for different flow rates (200 and 400 l/h respectively); as 2D400F,3D400F, and 4D400F for different diameters (2, 3 and 4 mm respectively); and as 2D400F,2D400F5, and 2D400F12 for the different number of holes (1,5 and 12 holes respectively) from here on.

The effect of air flow rate on destratification time and efficiency was observed. The experiments were carried out with the air diffuser diameter with a single hole and 2 mm diameter, with the air flow rates off 200l/h and 400l/h. In Table 3.2, the initial and final temperature values for each measuring point are listed. Since the most significant variation was observed at the heights of 5cm,15cm, and 85cm due to the thermal stratification pattern, comments were made on these measuring points. The charts of temperature changes as time series were given in Figure 3.4 for these measuring points only to prevent the charts excess.

The effect of air diffuser diameter was observed in this section. The experiments of 2mm,3mm, and 4mm air diffusers were performed under the same conditions of single hole air diffuser and 400l/h air flow rate. In Table 3.2, the initial and final temperature values for each measuring point are listed. Since the most significant variation was observed at the heights of 5cm,15cm, and 85cm due to the thermal stratification pattern, comments were made on these measuring points. The charts of temperature changes as time series were given in Figure 3.5 for these measuring points only to prevent the charts excess.

Table 3.2. Initial and final temperatures of experiments for air flow rate comparison

Height	Air flow rate	Initial Temperature (˚C) (t=0)	Final Temperature (˚C) (t=20 min)
5cm	200l/h	10.00	20.40
	400l/h	9.90	21.20
15cm	200l/h	18.40	20.70
	400l/h	18.40	20.90
30cm	200l/h	20.10	20.60
	400l/h	18.60	20.50
50cm	200l/h	22.00	21.40
	400l/h	21.50	21.20
70cm	200l/h	21.80	21.10
	400l/h	26.00	20.60
85cm	200l/h	29.50	21.10
	400l/h	30.70	21.10

It can be seen that clearly, the air flow rate has a significant effect on destratification time. At 5cm, the temperature reaches the final value of 20.4˚C from 10˚C in 20 minutes for the air flow rate of 200l/h, whereas the duration is around 10 minutes from 9.9 ˚C to 21.2 ˚C for the air flow rate of 400l/h. This result shows that there is a half-time difference between the two air flow rates. This difference is not as sharp for other measuring points but still noticeable.

According to Figure 3.5, it can be said that the destratification process had affected by the diameter of the air diffuser. At 5cm, the rise of temperature is quicker for 4mm diameter than the other, and it can be also said for the height of 85 cm in terms of decreasing rate. For the diameter of 2mm, the time for reaching the final temperature is slower than the others.

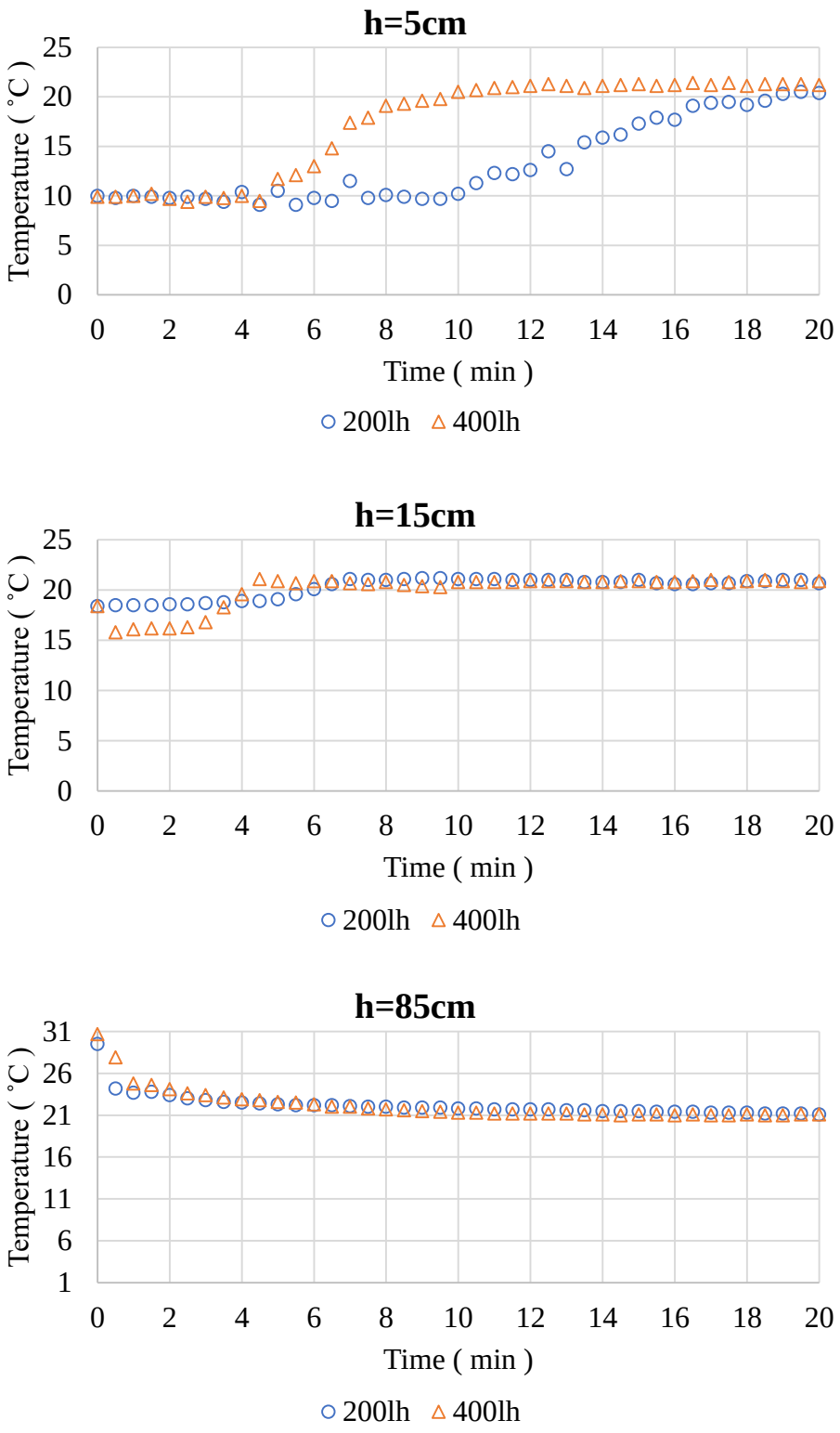

Figure 3.4. Comparison of air flow rates of 2mm air diffuser diameter at h=5,15,85 cm

Table 3.3 Initial and final temperatures for air diffuser diameter comparison

Height	Air Diffuser Diameter (mm)	Initial Temperature (˚C) (t=0)	Final Temperature (˚C) (t=20 min)
5cm	2	9.90	21.20
	3	10.00	21.00
	4	10.50	20.20
15cm	2	15.60	20.90
	3	16.10	20.50
	4	16.10	19.70
30cm	2	18.60	20.50
	3	19.20	20.20
	4	17.90	19.40
50cm	2	21.50	21.20
	3	21.00	20.90
	4	19.60	20.20
70cm	2	26.00	20.6
	3	21.6	20.3
	4	22.1	19.5
85cm	2	30.70	21.10
	3	32.00	20.80
	4	31.00	20.10

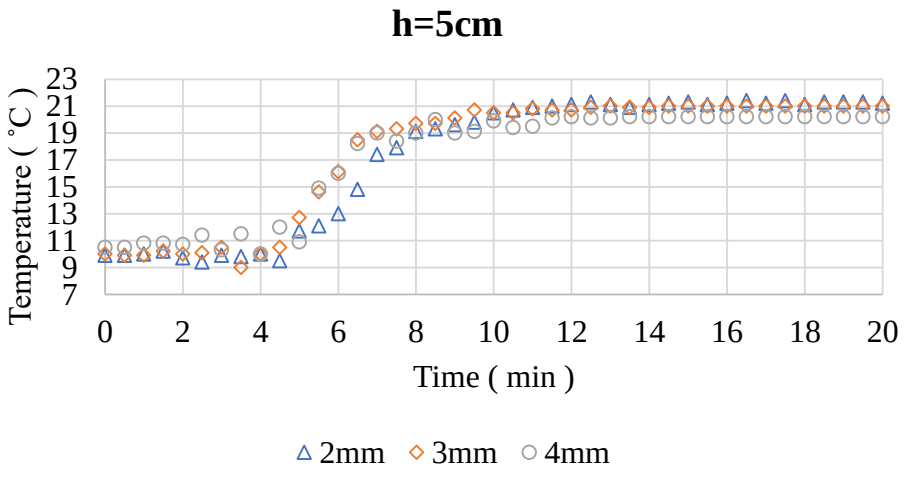

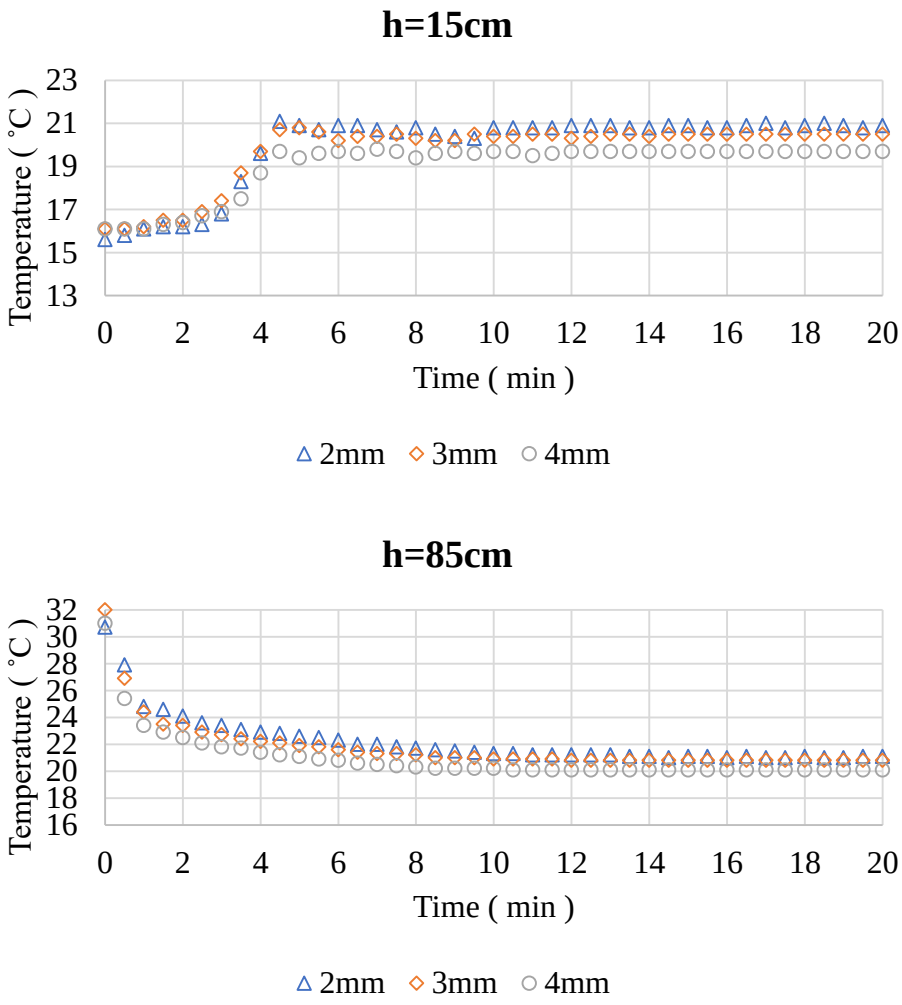

Figure 3.5 Comparison of diffuser diameters of 2mm,3mm, and 4mm at h=5,15,85 cm

The experiments were performed to observe the effect of the number of holes under the conditions of the same air diffuser diameter of 2mm and air flow rate of 400l/h. The graphs in Figure 3.6 show no considerable effect of the number of holes.

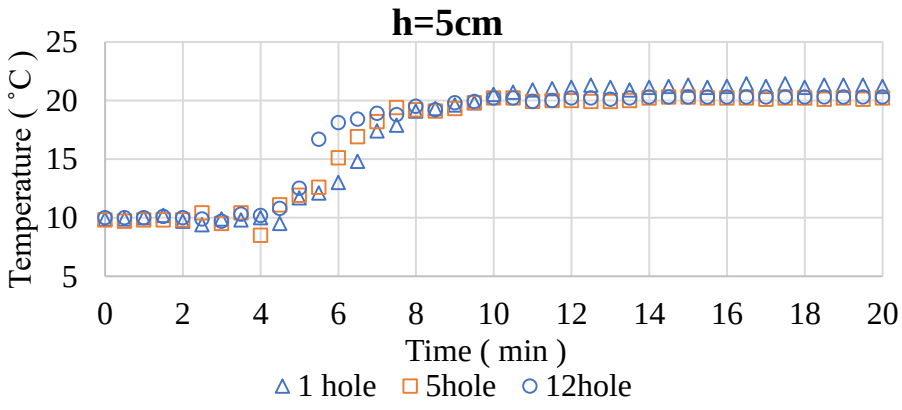

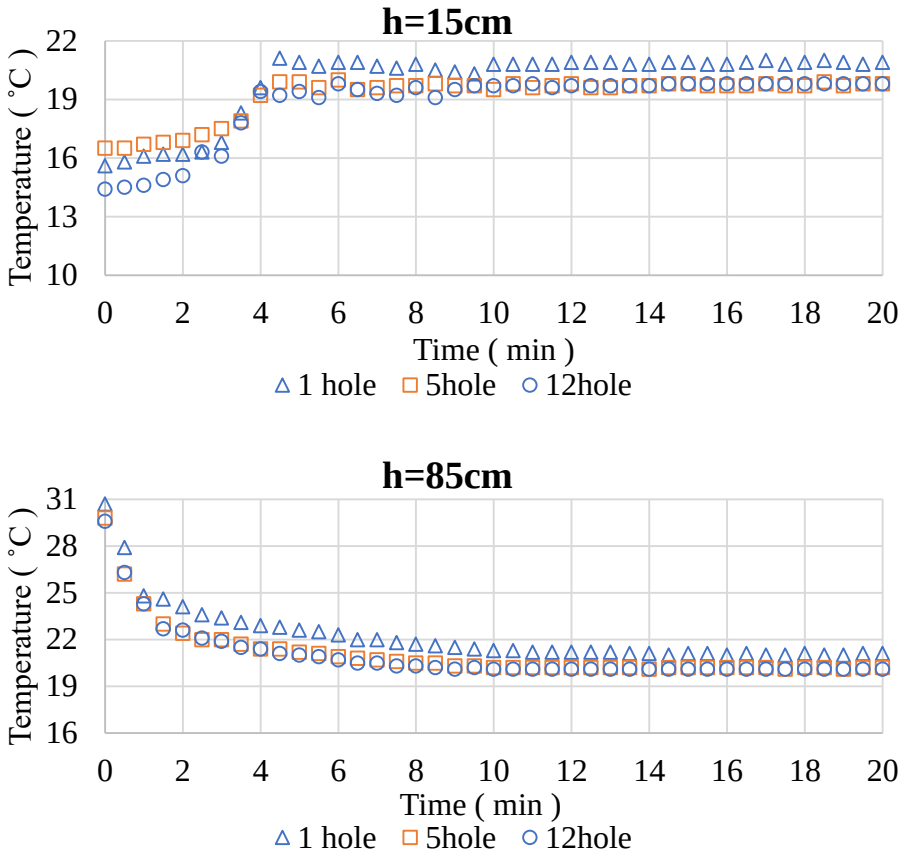

Figure 3.6 Comparison of number of holes of single,5,12 at h=5,15,85 cm

3.2. Destratification Efficiency

The artificial destratification process is a complex phenomenon since it involves the phase interaction between water and air and changing terms depending on the temperature. Some nondimensional parameters were presented in the literature to examine the artificial destratification process and efficiency.

Following the literature, the mixing rate will be characterized by Richardson number and buoyancy fluxes (Elçi and Ekmekçi 2016). Since these formulations involve the fluctuations of the vertical (w') and horizontal velocities (u') and the fluctuations of the density (ρ') by definition, these quantities will be calculated by subtracting 1 minute averaged values from the instantaneous 3D velocity measurements.

The Richardson number assesses the relative strengths of stratification and shear, *Ri*, which measures the interaction of Reynolds stresses with the shear and the stratification, and its formulation is given below.

$$Ri = -\frac{g}{\rho}\frac{\partial \rho}{\partial z}\frac{1}{\left(\frac{\partial w}{\partial z}\right)^2} \tag{3.1}$$

where (g) is the gravity, (ρ) is the density, (z) is the depth, and (w) is the vertical velocity.

Two-phase flow involves the modeling of air bubbles in the water. The rising of the air bubbles is driven by surface tension, buoyancy, viscous and inertial forces. An air bubble adopts a shape where surface tension, hydrostatic and hydrodynamic forces are at balance at the bubble surface. The essential nondimensional number controlling the movement of the air bubbles is the Weber number. It is a measure of the relative importance of the dynamic pressure force compared to the surface tension force and given as:

$$We = \frac{\rho u_b d_b}{\sigma} \tag{3.2}$$

where ρ is the fluid density, d_b is the bubble diameter, u_b is the velocity of the bubble, and σ is the surface tension.

Another parameter that is commonly used to characterize the physical properties of air bubbly flow is Morton numbers and given as:

$$Mo = \frac{We^3}{Fr^2\,\mathrm{Re}^4} = \frac{g\mu^4(\rho-\rho_a)}{\rho^2\sigma^3} = \frac{\left(viscous\ \ force\right)^4\left(buoyancy\ \ force\right)}{\left(inertia\ \ force\right)^3\left(surface\ tension\ \ force\right)^2} \tag{3.3}$$

where ρ is the fluid density, ρ_a is the air density, μ is the fluid viscosity, and σ is the surface tension.

One of the pioneering works on plume behavior was presented by Mcdougall (1978). Two nondimensional variables were presented as:

$$M = \frac{Q_0 p_a}{4\pi\alpha^2 \rho_r H_T u_s^3} \tag{3.4}$$

$$C = \frac{N^2 H_T^2}{u_s^2 M^{2/3}} \tag{3.5}$$

where Q_0=flow gas rate at the free surface; p_a=pressure at the surface; ρ_r=reference liquid density; H_T = total pressure head at the diffuser position; u_S=bubble slip velocity; α=entrainment coefficient; and N=buoyancy frequency given by the following equation.

$$N = \sqrt{(-g/\rho)(d\rho(z)/dz)} \tag{3.6}$$

Asaeda and Imberger (1993) introduced similar variables, called plume number, P_N, and M_H, which are given as follows:

$$P_N = \frac{N^3 H^4}{Q_B g} \tag{3.7}$$

$$M_H = \frac{Q_B g}{4\pi\alpha^2 H u_s^3} \tag{3.8}$$

Socolofsky and Adams (2005) introduced another nondimensional variable, U_N, and demonstrated how to use this variable as a single parameter in predicting the behavior of stratified multiphase plumes at a laboratory level.

$$U_N = \frac{u_s}{(Q_B g N)^{1/4}} \tag{3.9}$$

The destratification number (D_N) is also utilized in the literature and is given as (Kim 2010):

$$D_N = \frac{N^6 H^7}{4\pi\alpha^2 Q_0 g u_s^3} \tag{3.10}$$

where N is the buoyancy, H is the depth in the tank, α is the entrainment coefficient and function of air flow rate, Q_0 is the air flow rate, and u_s is the slip velocity of the bubbles.

In another study, the destratification efficiency is introduced in terms of various nondimensional numbers and is given as (Yum, Sung, and Park 2008):

$$\eta\ (\%) = 4.794 \left(\frac{N h_u D^2}{Q_0}\right)^{0.403} \left(\frac{Q_0}{u_s d_b^2}\right)^{0.148} \left(\frac{Q_0^4}{g^2 A_T^5}\right)^{0.025} \left(\frac{D_l^2}{A_T}\right)^{0.059} \tag{3.11}$$

where A_T is the tank area, Q_0 is the airflow rate, N is the buoyancy frequency, D is the bubble diffusing diameter, u_s is the bubble slip velocity, D_l is the horizontal length scale, η is the destratification efficiency.

The calculations given in Table 3.4 for the performed experiments in section 3.1.1 were created with the help of these dimensionless parameters and the destratification efficiency formula presented in the literature. All calculations in this table were based on the experiments performed in this study, including the density of water measurements, and generated a density formulation depending on temperature, which was explained in section 5.4.3

After these calculations, comparisons of changing parameters can be made based on the destratification efficiency for precise results.

The destratification efficiency values,η, presented in the table above were calculated for the whole mixing process of the experiments. When the data on destratification efficiency was analyzed in a broader context, it becomes clear that the number of holes does not significantly impact the mixing process since the destratification efficiency values are %9.66,9.44% and %9.69 for a single hole, 5 and 12 holes orderly.

The most effective mixing process was observed as %14.78 at the experiment with the air diffuser with a single hole and 4mm diameter, whereas a single hole with 3mm diameter comes after it with an efficiency ratio of %12.49. As a result, it is straightforward to conclude that as the diffuser diameter increases, the efficiency increases as well and that this effect is more pronounced than the effects of all other parameters.

The destratification efficiency values,η, presented in the table above were calculated for the whole mixing process of the experiments. When the data on destratification efficiency was analyzed in a broader context, it becomes clear that the number of holes does not significantly impact the mixing process since the destratification efficiency values are %9.66,9.44% and %9.69 for a single hole, 5 and 12 holes orderly. The most effective mixing process was observed as %14.78 at the experiment with the air diffuser with a single hole and 4mm diameter, whereas a single hole with 3mm diameter comes after it with an efficiency ratio of %12.49. As a result, it is straightforward to conclude that as the diffuser diameter increases, the efficiency increases as well and that this effect is more pronounced than the effects of all other parameters.

The lab-scale experiments conducted in literature, to measure the effects of bubble size and diffusing area, the destratification efficiency changed in a range of %3.5 and %9 in a smaller water tank and lower flow rates than used in this study. Even the efficiency values were different, the same results were concluded; bubble diameter has linearly related to the mixing efficiency, and air flow rate impact on mixing efficiency is not clear to consider (Kim 2010).

Table 3.4 Overview of parameters in experiments and nondimensional numbers

Case	H	A_T	Q_{air}	n	D	d_b	U_{slip}	u_t	D_a	h_m	T	ρ	N	α	M	C	D_1	U_N	η (%)
2D200F	0.85	1	5.60E-05	1	2	12	0.34	17.68	0.0015	0.3	20.1	1050.9	0.239	0.03	0.11	274.5	1.29	3.18	10.95
										0.1	14.2	1052.0							
2D400F	0.85	1	0.00011	1	2	12	0.372	35.37	0.0015	0.3	18.6	1051.2	0.227	0.03	0.12	186.5	1.5	2.97	9.66
										0.1	12.8	1052.2							
3D400F	0.85	1	0.00011	1	3	15	0.364	15.72	0.0015	0.3	19.2	1051.1	0.236	0.03	0.13	202.4	1.6	2.87	12.49
										0.1	13.5	1052.2							
4D400F	0.85	1	0.00011	1	4	18	0.32	8.84	0.0015	0.3	17.9	1051.3	0.2	0.03	0.19	145.9	2.35	2.63	14.78
										0.1	13.3	1052.2							
2D400F5	0.85	1	0.00011	5	2	12	0.34	35.37	0.0015	0.3	18.2	1051.3	0.191	0.03	0.16	132.9	1.96	2.83	9.44
										0.1	13.2	1052.2							
2D400F12	0.85	1	0.00011	12	2	12	0.34	35.37	0.0015	0.3	17.3	1051.5	0.205	0.03	0.16	151.8	1.96	2.78	9.69
										0.1	12.2	1052.317							

3.3. Summary of Experimental Studies

This chapter examined experimentally the artificial destratification process of the thermally stratified water column through different combinations of air diffusers. Several experiments were performed in the Hydraulic Laboratory at Izmir Institute of Technology. Air diffusers with different configurations of diameters, holes, and air flow rates were used in the experiments to investigate the effects of these parameters on the destratification process of the water column in the experimental setup.

To investigate the effects of air flow rate, experiments were conducted using a single hole air diffuser with a diameter of 2 mm, and two different air flow rates of 200l/h and 400l/h were given to the system. Based on the charts in Figure 3.4 and destratification efficiency, η, in Table 3.4, there was no significant change in the destratification efficiency. Still, the mixing was reached much faster with the higher air flow rate, especially at the hypolimnion.

The positive effect of the increasing diameter of the air diffuser on mixing efficiency was the most significant observation based on the performed experiments of a single hole air diffuser with the diameters of 2mm,3mm, and 4mm under the same air flow rate of 400l/h. When the destratification efficiency was around %10 for 2mm diameter, it reached around %15 for the diameter of 4mm, which means that the mixing process would be more effective with the ratio of %50 for the diameters of 2 and 4mm. However, it was clear that the diameter of the air diffuser had no impact on the destratification time, which can be understood in Figure 3.5.

In order to examine the effect of the number of holes of the air diffuser on the mixing process, experiments were conducted with the hole numbers of a single hole,5 holes, and 12 holes under the same conditions of air flow rate of 400l/h and 2 mm air diffuser hole diameter. According to charts in Figure 3.6 and destratification efficiency, η, in Table 3.4, there was no noticeable effect on destratification time and efficiency, except that the five-hole one makes little positive difference.

Although this chapter includes the experimental studies, the primary purpose of this thesis is to generate a numerical model which is applicable for the artificial

destratification of thermally stratified water column by air diffuser. So, these experimental results were obtained for the numerical model verification, which was presented in Chapter 6.

CHAPTER 4

NUMERICAL THEORY

4.1. CFD Modeling in General

This chapter will discuss the input required to solve CFD issues, including CAD geometry, computational mesh, material parameters, and boundary conditions. The complexity and accuracy of CFD simulations for a variety of applications are briefly explored, including laminar and turbulent flows, single-phase and multiphase flows.

Simulating simple, single-phase laminar flow is extremely precise, and simulations of the majority of single-phase turbulent flows are dependable. However, many engineering systems are quite complex, and models of multiphase systems and systems with extremely quick responses are still imprecise. Traditional models based on well-proven design equations that have been validated over many years are more accurate than the finest CFD simulations for these systems. However, design equations are only accessible for current equipment and a restricted range of process circumstances, and CFD simulations may be extremely valuable even when exact predictions are not feasible, for example, by calibrating the model to get an experimentally confirmed solution. Parameter studies may do using this simulation by making tiny adjustments to the parameters, for example, to determine the effect of changes in temperature, flow, or viscosity.

One advantage of employing CFD is that comprehensive local information about the simulated system may be obtained. It is feasible to mimic not just conversion but also local temperature, particle entrainment, back mixing, and bubble formation in a fluidized bed. This precise information will aid in developing a qualitative picture of the process, and a parameter analysis will disclose further details such as bottlenecks and equipment operational limitations. Without the necessary expertise, CFD simulation may be a highly unpredictable instrument. Commercial CFD applications have a large number of default

parameters and nearly always produce results from simulations; nevertheless, to acquire trustworthy results, the model must be chosen logically.

4.1.1. Flow Definition

It is advantageous to distinguish between the qualities of fluids and flows. The intrinsic characteristics of fluids, such as viscosity, density, surface tension, diffusivity, and heat conduction, may be expressed as functions of temperature, pressure, and composition. Pressure, turbulence, and turbulent viscosity are all flow-dependent properties.

In CFD modeling, the concept of flow has separated the sub-categories as laminar/turbulent, steady/transient, and single-phase/multiphase.

4.1.1.1. Laminar Flow

The Navier–Stokes equations explain the momentum transmission of a flow dominated by viscous forces in laminar flow. CFD can provide extremely accurate flow models for single-phase systems when the flow is always laminar.

It is difficult to correctly replicate the transitions between laminar and turbulent flow, both from turbulent to laminar and from laminar to turbulent. The flow can vary between laminar and turbulent in this area, and turbulent slugs regularly emerge in laminar flow much below the essential Reynolds number for turbulent flow transition.

Additionally, heat transport simulations are frequently rather precise, and accurate temperature predictions are easily achieved. Mass transport is also fairly simple in the gas phase. However, because liquids have diffusivities approximately four orders of magnitude less than gases at ambient pressure, realistic mass-transport calculations in laminar liquids are problematic.

4.1.1.2. Turbulent Flow

Although the Navier–Stokes equations describe turbulent flows, they are seldom solved for practical engineering applications, even with supercomputers, due to the flow's characteristics. Solving the Navier–Stokes equations requires an extremely precise time

and space resolution, which is currently not attainable. The direct solution of the Navier–Stokes equations (DNS) for simple models, on the other side, is extremely useful to better understand turbulence and generate better models.

A more cost-efficient approach is to resolve just large-scale turbulence, filtering out fine-scale turbulence and modeling these tiny scales as flow-dependent effective viscosity. This technique, known as large-eddy simulation (LES), is gaining popularity because it enables the simulation of basic engineering processes on a fast computer. However, the simulations are quite time-intensive on a computer, and several weeks are sometimes required to produce acceptable statistical averages for even fairly simple flows.

It is impossible to resolve the turbulence fluctuations in increasingly complicated flows. Reynolds-averaged Navier–Stokes (RANS) techniques are used in the majority of engineering simulations. Although these models use time-averaged turbulent fluctuations, they may be used to approximate respectable velocity averages. However, critical features of the flow remain uncertain. Everything that occurs on a scale finer than the grid size is unresolved, for example, the decomposition and coalescence of bubbles and drops in multiphase flow. To incorporate these occurrences, additional models must also be introduced to the RANS models.

4.1.1.3. Single-Phase Flow

Quite accurate solutions can be obtained in single-phase laminar flow when in turbulent flows; it can be satisfactory for more cases.

4.1.1.4. Multiphase Flow

Gas-liquid, gas-solid, liquid-liquid, liquid-solid, or gas-liquid-solid systems are all examples of multiphase flow. It is possible to produce satisfactory simulation results for a multiphase system containing very small particles, bubbles, or droplets that closely follow the continuous phase. Systems wherein the dispersed phase has a significant influence on the continuous phase are harder to model effectively, and for multiphase systems with a high dispersed phase load, only basic models are available. Currently, the quality of simulations is limited not by computer speed or memory but by a dearth of

excellent multiphase flow models. However, multiphase flows are critical in engineering because they are involved in a large number of common processes.

4.1.2. CFD Model Process

For simulation of any model in CFD programs, the steps in Figure 4.1 are followed.

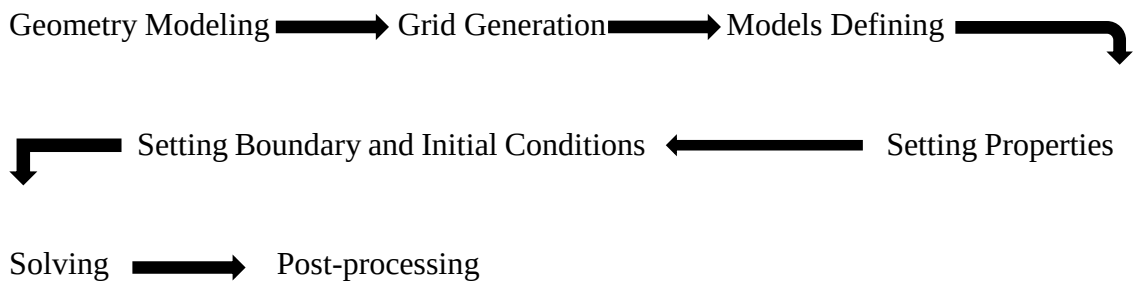

Figure 4.1. Steps in the CFD process

4.1.2.1. Mesh (Grid Generation)

The momentum transfer equations are nonlinear, which means that the computational volume must be correctly discretized in order to achieve an accurate numerical solution. Meshing the computational domain accurately is just as critical as establishing the physical models. Due to the fact that an ill-conditioned mesh might produce extremely erroneous results, the mesh's quality, including its aspect ratio and skewness, must be checked before the simulations. Most CFD applications also include adaption, which permits local grid modification when necessary after obtaining a preliminary result.

4.1.2.2. Defining Model

The Navier–Stokes equation calculations were performed easily for single-phase laminar flow, but as for turbulent and multiphase flows, the user must adopt the most appropriate model. There are a few widely recognized models of turbulence and multiphase flow, although hundreds of others are available. Additionally, numerous parameters must be adjusted for each model. While the default choices are frequently the best choice, the user may occasionally identify more suitable parameters. Additionally, with the majority of commercial CFD applications, you may construct your customized

model as a user-defined subroutine/function (UDS/UDF). The CFD software does not determine all properties, and several semi-empirical models must also be specified. Empirical models for drag and Sherwood and Nusselt numbers as a function of the localized particle Reynolds number or turbulence intensity characterize the momentum, heat, and mass transfer between the dispersed and continuous phases in multiphase flow.

4.1.2.3. Setting Properties

Properties of fluids like viscosity, density, pressure dependency are defined before the solution is started. Some of them are available in the CFD software, and also they can be introduced to the model, not as a constant but as writing UDS/UDF or an equation with different coefficients like done in this study.

4.1.2.4. Boundary Conditions

Boundary conditions have an important role in obtaining accurate results in CFD modeling. All inlet and outlet of the flow must be defined as close as the real cases. Lots of options are available in CFD programs, and also, again, for the behaviors of boundary conditions, UDF can be written to expand or collapse the properties. Except for the inlet and outlets, conditions for the wall also must be defined. When defining boundary conditions, initial parameters are defined for transient simulations.

4.1.2.5. Solve

Before the solution is started, the final step is the solving properties. Options like segregated or coupled solver, implicit or explicit time-stepping methods must be chosen according to problem cases. Also, acceptable convergence criteria for iterations must be defined properly.

4.1.2.6. Post-processing

Post-process is one of the steps of numerical modeling in which the quality of the solution is measured in the ways of effects of grid size, numerical schemes, chosen boundary conditions on the solution. The final simulation results analysis will then provide local information regarding flow, concentrations, temperatures, and reaction

rates, among other things. Although the findings are not particularly precise for more complicated systems, it can still be seen that how changing parameters affect the final solution, for example, defining a density and viscosity profile as a polynomial changing with temperature for the destratification process of a water column.

4.2. Turbulence in General

Turbulence occurs in the majority of natural and industrial flows. Natural turbulent flows occur in seas, rivers, and the atmosphere, whereas industrial turbulent flows occur in heat exchangers, chemical reactors, and other industrial processes. Most industrial flows are turbulent, as turbulence considerably increases heat and mass transfer rates. Various types of turbulent multiphase flows can be found in the industry. Turbulence is critical in these sorts of flows because it impacts processes such as bubble and drops break-up and coalescence, hence regulating the interfacial area between the phases. Thus, turbulence modeling becomes a critical component of CFD. To evaluate which technique to turbulence modeling is most appropriate for a specific application, limits and variation of turbulence models must understand clearly.

4.2.1. Characteristic Features of Turbulence

The concept of turbulence is described as an irregular state of flow in which multiple parameters exhibit random fluctuation with respect to time and space coordinates, allowing for the identification of statistically distinct average values. (Hinze 1975).

The continuous turbulent regime requires the turbulent energy source; otherwise, turbulent structure damage and evolve the smaller ones than after the flow regime turns the laminar flow. Possible future developments of turbulence can be determined by analysis of turbulent flows. Tennekes and Lumley (1972) did not provide a clear definition of turbulence; rather, they highlighted the most distinctive features of turbulence. These are as follows:

One of these features is irregularity. Turbulent flows are amorphous, unpredictable, and chaotic in nature, exhibiting a broad variety of length, velocity, and

time scales. In turbulent flows, large-scale movements are often referred to as vortices. A turbulent eddy is a turbulent movement that is at least substantially coherent in a particular location. A large turbulent eddies domain may also contain smaller ones. This implies that several sizes coexist and that smaller scales occur inside larger ones. The biggest sizes in turbulent flows are constrained by the flow's geometry, and the smallest scales are constrained by viscosity. The tiniest eddies are often hundreds of times smaller than the largest eddies. Eddies expand, spin, and split into more as they travel. Because turbulent flows are very irregular and span a large variety of length and time scales, a classification algorithm for turbulence modeling is extremely challenging. As a result, statistical models are commonly utilized in engineering simulations.

Probably the most distinguishing feature of turbulence is its diffusive nature. Due to the chaotic movements in the flow, turbulent diffusive transport enables greater mixing rates of species, momentum, and energy than would be possible by molecular diffusion alone. These speeds are often many orders of magnitude greater than the diffusion rate of molecules. Due to the fact that turbulence is a three-dimensional phenomenon, turbulent transport happens in all dimensions.

At high Reynolds numbers, instability occurs. Turbulence occurs as a result of instabilities at high Reynolds numbers. This occurs physically when the timeframe for viscous damping of a motion variation exceeds the timeframe for convective transfer.

The energy dissipated during chaotic kinetic energy dissipation. All turbulent flows exhibit an energy flux from the biggest turbulent sizes to the smallest turbulent scales. Due to viscous strains at the lowest scales, turbulent kinetic energy is wasted as heat. The concept of energy cascade is the flux of energy. The energy cascade hypothesis states that kinetic energy penetrates turbulence at the highest levels when energy is taken from the mean flow. This energy is subsequently transmitted to tiny sizes via inviscid processes. This energy flow occurs because huge eddies are unsustainable and divide up into separate eddies, moving energy to lower scales. These smaller eddies follow a similar process of disintegration and energy transfer to even smaller eddies. On the tiniest scale, we have dissipative eddies, which have their energy wasted into heat due to viscous action caused by molecular viscosity. The illustration of this energy flux can be examined in

Figure 4.2. As a result of the dissipation, turbulence decays swiftly in the absence of external energy.

Turbulence is a continuous phenomenon, so the motion of fluids is described by mass and momentum conservation equations augmented by initial and boundary conditions.

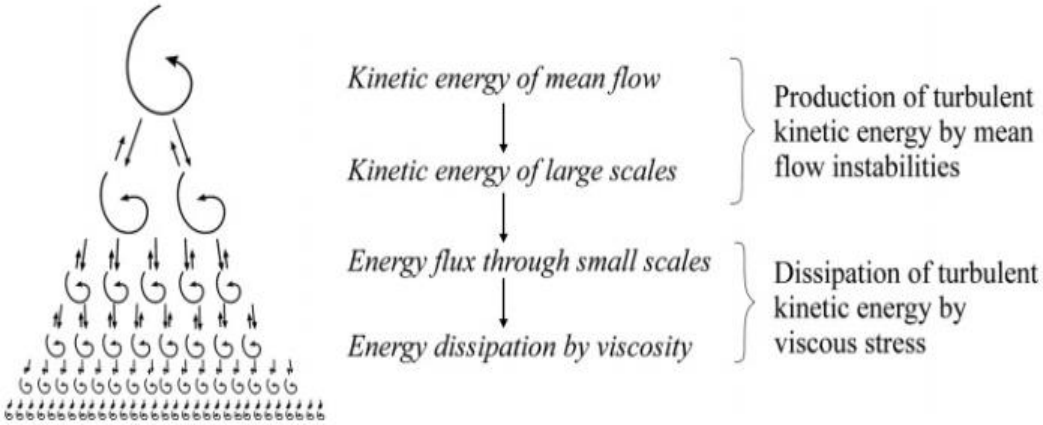

Figure 4.2 Energy flux illustration in turbulent flow

(Source: Anderson 1995)

4.2.2. Reynolds Number

There is a criterion which is a dimensionless number, to determine the regime of flow as laminar, transition, or turbulent. Reynolds (1842-1912) discovered the non-dimensional Reynolds number, which is a ratio of inertial to viscous forces. This invention simplified the comprehension of turbulent flow.

$$RE = \frac{\rho V d}{\mu} = \frac{V d}{\upsilon} = \frac{Q d}{\upsilon A} \tag{4.1}$$

where the density ρ, diameter d, velocity υ, and viscosity μ are the parameters of the Reynolds number, Lower Reynolds numbers indicate laminar flow, whereas higher Reynolds numbers indicate turbulent flow; however, the point at which laminar flow transitions to turbulent flow is dependent on a variety of parameters, such as wall roughness, pressure differential, and others. (Roberson and Crowe 1975).

4.2.3. Turbulence Modeling in CFD

The Navier Stokes equations are the fundamental equations of fluid flow, deriving from momentum balances on a fluid element. The Navier Stokes equations are employed in the numerical simulation of turbulent flow, either directly or indirectly. Turbulent flow is exceedingly complex to solve due to the widely diverse mixing-length scales involved.

The continuity equation is as follows for the case of only conservation of mass and momentum equations are considered for an incompressible Newtonian fluid which has under conditions of constant density,ρ and viscosity,μ and also has a velocity field as $\vec{v} = (u_r, u_\theta, u_z)$ cylindrical coordinates (r, θ, z) (Verrsteg and Malalasekera W. 2007);

$$\frac{1}{r}\frac{\partial}{\partial r}(ru_r) + \frac{1}{r}\frac{\partial}{\partial \theta}(u_\theta) + \frac{\partial}{\partial r}(u_z) = 0 \tag{4.2}$$

When the analytical solution of equation (4.3) is possible for laminar flow, numerical solution for turbulent is difficult. This is owing to the considerably differing mixing-length scales involved, which necessitates a small mesh resolution, rendering very turbulent flow computations computationally infeasible. There are alternative methods which are Reynolds averaging and filtering, to solve Navier Stokes equations so that it is not necessary to direct simulation of small-scale turbulent disturbances.

For an incompressible fluid with constant density and viscosity, the Navier Stokes equations of motion are:

$$\rho\left[\frac{Du_r}{Dt} - \frac{u_\theta^2}{r}\right] = -\frac{\partial p}{\partial_r} + f_r + \mu\left[\nabla^2 u_r - \frac{u_r}{r^2} - \frac{2}{r^2}\frac{\partial u_\theta}{\partial \theta}\right]$$

$$\rho\left[\frac{Du_\theta}{Dt} - \frac{u_r u_\theta}{r}\right] = -\frac{1}{r}\frac{\partial p}{\partial_\theta} + f_\theta + \mu\left[\nabla^2 u_\theta - \frac{u_\theta}{r^2} - \frac{2}{r^2}\frac{\partial u_\theta}{\partial \theta}\right] \tag{4.3}$$

$$\rho\left[\frac{Du_z}{Dt}\right] = -\frac{\partial p}{\partial_z} + f_z + \mu[\nabla^2 u_z]$$

where f is the body force components is cylindrical coordinates, p is the pressure, and operators are as follows:

$$\frac{D}{Dt} = \frac{\partial}{\partial t} + u_r \frac{\partial}{\partial r} + \frac{u_\theta}{r}\frac{\partial}{\partial t} + u_z \frac{\partial}{\partial z}$$

$$\nabla^2 = \frac{\partial^2}{\partial r^2} + \frac{1}{r}\frac{\partial}{\partial r} + \frac{1}{r^2}\frac{\partial^2}{\partial \theta^2} + \frac{\partial^2}{\partial z^2} \quad (4.4)$$

The most common techniques for turbulent in numerical analysis are as follows:

- Direct numerical simulation (DNS);
- Large-eddy simulation (LES);
- Reynolds averaged Navier Stokes (RANS).

Turbulent flows are defined by fluctuating velocity fields that combine and vary with conveyed variables such as momentum, energy, and mass. These oscillations are discovered to be computationally prohibitively costly to replicate, much more so for complicated, high Reynolds flow. As a result, other ways that are computationally efficient are utilized to avoid directly simulating tiny scale turbulent oscillations (Verrsteg and Malalasekera W. 2007; Gatski, Hussaini, and Lumley 1996; Theodore 1971).

4.2.3.1. Direct Numerical Simulation (DNS)

The direct numerical simulation (DNS) technique can seem to be the most apparent and easy method for simulating turbulent flows at first look. There is no need for a turbulence model when using DNS, which solves the unsteady 3D Navier–Stokes equations directly. The equations accurately describe fluid flows in both laminar and turbulent circumstances. The challenge arises when these equations are solved at a high Reynolds number. Recall that turbulent flows with a high Reynolds number exhibit a large range of length and time scales. This implies that the simulations must resolve all of these turbulent scales. The required level of resolution is approximately defined by the Kolmogorov length and time scales. As a result, extremely dense computing grids and extremely small time intervals are required. Add to this the fact that the equations are nonlinear, and it is evident that the computational solution procedures will be challenged, making any simulation extremely time-consuming. Indeed, it will be impossible to use DNS to solve real-world technical issues by developing computer power. Even if these simulations were practicable for actual engineering applications, the volume of data generated would be staggering. At the moment, DNS is mostly used for research purposes

rather than as a design help. DNS has a high computing cost, which grows with the cube of the Reynolds number.

4.2.3.2. Large Eddy Simulation (LES)

Given that the primary difficulty in modeling high-Reynolds-number flows is the existence of extremely short length and time scales, it makes sense to filter the equations, resolving turbulence scales between intermediate and large. By purposely leaving the lowest turbulence scales unresolved, large-eddy simulation (LES) enhances the use of DNS for actual engineering applications. The dynamics of large scales are explicitly simulated in LES because that LES must be three-dimensional and dynamic. The advantages of LES stem from the fact that massive eddies, which are difficult to represent universally due to their anisotropy, are directly modeled. In comparison, tiny eddies are easier to model because they are more isotropic and adapt rapidly to maintain a dynamic equilibrium with the energy transfer rate imposed by big eddies. Subgrid stress models account for the impacts of unresolved scales, which cannot be ignored. This implies that the subgrid models should be globally applicable. This model is well-suited for simulating flows with a high Reynolds number. Despite this, the computational cost of LES is rather expensive in contrast to other turbulence models. The high computational cost is due to the extremely tiny grid, the small-time increments, and the lengthy computing time required to generate trustworthy statistics.

4.2.3.3. Reynolds Averaged Navier Stokes (RANS)

LES is predicted to see a growth in industrial applications in the near future. LES, on the other hand, is now too computationally costly for routine simulations, similar to DNS. Frequently, the industrial and academic worlds want models that are even simpler than LES. This chapter introduces turbulence models, which are commonly utilized in engineering simulations. These models depend on a technique for separating the scales. Recall that the LES technique eliminates short length and temporal scales. Even so, it is necessary to filter out intermediate-to-large turbulence scales in order to produce a set of equations suitable for everyday simulations. As a result, solving these equations remains the sole feasible method for doing typical models of turbulent flows seen in engineering

practice. Reynolds postulated over a century ago that instantaneous variables as velocity and pressure might be divided into a mean and a fluctuating component

$$U_{\mathrm{i}} = \langle U_{\mathrm{i}} \rangle + u_i \tag{4.5}$$

$$P = \langle P \rangle + p \tag{4.6}$$

As a result, this procedure is referred to known as Reynolds decomposition. All of the turbulence models discussed in the subsequent sections of this chapter are mathematically based on the Reynolds-decomposition notion. With Reynolds decomposition, the mean flow velocity and turbulence quantities are used to statistically characterize the flow. The turbulence fluctuations are isolated from the non-turbulence components by time averaging over an acceptable time span. As a result, the set of equations generated using this approach is referred to as the Reynolds averaged Navier–Stokes equations or RANS equations. In many real situations, it is required to model non-steady flows by averaging the instantaneous variables across a time period that is long in comparison to the turbulence timeframes but short in comparison to the mean component timescale. This means that in the RANS equations, the time derivative of the mean flow compensates for fluctuations over timescales higher than those of turbulence.

Recalling the continuity and Navier Stokes equations orderly

$$\frac{\partial U_j}{\partial x_j} = 0 \tag{4.7}$$

$$\frac{\partial U_i}{\partial t} + U_j \frac{\partial U_i}{\partial x_j} = -\frac{1}{\rho}\frac{\partial P}{\partial x_i} + \upsilon \frac{\partial^2 U_i}{\partial x_j \partial x_j} \tag{4.8}$$

Let instantaneous variables in equations of ((4.5)) and ((4.6)) substitute the equations of ((4.7)) and (4.8), the following obtains

$$\frac{\partial(\langle U_i \rangle + u_i)}{\partial x_i} = 0 \tag{4.9}$$

$$\frac{\partial(\langle U_i \rangle + u_i)}{\partial t} + (\langle U_j \rangle + u_j)\frac{\partial(\langle U_i \rangle + u_i)}{\partial x_j} = -\frac{1}{\rho}\frac{\partial(\langle P \rangle + p)}{\partial x_i} + \upsilon \frac{\partial^2(\langle U_i \rangle + u_i)}{\partial x_j \partial x_j} \tag{4.10}$$

After time-averaging is applied for all terms in linear fluctuating variables and not applied in nonlinear terms, then arranging, general RANS equation

$$\frac{\partial\langle U_i\rangle}{\partial t}+\langle U_j\rangle\frac{\partial\langle U_i\rangle}{\partial x_j}=-\frac{1}{\rho}\frac{\partial\langle P\rangle}{\partial x_i}+\upsilon\frac{\partial^2\langle U_i\rangle}{\partial x_j^2}+\frac{\partial\langle u_iu_j\rangle}{\partial x_j} \tag{4.11}$$

Which can also be written as

$$\frac{\partial\langle U_i\rangle}{\partial t}+\langle U_j\rangle\frac{\partial\langle U_i\rangle}{\partial x_j} = -\frac{1}{\rho}\frac{\partial}{\partial x_j}\left\{\langle P\rangle\delta_{ij}+\mu\left(\frac{\langle U_i\rangle}{\partial x_i}+\frac{\langle U_j\rangle}{\partial x_j}\right) - \rho\langle u_iu_{ij}\rangle\right\} \tag{4.12}$$

The term of $\left(-\rho\langle u_iu_{ij}\rangle\right)$ in equation (4.12) is called Reynolds stress term, which means the second-order moment of the velocity components at one point.

4.2.3.4. Overview

For a numerical simulation, scaling size differences between Direct Numerical Simulation and Large Eddies Simulation and Reynolds Averaged Navier Stokes can be shown in Figure 4.3.

Overview of turbulence modeling in numerical simulations and available turbulence models with properties can be examined in Table 4.1.

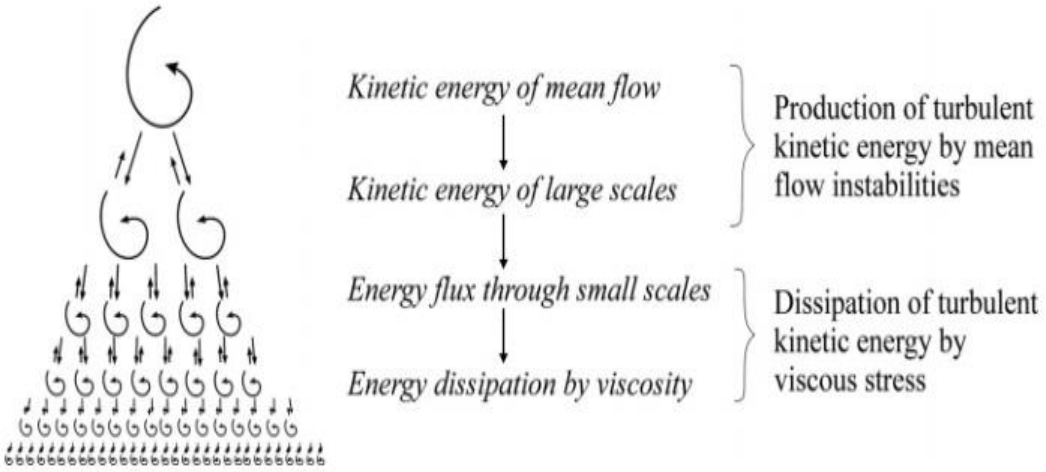

Figure 4.3. Illustration of resolved turbulent scales (Andersson 2011)

4.3. Multiphase Model in General

In CFD, the multiphase concept is as essential as turbulence because flows are mostly multiphase in the areas from nature to industry. Multiphase flow research is a very vast and imprecisely defined field of study. This has resulted in a plethora of basic and applied research fields. It has also resulted in a great deal of confusion. There is no agreement on the mathematical model to be utilized, let alone all the experimental closure models derived from measurable data. Certain sectors allow for reliable ab-initio simulations, while others allow for just parameter analyses based on experimentally validated simulations. Multiphase flow models are often valid at low particle concentration and with particles that closely follow the continuous phase.

Multiphase can be defined as a simulation of the flow combination of two or more phases, which refers to states of matter as solid, gas, or liquid. In other words, it is the flow of the mixture of the states of matters, such as bubble columns, fluidized beds, droplets, burning, melting. Definition of phase is the state of matter in thermodynamics. So additionally to the above multiphase defining, not only two different states of matter but also the modeling of two immiscible liquids is also considered as multiphase flow (Clift, Grace, and Weber 2005).

Table 4.1 Overview of Turbulence Modeling

Direct Numerical simulation		No turbulence model
Large Eddy Simulation		Only subgrid turbulence modeling
RANS-based models (One-point statistical modeling)	**Reynolds Stress Model**	Second-moment closure
	Two Equation Models Realizable k-Ɛ RNG k-Ɛ Standard k-Ɛ Standard k-ω	First-moment closure
	One-equation Models Spalart-Allmaras	
	Zero-equation (Algebraic) Models Prandtl's mixing-length model Uniform Turbulent Viscosity	

A critical distinction between multiphase flow is made according to phase presentation in the flow as separated or dispersed, as shown in Figure 4.4. The phase is often represented by particles or droplets in a dispersed flow, while several separate contacts exist. The phases of a separated flow are primarily isolated, having just a few interfaces.

Typically, dispersed flows are categorized into two categories of flow regimes: dilute and dense. Because the space between particles or droplets is exceptionally significant in the dilute regime, their behavior is dictated by continuous phase (fluid)

forces. Because the distance between particles is smaller in dense phase systems, inter-particle interactions are often rather significant. Dense flows are defined as those having a particle diameter spacing of fewer than ten.

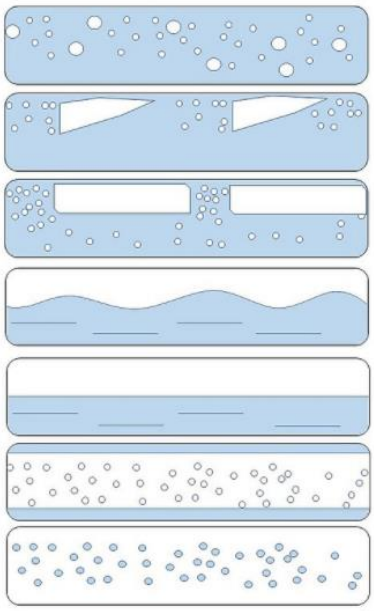

Figure 4.4. Different topologies of horizontal multiphase flow
(Source: https://www.wikiwand.com/en/Multiphase_flow)

Due to the existence of several phases, characterizing and measuring the nature of the flow is far more complex than under single-phase circumstances. It is challenging to calculate velocity owing to insufficient information about the velocities of each phase at a certain point.

There are two basic approaches to simulate multiphase flow. One of them is the Euler-Lagrange method, which solves the Navier-Stokes equations with the fluid phase considered as a continuum. Solving the dispersed phase requires monitoring a large number of dispersion particles, bubbles, or droplets. With the fluid phase, the scattered phase may interchange momentum, mass, and energy. (Crowe 2005).

Another approach is Euler-Euler two-phase flow. In this approach, the volume-averaged mass conservation equation for each phase is dominated (Wörner 2003). Each phase is modeled as fluids in this model.

The most straightforward way for classifying continuous multiphase flows is to analyze each phase separately. This is referred to as the homogeneous flow model, which

was initially developed in the 1960s by Soviet scientists. For this model, the assumptions are made: the velocity of the gas phase is equal to that of the liquid phase and the thermodynamic stability of the two phases.

4.3.1. Euler-Lagrange Approach

This technique is based on the Eulerian framework being applied to the continuous fluid and the Lagrangian concept being applied to the dispersed phase. The continuous phase is modeled using time-averaged Navier-Stokes equations, while the dispersed phase is modeled through the estimated continuous flow field. With the primary fluid phase, the dispersed phase may interchange momentum, mass, and energy. To determine the state or position of the dispersed phase, ordinary differential equations describing mass, momentum, and energy balances are solved, along with relevant interaction terms to reflect the interaction of the phases with the continuous phase. A crucial premise of this technique is that the dispersed phase occupies a small volume percentage, implying that the dispersed phase parts are not too near and should be viewed as separate (Crowe 2005). Thus, the neighboring element does not affect the mass, momentum, or heat transfer in the Eulerian-Lagrangian method. During the computations, trajectories of the dispersed phase are estimated independently at defined intervals. This model is suitable for simulating particle separation and spray dryers, burning and liquid fuels, and specific particle-laden flows (Wörner 2003).

4.3.2. Euler-Euler Approach

The Euler–Euler model considers a dispersed multiphase flow composed of two or more completely interpenetrating quasi-fluids and is generally classified as the two-fluid model. In this approach, volume averaging is used to generate the two-fluid model. A volume fraction is a critical number that appears in the equation as a result of the averaging. This amount by itself provides no information regarding the size or behavior of the scattered phase, which is often determined using closure models. The Euler–Euler framework is used to simulate both stratified and dispersed flow. The Euler–Euler model is a generic model for most types of multiphase flow, whereas the mixture model is a simpler way of the Euler–Euler model. For stratified flows, the volume-of-fluid model is used. Intuitively, the derivation of the two-phase model is simplest to visualize in terms

of volume averaging. This model employs a smaller volume, considerably smaller than that of large-scale flow structures but much more than that of dispersed particles, where both phases coexist. The volume fraction is expressed in terms of phase distribution and computational volume size. The volume may then be averaged using the locally instantaneous equations characterizing both phases, taking into account the bulk density of every phase (Anderson 1995).

4.4. Fluent in General

Ansys Fluent is a cutting-edge computer application that enables the simulation of fluid flow, heat transport, and chemical reactions in complicated geometries. Ansys Fluent is developed in the C programming language and makes extensive use of the language's flexibility and capability. As a result, true memory management allocation, effective data formats, and dynamic solver control are enabled. Additionally, Ansys Fluent is built on server architecture, allowing it to operate as several concurrent processes on both desktop computers and powerful computing servers. This design enables fast execution, interactive control with total portability across many machine types and operating systems. Ansys Fluent offers total mesh freedom, including that of the ability to solve flow issues utilizing unstructured meshes built with relative ease around complicated geometries. Meshes in two dimensions (triangular/quadrilateral), three dimensions (tetrahedral/hexahedral/pyramid/wedge/polyhedral), and mixed (hybrid) meshes are supported. Additionally, Ansys Fluent allows you to fine-tune or coarse-tune your mesh depending on the flow solutions. You may import your mesh into Ansys Fluent or, for 3D geometries, use Fluent's meshing mode to generate your mesh. The remainder of the procedures are carried out inside Fluent's solution mode, including specifying boundary conditions, defining fluid characteristics, running the solution, optimizing the mesh, and postprocessing and visualizing the results (*ANSYS FLUENT User's Guide* 2021)

In this study, numerical modeling of destratification of temperature stratified water column with aeration is examined. To do this, the turbulence model, multiphase model, and energy equation are the key parameters. In the following sections, these are explained in detail.

4.5. Turbulence Models in Fluent

Turbulence is unstable random motion found in fluids in three-dimensional with high Reynolds numbers ranging from modest to high. Due to the fact that technical flows are often composed of low viscosity fluids, practical flows are turbulent. Numerous quantities of technical significance are dependent on turbulence, such as mixing of momentum, energy, and species; heat transfer; pressure change and efficiency, and forces on bodies. While the Navier-Stokes equations represent turbulence, in theory, it is often not viable to resolve the vast range of time and space scales using Direct Numerical Simulation (DNS) since the CPU requirements would greatly surpass existing computing capacity in the near future. As a result, averaging processes must be performed to the Navier-Stokes equations in order to eliminate all, or at least some, components of the turbulent spectrum. The most often used averaging approach is Reynolds averaging (which is essentially time-averaging) of the equations, which results in the Reynolds-averaged Navier-Stokes (RANS) equations. This method eliminates all turbulent features from the flow, resulting in a smooth fluctuation of the mean velocity and pressure fields. However, the averaging procedure adds new unknown components (Reynolds Stresses and Fluxes) into the transport equations, which must be given by adequate turbulence models. The accuracy of the simulation might be highly dependent on the turbulence model used, and it is critical to make the appropriate model selection as well as to supply an accurate numerical mesh for the selected model. Scale-Resolving Simulation (SRS) models are an alternative to RANS. At least a part of the turbulent spectrum is solved in at least a section of the flow domain using SRS approaches. Although Large Eddy Simulation (LES) is the most well-known of these methods, several novel hybrids (models combining RANS and LES) are emerging. Due to the fact that all SRS approaches need time-resolved simulations with a very tiny time step size, it is critical to note that these methods are much more computationally costly than RANS simulations (*ANSYS FLUENT User 's Guide* 2021)

RANS models are the most cost-effective method for simulating turbulent industrial flows. Typical applications of these models are the k-ω and k-Ɛ models in their many configurations. These approaches reduce the complexity of the issue to the solution of two extra transport equations and include an Eddy-Viscosity (turbulent viscosity) into

the computation of the Reynolds Stresses. There are more advanced RANS models available that directly solve each of the six separate Reynolds Stresses (Reynolds Stress Models - RSM) plus a scaling equation. RANS models are appropriate for a wide variety of engineering applications and often give the requisite degree of accuracy. Due to the fact that none of these models are global, it is necessary to choose which model is best appropriate for a certain application.

Turbulence models are categorized according to which governing equations solving and additional transport equations to those governing equations. All turbulence models can be shown in the “Viscous Model” box in Figure 4.5.

4.5.1. One-Equation Models

4.5.1.1. Spalart-Allmaras Model

The Spalart-Allmaras model is a reasonably basic one-equation model that solves the kinematic viscosity transfer equation. The Spalart-Allmaras model was developed primarily for aerospace applications requiring wall-bounded flows, and it has been shown to provide accurate results for boundary layers exposed to unfavorable pressure gradients. Additionally, it is gaining traction in turbomachinery applications. Avoid using the model as a general-purpose model due to the model's lack of calibration for free shear flows.

4.5.2. Two-Equation Models

These models need the solution of two extra governing equations in order to calculate the turbulence contribution to the mean flow. Beside the Spalart-Allmaras model, the majority of turbulence models used in production CFD are two-equation models. The shear stress transport (SST) and the k-models are two of the most prominent models; nevertheless, there are several additional models included in this caption.

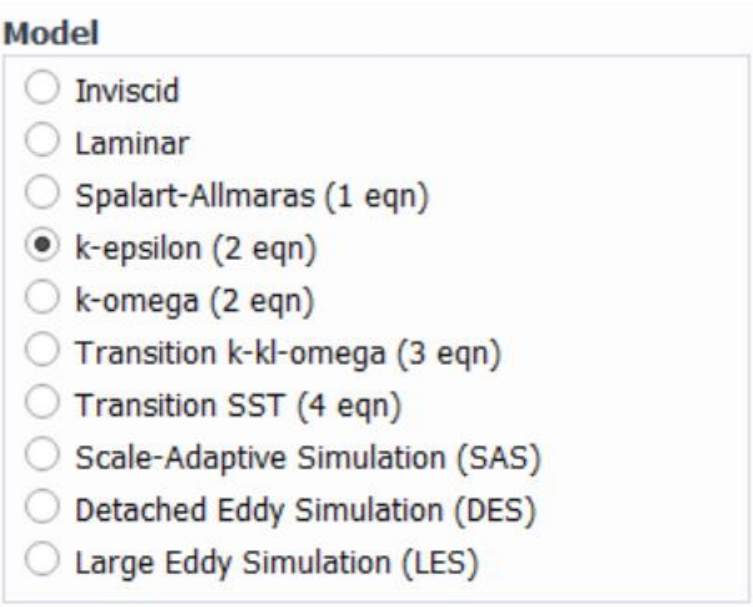

Figure 4.5. Turbulence Models in Fluent

(Source: *ANSYS FLUENT User 's Guide* 2021)

4.5.2.1. Standard k-Ɛ Turbulence Model

This model is based on the idea of the derivation of the standard model while the flow is completely turbulent and that the influence of molecular viscosity is minimal (Launder and Spalding 1972). The conventional model is based on an eddy viscosity model, in which the Reynolds stresses in equation (4.12) are proportional to the average velocity gradients, with turbulent viscosity serving as the constant of proportionality. This was initially presented by Boussinesq, who argued that the momentum transfer produced by turbulent eddies could be described using an effective eddy viscosity in the same manner as the momentum transfer produced by molecular diffusion can be modeled using a molecular viscosity (Schmitt 2008).

k-Ɛ turbulence is the most often used model in Computational Fluid Dynamics for simulating mean flow characteristics under turbulent flow situations. It is a two-equation model that provides a broad description of turbulence via the use of two transport equations. The initial motivation for developing the k-Ɛ model was to enhance the mixing-length model and develop a method for algebraically dictating turbulence scales in moderate to high complexity flows. Also, the ratio of Reynolds stress to mean deformation rate is constant in all directions. The first transferred variable, referred to as turbulent kinetic energy,k, is responsible for determining the energy contained inside the

turbulence. The second transferred variable is turbulence dissipation, Ɛ, which is used to calculate the rate at which turbulent kinetic energy dissipates.

The turbulence kinetic energy and rate of dissipation are computed from the following transport equations:

$$\frac{\partial}{\partial t}(\rho k) + \frac{\partial}{\partial x_i}(\rho k u_i) = \frac{\partial}{\partial x_j}\left[\left(\mu + \frac{\mu_t}{\sigma_k}\right)\frac{\partial k}{\partial x_j}\right] + G_k + G_b - \rho\varepsilon - Y_M + S_k \tag{4.13}$$

and

$$\frac{\partial}{\partial t}(\rho\varepsilon) + \frac{\partial}{\partial x_i}(\rho\varepsilon u_i) = \frac{\partial}{\partial x_j}\left[\left(\mu + \frac{\mu_t}{\sigma_\varepsilon}\right)\frac{\partial \varepsilon}{\partial x_j}\right] + C1_\varepsilon\frac{\varepsilon}{k}(G_k + C_{k3\varepsilon}G_b) - C2_{\varepsilon\rho}\frac{\varepsilon^2}{k} + S_\varepsilon \tag{4.14}$$

In equations (4.13) and (4.14), the terms G_k and G_b are turbulence kinetic energy owing to the mean velocity gradients and buoyancy orderly. Y_M is fluctuating dilatation in compressible turbulence to the overall dissipation rate where S_k and S_ε are source terms and σ_k and σ_ε are the turbulent Prandtl numbers. $C_{1\varepsilon}$, $C_{2\varepsilon}$, $C_{3\varepsilon}$, σ_k and σ_ε are constants and default values are $C_{1\varepsilon}$ =1.44, $C_{2\varepsilon}$ =1.92, σ_k =1.0 and σ_ε =1.3. Values of these are obtained empirically.

Also, turbulent viscosity μ_t is calculated as follows:

$$\mu_t = \rho C_\mu \frac{k^2}{\varepsilon} \tag{4.15}$$

where C_μ = 0.09 is another default value that is found empirically.

4.5.2.2. Standard k-ω Turbulence Model

ANSYS Fluent's basic k-ω model is based on the Wilcox k-ω model (Wilcox 2006) with adjustments to account for low-Reynolds number phenomena, compressibility, and shearing dispersion. One of the Wilcox model's shortcomings is the solution sensitivity to values of k and ω outside of the shear layer. While the revised

formulation in ANSYS Fluent mitigates this reliance, it may still have a considerable influence on the solution, particularly for free shear (Menter 2009).

The standard k-ω model is an empirical model based on transport equations for turbulence kinetic energy,k, and specific dissipation rate,ω, which is also known as the ratio of Ɛ to k (Wilcox 2006).

Over the years, as the k-ω model has been refined, production components have been introduced to both the k and ω equations, increasing the accuracy of the model for forecasting free shear flows.

The turbulence kinetic energy and rate of dissipation are computed from the following transport equations:

$$\frac{\partial}{\partial t}(\rho k) + \frac{\partial}{\partial x_i}(\rho k u_i) = \frac{\partial}{\partial x_j}\left[\Gamma_k \frac{\partial k}{\partial x_j}\right] + G_k - Y_k + S_k \tag{4.16}$$

and

$$\frac{\partial}{\partial t}(\rho \omega) + \frac{\partial}{\partial x_i}(\omega u_i) = \frac{\partial}{\partial x_j}\left[\Gamma_\omega \frac{\partial \omega}{\partial x_j}\right] + G_\omega - Y_\omega + S_\omega \tag{4.17}$$

In equations (4.16) (4.16) and (4.17), the terms G_k and G_ω are turbulence kinetic energy owing to the mean velocity gradients and generation of ω orderly. Γ_k and Γ_ω are effective diffusivities where Y_k and Y_ω are dissipation due to turbulence. S_k and S_ω are source terms again.

Effective diffusivities are obtained as:

$$\begin{aligned} \Gamma_\omega &= \mu + \frac{\mu_t}{\sigma_k} \\ \Gamma_k &= \mu + \frac{\mu_t}{\sigma_\omega} \end{aligned} \tag{4.18}$$

and turbulent viscosity μ_t is calculated as follows:

$$\mu_t = \alpha + \frac{\rho k}{\omega} \tag{4.19}$$

4.5.3. Three and Four Equation Models

4.5.3.1. Transition k-kl-ω Model

This model is usable for predicting boundary layer situations and transitions from laminar to a turbulent regime on that boundary layer (Walters and Cokljat 2008).

This model is classified as three equations because laminar kinetic energy, turbulence kinetic energy, and inverse turbulent time scale are involved in transporting equations.

4.5.3.2. Transition SST Model

The transition SST model is constructed by combining the SST k-w transport equations with two additional transport equations, one for intermittency and one for transition onset criteria, in terms of momentum-thickness Reynolds number. An ANSYS empirical relation has been created to account for typical bypass transitions and flows in low-turbulence freestream situations. Additionally, a handy feature allows you to specify user-defined empirical correlation, which may then be used to influence the transition start momentum thickness Reynolds number equation (*Ansys Fluent Theory Guide* 2021).

4.6. Multiphase Modeling in Fluent

In this chapter, the multiphase model will be discussed in terms of considerations for choosing model types, limitations, and relevant parameters.

4.6.1. Multiphase Model Types

There are four categories as the combination of gas, liquid and solid; gas-liquid or liquid-liquid, gas-solid, liquid-solids, and three-phase flows.

Examples of gas-liquid or liquid-liquid flows are bubble flow, droplet flow, slug slow, and stratified flow. The examples for gas-solid flows are fluidized bed and particle-

laden flow, and also sedimentation and slurry flow are examples for liquid-solid flows. Some of them can be seen in Figure 4.6.

4.6.2. Multiphase Models in Fluent

In this part, available multiphase models in the Euler-Euler approach in Fluent and consideration are discussed to choose a suitable model for the specific cases wanted to be modeled.

4.6.2.1. Model Comparisons and Parameters

For broad, complicated multiphase flows including numerous flow regimes, choose the most interesting part of the flow and then pick the model that is best suited for that feature of the flow. It should be understood that the accuracy of the findings will be lower than for flows with a single flow since the model employed will be valid for just a portion of the modeled flow.

The Volume of Fluid (VOF) model is suitable for stratified or free-surface flows. When the volume fraction of separated and/or dispersed flow exceeds 10%, then mixture and Eulerian models should be applied. If that volume fraction is less or equal to the %10, then the Discrete Phase model, which has the approach of Eular-Lagrangian, should be used.

Besides volume fraction, particulate loading, β is considered a parameter for model choosing because it significantly affects phase interaction.

$$\beta = \frac{\alpha_d \rho_d}{\alpha_c \rho_c} \tag{4.20}$$

where (d) indicates dispersed particle and (c) is for carries phase. And the density ratio of dispersed phase to carrier phase [$\gamma=\rho_d/\rho_c$] is less than 0.001 for gas-liquid flows.

According to particulate loading, the coupling way differs as one-way (low particulate coupling), two-way (intermediate particulate coupling), and four-way. For

high loading, viscous and pressure stress caused by the particles are considered an addition to two-way, then it becomes four-way coupling. For these types, only the Eulerian model gets the correct solution.

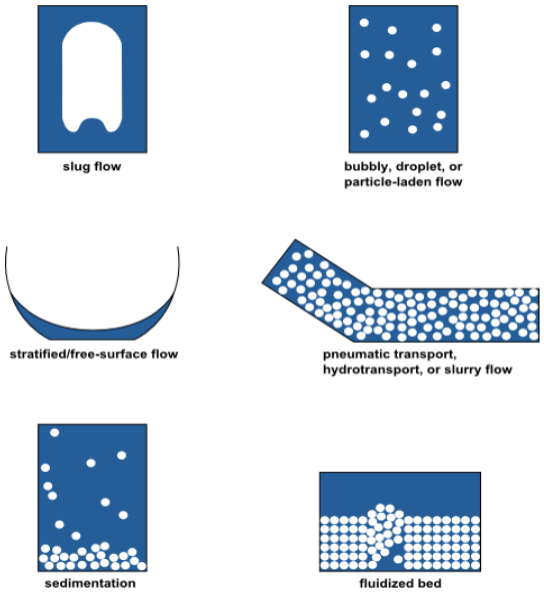

Figure 4.6. Multiphase Flow Regimes

(Source: *Ansys Fluent Theory Guide* 2021)

Another critical parameter is Stokes number to choose between appropriate models for intermediate particular loadings. It is the relation response times between particle and system.

$$St = \frac{\tau_d}{t_s} \tag{4.21}$$

$$\tau_d = \frac{\rho_d d_d^2}{18\mu_c} \qquad t_s = \frac{L_s}{V_s} \tag{4.22}$$

where (s) indicates the system terms and (d) is for dispersed phase.

For St is less than (1.0), discrete phase, mixture, and Eulerian models are available, but in most cases, the mixture model is used due to the having less expensive

computationally. When Stokes number is more than (1.0), particles move independently of the flow, and then the dispersed phase and Eulerian model is applied.

4.6.3. Multiphase Models in Fluent

4.6.3.1. The volume of Fluid Model

The volume of fluid modeling is a method for surface tracking applied to a fixed Eulerian mesh. It is intended for two or more immiscible fluids in which the location of the fluids' interface is of interest. The fluids in the VOF model form a single pair of momentum equations, and the volume fraction for every fluid in each computational cell is monitored throughout the domain. Stratified flows, free-surface flows, filling, sloshing, the motion of big bubbles in a liquid, the motion of liquid after a dam breach, the predicting of jet breakup (surface tension), and the steady or transient monitoring of any liquid-gas interface are all applications of the VOF model.

4.6.3.2. Mixture Model

The mixing model is intended to be used in two or more stages (fluid or particulate). The phases are considered as interpenetrating continua, as in the Eulerian model. In this model for the secondary phase, equations of momentum, continuity, and energy are solved for the mixture, while volume fraction is only for the secondary phase.

In certain circumstances, the mixture model is an acceptable alternative for the classical Eulerian multiphase model. A fully multiphase model may not be possible when the particulate phase is widely distributed or when the phase transition laws are unknown or their trustworthiness is in doubt. A simplified model, such as the mixture model, can operate as well as a full multiphase model while solving fewer variables.

In this model, phases are interpenetration, volume fractions of phases differ between 0 and 1. Also, the velocities of phases can be different; this is the slip velocity concept. If phases have different velocities, this model computes the algebraic expression for relative velocities.

Continuity Equation

$$\frac{\partial}{\partial t}(\rho_m) + \nabla(\rho_m \vec{v}_m) = 0 \tag{4.23}$$

where mass-averaged velocity $\vec{V}_m$ is obtained as:

$$\vec{v}_m = \frac{\sum_{k=1}^{n} \alpha_k \rho_k \vec{v}_k}{\rho_m} \tag{4.24}$$

Where ρ_m is the mixture density and α_k is the volume fraction of the phase.

Momentum Equation

It can be expressed as the summation of individual momentum equations of phases.

$$\frac{\partial}{\partial t}(\rho_m \vec{v}_m) + \nabla(\rho_m \vec{v}_m \vec{v}_m) = -\nabla p + \nabla[\mu_m(\nabla \vec{v}_m + \nabla \vec{v}_m^T)] + \rho_m \vec{g} + \vec{F} + \nabla\left(\sum_{k=1}^{n} \alpha_k \rho_k \vec{v}_{dr,k} \vec{v}_{dr,k}\right) \tag{4.25}$$

where (n) indicates the number of phases, $\vec{F}$ is a body force. $\vec{v}_{dr,k}$ is secondary phase drift force and μ_m is the mixture viscosity, and they are obtained as:

$$\mu_m = \left(\sum_{k=1}^{n} \alpha_k \mu_k\right) \tag{4.26}$$

$$\vec{v}_{dr,k} = \vec{v}_k - \vec{v}_m \tag{4.27}$$

Slip Velocity Calculation

As mentioned before, the mixture model allows the phases have different velocities. The ratio of the secondary phase (p) velocity to primary phase (q) velocity is defined as slip velocity.

$$\vec{v}_{pq} = \vec{v}_p - \vec{v}_q \tag{4.28}$$

To calculate slip velocity, the formulation expressed by Manninen 1996 is applied

$$\vec{v}_{pq} = \frac{\tau_p}{f_{drag}} \frac{(\rho_p - \rho_m)}{\rho_p} \vec{a} \tag{4.29}$$

where particle relaxation time, τ_p is calculated as:

$$\tau_p = \frac{\rho_p d_p^2}{18\mu_q} \tag{4.30}$$

where (d) and $\vec{a}$ indicate the diameter and acceleration of the secondary phase (p).

And the drag function in equation (4.29) is obtained as (Hank 2011):

$$f_{drag} = \begin{cases} 1 + 0.15Re^{0.687} & Re \leq 1000 \\ 0.0183Re & Re > 1000 \end{cases} \tag{4.31}$$

And the acceleration is as follows:

$$\vec{a} = \vec{g} - (\vec{v}_m \nabla)\vec{v}_m - \frac{\partial \vec{v}_m}{\partial t} \tag{4.32}$$

4.6.3.3. Eulerian Model

The Eulerian model is the most sophisticated of the multiphase models. Each phase of this model is solved using continuity and momentum equations separately. The coupling process makes use of pressure and interphase transfer coefficients. This coupling is handled differently based on the different phases; only fluid flows and fluid-solid fluxes are treated differently. The characteristics of fluid-solid fluxes are determined using kinetic theory. The kind of mixture being represented also has an effect on the interchange of momentum between the phases. Eulerian multiphase models have been used for fluidized beds, sediment-laden flow, and air bubble water columns.

Volume Fraction Equation

Volume fraction states that the space is ranked as from each phase, and equations are solvers individually for each phase with local instantaneous balance.

The volume fraction of phase q is obtained as follows:

$$V_q = \int_V \alpha_q dV \tag{4.33}$$

where

$$\sum_{q=1}^{n} \alpha_q = 1 \tag{4.34}$$

and the effective density of secondary phase,q is as:

$$\hat{\rho}_q = \alpha_q \rho_q \tag{4.35}$$

Conservation of Mass Equation

The general form of the equation is written in equation (4.23), and it is revised in ANSYS Fluent for the Eulerian multiphase model as shown in equation ((4.37).

$$\frac{\partial}{\partial t}(\alpha_q \rho_q) + \nabla (\alpha_q \rho_q \vec{v}_q) = \sum_{p=1}^{n} (\dot{m}_{pq} - \dot{m}_{qp}) + S_q \tag{4.36}$$

where mass flux in the equations represents the mass transfer between phases, $\vec{v}_q$ is the velocity of phase,q. And the last term, S_q, is zero as default, but it allows to add source term with UDF(User Defined Functions).

$$\frac{1}{\rho_{rq}} \left(\frac{\partial}{\partial t}(\alpha_q \rho_q) + \nabla (\alpha_q \rho_q \vec{v}_q) = \sum_{p=1}^{n} (\dot{m}_{pq} - \dot{m}_{qp}) + S_q \right) \tag{4.37}$$

where ρ_{rq} is the phase reference density.

Conservation of Momentum Equation

For phase q, the momentum balance is computed in general form as:

$$\frac{\partial}{\partial t}(\alpha_q \rho_q \vec{v}_q) + \nabla(\alpha_q \rho_q \vec{v}_q \vec{v}_q) = -\alpha_q \nabla p + \nabla \bar{\bar{\tau}}_q + \alpha_q \rho_q \vec{g} + \sum_{p=1}^{n} (\vec{R}_{pq} + \dot{m}_{pq} \vec{v}_{pq} - \dot{m}_{qp} \vec{v}_{qp}) + (\vec{F}_q + \vec{F}_{lift,q} + \vec{F}_{wl,q} + \vec{F}_{vm,q} + \vec{F}_{td,q}) \quad (4.38)$$

where $\vec{F}_q$, $\vec{F}_{lift,q}, \vec{F}_{wl,q}, \vec{F}_{vm,q}, \vec{F}_{td,q}$ are the forces that represent the external body, lift, wall lubrication, virtual mass, and turbulent dispersion forces. $\vec{R}_{pq}$ is interaction force, and p is shared pressure. Also, the term of $\bar{\bar{\tau}}_q$, the stress-strain sensor of the qth phase.

Then the equation (4.38) is revised for fluid-fluid momentum equations in ANSYS Fluent as follows:

$$\frac{\partial}{\partial t}(\alpha_q \rho_q \vec{v}_q) + \nabla(\alpha_q \rho_q \vec{v}_q \vec{v}_q) = -\alpha_q \nabla p + \nabla \bar{\bar{\tau}}_q + \alpha_q \rho_q \vec{g} + \sum_{p=1}^{n} (\vec{K}_{pq}(\vec{V}_p - \vec{V}_q) + \dot{m}_{pq} \vec{v}_{pq} - \dot{m}_{qp} \vec{v}_{qp}) + (\vec{F}_q + \vec{F}_{lift,q} + \vec{F}_{wl,q} + \vec{F}_{vm,q} + \vec{F}_{td,q}) \quad (4.39)$$

4.7. Energy Modeling in Fluent

This chapter provides the energy equation details in Fluent. Heat transfer refers to the flow of thermal energy of matters in different occupied regions. Conduction, convection, and radiation are the mechanisms of the heat transfer concept. Fluent allows to solve all of them but also requires computational effort for some cases.

4.7.1. Modeling Conductive and Convective Heat Transfer

Simulating heat transfer within liquids and/or solids is related to this sub-model of Fluent. When the Fluent energy equation is activated in the “Models” box, it is necessary to make some arrangements such as boundary conditions and material properties.

The energy equation is solved for the following form:

$$\frac{\partial}{\partial t}(\rho E) + \nabla.\left(\vec{v}(\rho E + p)\right) = \nabla\left(k_{eff}\nabla \mathrm{T} - \sum_j h_j \vec{J}_j + \left(\bar{\bar{\tau}}_{eff}.\vec{v}\right)\right) + S_h \qquad (4.40)$$

where $\vec{J}_j$ are the diffusion flux and the effective conductivity, k_{eff} is the summation of turbulence diffusivity (k) and turbulent thermal conductivity (k_t). S_h is the additive heat source that has a default value of zero.

The term (E) in equation (4.40) is obtained as:

$$E = h - \frac{p}{\rho} + \frac{v^2}{2} \qquad (4.41)$$

where h is the sensible energy that changes for ideal gas and incompressible flows.

4.7.2. Arrangements for Energy Equation Model

As mentioned before, when the energy equation is activated, some updatings for materials and boundary conditions are necessary.

For boundary conditions, temperatures must be specified for inlets and exits of the domain. Also, for boundary conditions for walls, some thermal conditions can be assigned, such as specified heat flux and temperature, convective heat transfer, etc.

Fluent allows to change and arrange for material properties based on temperature changes such as defining density and viscosity depending on the temperature.

Another essential point for the energy equation is limiting the temperature values for the stability of the solution. The temperature ceiling and floor are used to increase the stability of simulations in which the temperature must physically remain within certain ranges. Occasionally, intermediate solutions to the equations result in temperatures beyond these limitations, for which property definitions. Temperature limits ensure that temperatures remain within the range expected for your situation. If the Ansys Fluent computation forecasts a temperature greater than the upper limit, the stored temperature data are pegged to this upper limit and reported in consol during simulation.

4.8. Summary

In this study, destratification of temperature stratified water column by air bubble was modeled. The numerical models were generated and solved in ANSYS Fluent Student Version 2021. For this study, the turbulence, multiphase, and energy equation models are essential concepts for obtaining an accurate solution. Thus this chapter is necessary to understand for getting solutions as precise as possible from the numerical models.

Some experiments were carried out in the Hydraulics Laboratory in İzmir Institute of Technology to verify the model results. Experiment setup and results will be discussed in Chapter 3.

According to experiment results, sub-models and parameters of numerical models were changed and updated to get the closest results with some assumptions and limitations. Detailed information about numerical modeling will be discussed in the following Chapter 5.

As a turbulence model, k-Ɛ, k-ω, and Reynolds stress (RSM) models were tested with some variations. After some trials, it was decided that the k-ω turbulence model gets more relevant results with the experiments.

There were two suitable options for the problem descriptions as a multiphase model: the Mixture and Eulerian models. Both of them were applied with different boundary conditions and variations. After lots of trials, it was observed that the Eulerian multiphase model gets more similar results with the experiments.

To create temperature stratification in the water tank in the model, the energy equation model was used in Fluent. Inlet, outlet, and wall boundary conditions were set according to experimental data. Some regions were created in the water column for temperature stratification, and initial values were assigned to these regions. Depending on the observations during experiments, the necessary temperature limitations were also set to model to get the stability of solutions.

CHAPTER 5

NUMERICAL SETUP

5.1. Fluid Domain

This study aims to simulate the mixing process of thermally stratified water column in a tank by air bubble plume under different conditions. Reference values are set, and numerical models were calibrated based on the observations obtained from the experiments conducted in the laboratory. As described in Chapter 3, experiments were carried on in a tank having dimensions of 1m*1m*1m, and the water height was kept at 0.94 meters during the experiments. Since the cooling pipes were placed at the bottom of the tank, the flow area corresponding to the 6 cm measured from the bottom was not taken into account in the numerical model. Hence, when generating the fluid domain in the numerical model, the water height of 88 cm having the same cross-sectional area as the experiment setup was considered.

5.2. Generation of the Model Geometry

The first step in creating a project in ANSYS Fluent is to create geometry that has many ways. Generally, CAD programs are used to create a geometry later on imported to ANSYS software. However, it is essential to note that CAD programs do not have the ability to develop whole matching geometry for CFD such as nuts, thickness, etc. Due to these extra arrangements and the simplicity of the geometry of this study, geometry was accomplished using a DesignModeler, the component system of ANSYS Workbench. DesignModeler includes a plethora of features and tools for creating a 2D or 3D model of the system under examination. While a two-dimensional model is simpler to construct, it cannot be used to solve all types of problems (Andersson 2012). Due to the nature and complexity of this study and the situation being examined, it is necessary to create a 3D model, which will require additional computational power and longer simulation times.

To compare the effects of different air diffuser diameters and numbers of the plume, some variable model geometries were obtained but in the same way, as explained in this section. A 1m*1m cross-section area was drawn on the XZ plane (Figure 5.1) for 2-D geometry to obtain model geometry.

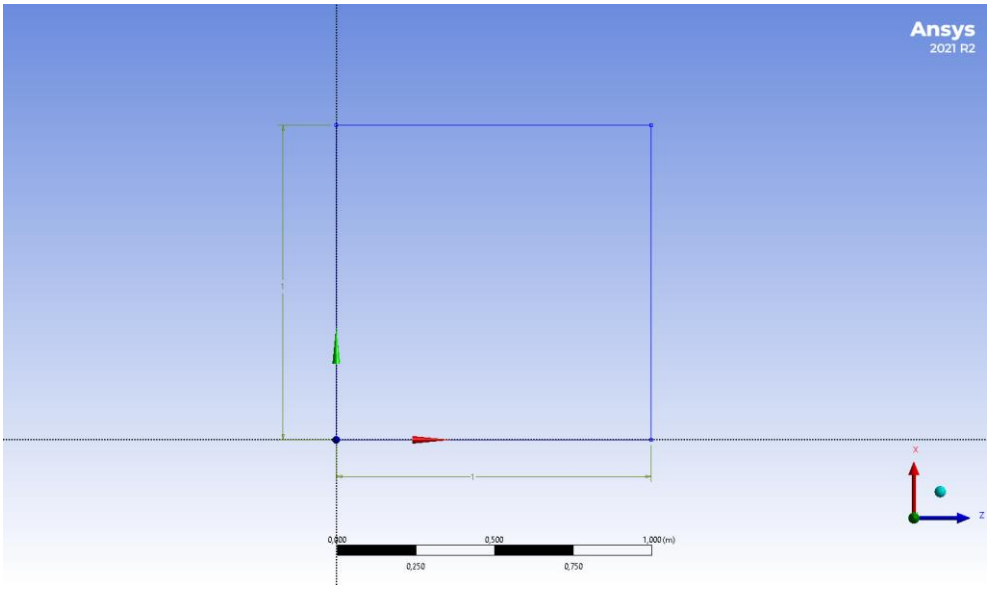

Figure 5.1. 2D body of fluid domain in ANSYS DesignModeler

The resulting surface area was extruded 0.88 meters to construct a 3-D fluid domain via the “Extrude” command (Figure 5.2).

To create the part of the air diffuser of the model geometry, a circle called “Sketch 2” was drawn in the middle of the lowest tank, again in the XZ plane, and extruded 0.06 meters in the Y direction to mimic the experimental setup. Model geometry was generated as two separate bodies because they will be initialized with different values for air volume fraction and temperature. These two individual bodies were also classified as a single part in the geometry section to overcome some errors in meshing Fluent solver. Also, it is essential to create names of bodies in the geometry section so that mesh and Fluent solver describe the sections. (Figure 5.3).

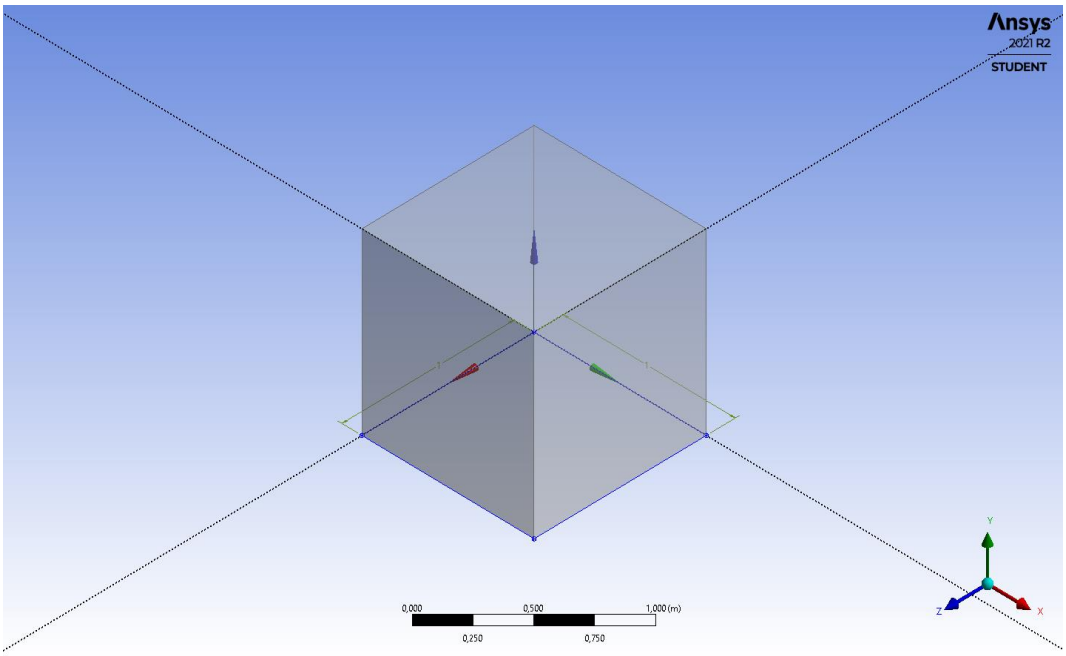

Figure 5.2. 3-D body of fluid which has obtained via the “Extrude” command

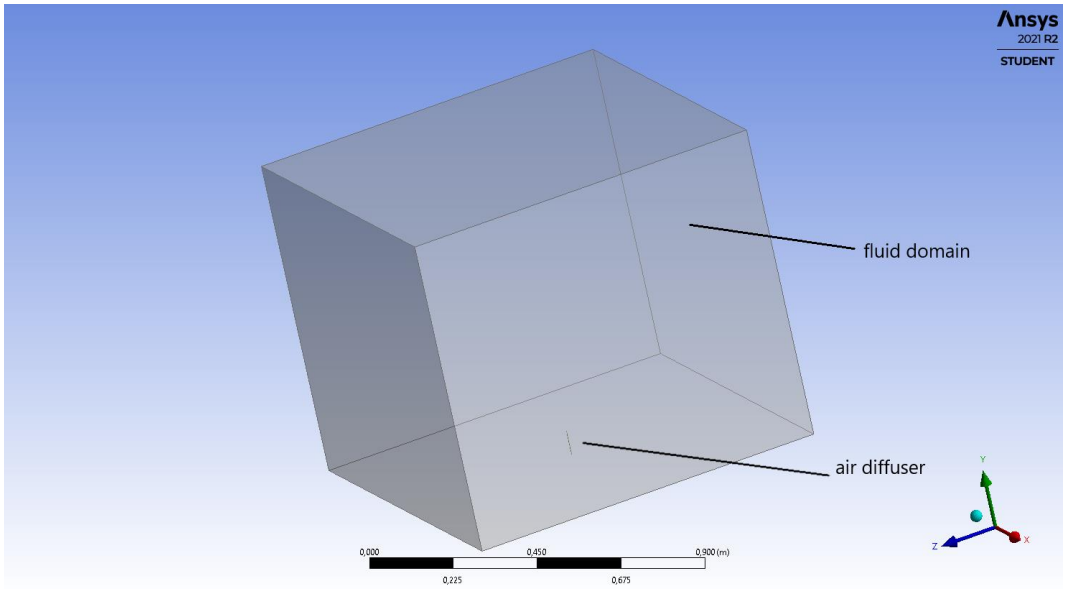

Figure 5.3. Model geometry with air diffuser

5.3. Generation of the Mesh

The principle of meshing is to divide the domain into smaller pieces called "cell/node" to solve equations in each element for accurate results. Meshing the geometry is a critical aspect of ensuring the validity of the simulations and results. This can be accomplished in a variety of ways, and certain areas of the geometry will require a finer mesh to capture particularly interesting flows. The student edition of ANSYS Fluent used in this project has a limit of 512000 cells or 512000 nodes, resulting in some meshing limitations. Additionally, a finer mesh will increase the computational cost of the simulations and result in a longer simulation time. The software includes a variety of meshing tools suitable for a variety of geometries and expected simulation behavior. These mesh types can also be created as a combination. Some basics of cell shapes to mesh can be seen in Figure 5.4.

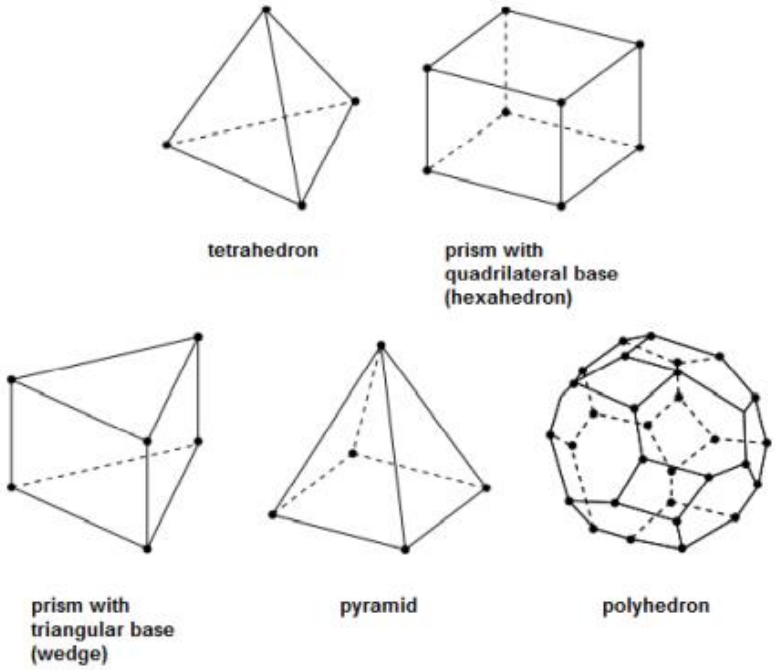

Figure 5.4. Mesh types

(Source: *ANSYS FLUENT User 's Guide* 2021)

5.3.1. Mesh Quality

The mesh quality is critical for the accuracy and stability of numerical computation. Regardless of the type of mesh used in your domain, it is critical to maintain the quality of the mesh. A critical indicator of mesh quality that Ansys Fluent enables to check is a value called “orthogonality.” For every face “i,” orthogonality is calculated in these following equations:

$$\frac{\vec{A}_i \, \vec{f}_i}{|\vec{A}_i \, ||\vec{f}_i \,|} \tag{5.1}$$

$$\frac{\vec{A}_i \, \vec{c}_i}{|\vec{A}_i \, ||\vec{c}_i \,|} \tag{5.2}$$

where;

$\vec{A}_i$ is the normalized dot product of the area vector of a face,

$\vec{f}_i$ is a vector from the centroid of the cell to the centroid of that face,

$\vec{c}_i$ is a vector from the centroid of the cell to the centroid of the adjacent cell that shares that face.

The concept of orthogonality is used to compute the orthogonal quality, which is a method for checking the quality of the mesh. Orthogonal quality approaching 1 means the cells are acceptable, while approaching 0 indicates poor quality mesh, which is undesirable.

Another criteria for mesh quality is the concept of skewness which means the difference in shape between a cell’s shape and that of an equilateral cell of equivalent volume. It is sized up from 0 to 1, where closest to 0 refers to excellent.

5.3.2. Mesh Applications for this Study

Before getting started to meshing, it is essential to describe the name of the bodies or parts of the domain so that some automatic configurations are done according to the name. Naming was done by face selection. The bottom and sides of the tank and also

inner diffuser sides were named as “walls,” the upper face of the tank as “outlet,” and the bottom face of the diffuser body as “inlet_air” (Figure 5.5).

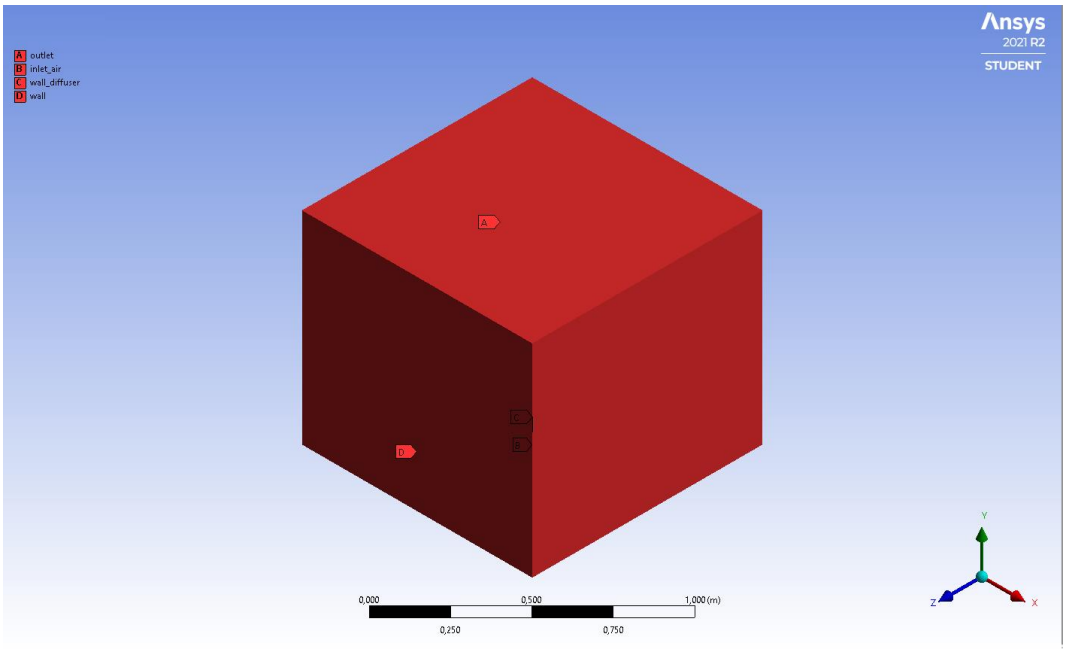

Figure 5.5. Named surfaces of geometry

After describing names, the “Create Automatic Connections” section was activated to define continuous mesh for the interface between the inner tank body and wall diffuser. Later on, meshing was done for fluid domain and air diffuser bodies separately because of the very different sizes between them.

For the “FluidDomain” part, the “Hex Dominant” mesh method was applied, while the “air diffuser” part was the “Sweep” method. In this study, the “Hex Dominant” mesh application was essential because that the Eulerian multiphase model can be applied for this type of mesh (*ANSYS FLUENT User’s Guide* 2021). Element sizes were adjusted for each part according to the number of elements limitations on ANSYS Student Version and mesh quality criteria. Last for all, the average orthogonal quality and skewness were 0.995, and 0.0472 orderly with the total number of elements was about 450000; details can be seen in Table 5.1. Plan view of meshed geometry (Figure 5.6) and sectional view of meshing (Figure 5.7) can be seen.

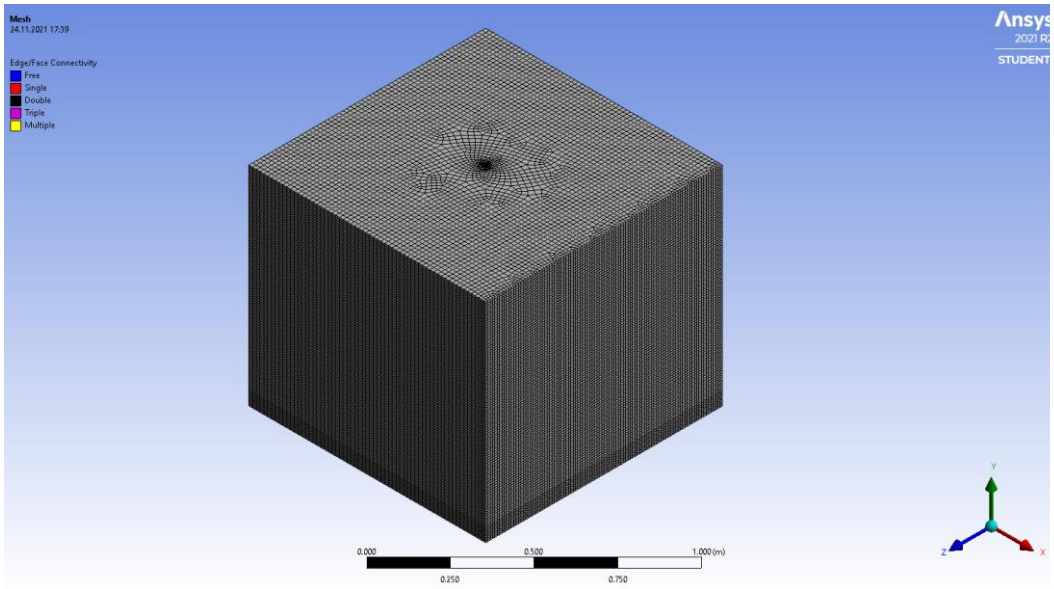

Figure 5.6 Plan view of meshing

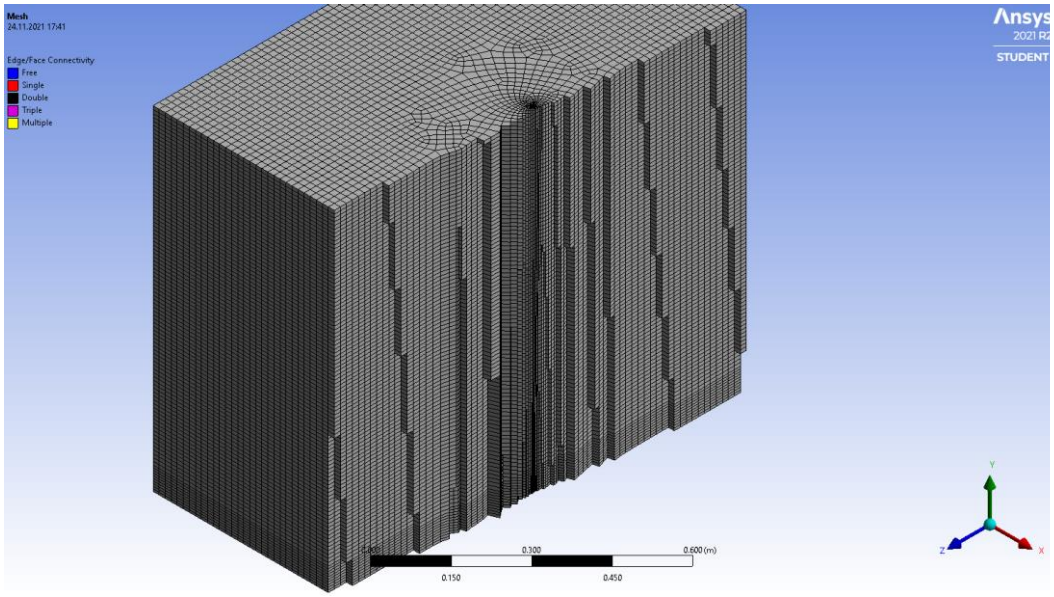

Figure 5.7. The sectional view of the meshed body

Overview of geometry and mesh is given in Table 5.1.

5.4. Solver and Setup

After meshing is completed, the domain is posted to Fluent solver to assign the sub-models, materials, boundary conditions, materials, and other necessary arrangements.

Table 5.1. Properties of Geometry and Mesh

	Fluid Domain	Air Diffuser	All Domain
Dimensions	1m * 1 m cross-section 0.88 m depth	0.002 m diameter 0.06 m length	-
Volume	0.88 m^3	2.04e-07 m^3	0.88 m^3
Method	Hexa Dominant	Sweep	MultiZone
Nodes	-	-	468996
Elements	-	-	449316
Minimum Orthogonal Quality	-	-	0.5587
Maximum Orthogonal Quality	-	-	1
Average Orthogonal Quality	-	-	0.9951
Minimum Skewness	-	-	4.51E-09
Maximum Skewness	-	-	0.696
Average Skewness	-	-	4.72E-02

5.4.1. General

In Fluent, the solver type was chosen as “pressure-based” and “transient.” The gravitational acceleration was set as -9.81 m^2/s in the Y direction.

5.4.2. Applied Sub-Models

In this study, the Eulerian multiphase model was applied that gives best matches with the experimental results. Besides that, the mixture multiphase model was also

applied. The examining and comparison of these two multiphase models will be made in another part. In the Eulerian multiphase model, properties are given in Table 5.2.

Table 5.2. Multiphase Model Settings

	Multiphase Model
Type	Eulerian
Volume Fraction Parameters	Implicit
Number of Phases	2
Phase-1 (primary)	Water
Phase-2 (secondary)	Air, with a constant diameter
Phase Interaction	Forces Drag Force schiller-naumann
	Interfacial Area ia-particle

For phase-2, air diameter was chosen as constant as bubble diameter concerning experimental measurements. Thus, for all cases that used different air diffuser diameters, this value was updated.

The energy equation was activated in the “Models” box for the temperature option.

The turbulence model was selected as the SST k-ω model with default model constants. But also other options for turbulence models, k-Ɛ (2-equation) and Reynolds Stress (7-equation), were tested to observe the effects of turbulence models and will be discussed in another chapter.

5.4.3. Materials used in the Model

As can be mentioned above, there are two phases as water and air. Properties of materials are given in Table 5.3.

Default values were set for air, but some adjustments were made for water as temperature changes are essential in this study. These were properties of density, viscosity, and specific heat.

In the Fluent material database, the default density of water is 998 kg/m^3. To input to model the exact density of water in the experiments, density measurements were done. Besides the density of the water in the experiment, another important point was to define the density change depending on the temperature. At this point, a formulation of density depending on temperature was obtained. To do this, water examples are taken from the tank at different temperatures. With the help of the apparatuses of a pycnometer of 100ml and precision balance, measurements were carried out for seven different temperatures, as in Table 5.4.

Table 5.3 Properties of Materials

	Water	Air
Density (kg/m^3)	polynomial	1.225
Specific Heat (J/kgK)	5000	1006.43
Thermal Conductivity	0.6	0.0242
Viscosity (kg/(ms))	sutherland	1.79E-05
Molecular Weight (kg/mol)	18.0152	28.966
Standard State Enthalpy (J/kgmol)	-2.86E+08	0
Reference Temperature (C)	20	20

Table 5.4 Density of water measurements

Temperature (°C)	Mass of Water (gr)	Volume of Tare (ml)	Mass (kg)	Volume (m^3)	Density (kg/m^3)
5.95	105.3	100	0.1053	0.0001	1053
15.15	105.2	100	0.1052	0.0001	1052
19.15	105.1	100	0.1051	0.0001	1051
23.15	105	100	0.105	0.0001	1050
29.15	104.8	100	0.1048	0.0001	1048
31.55	104.8	100	0.1048	0.0001	1048
43.25	104.2	100	0.1042	0.0001	1042

As a result, the equation of density with temperature changes was obtained as follows:

$$\rho = -0.0064T^2 + 3.4926T + 573.25 \quad (5.3)$$

This equation was set as the density of water to the solver, as can be seen in Figure 5.8.

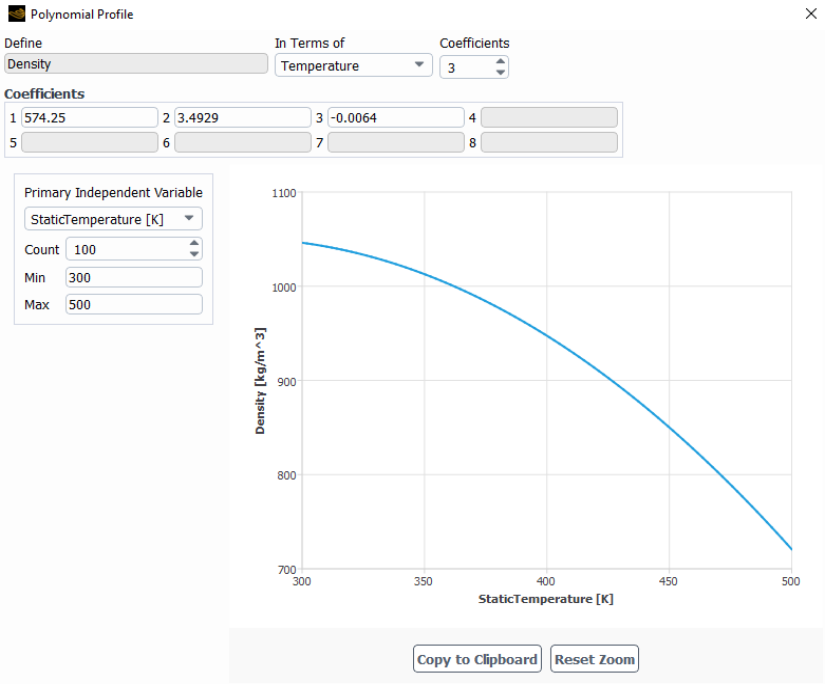

Figure 5.8.The equation of density of water in Fluent

Another property of water that was changed depending on temperature was viscosity. For this, the "sutherland law" was used in Fluent, reference viscosity at reference density, and temperature values of maximum and minimum were introduced (Figure 5.9).

5.4.4. Boundary Conditions

In this section, boundary conditions that applied to the model are explained. Some of the available boundary conditions in the Eulerian multiphase model and features are listed in

Table 5.5.

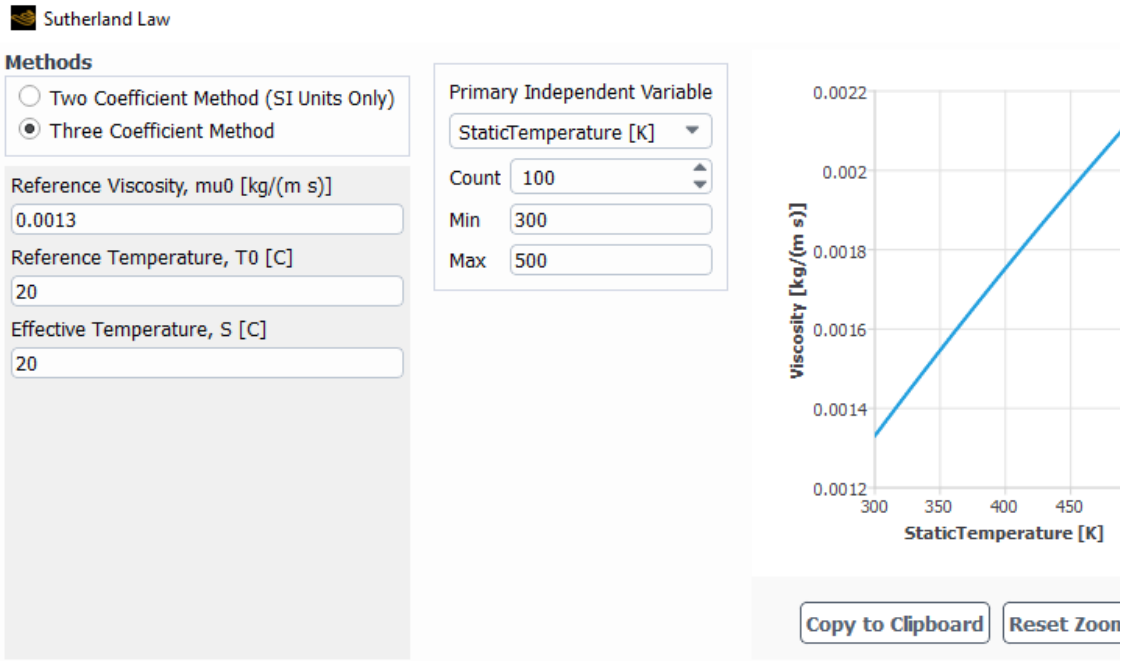

Figure 5.9. The viscosity of water in Fluent

5.4.4.1. Inlet Boundary Conditions

In this study, only air enters the water-filled tank, so the bottom face of the "air diffuser" body was assigned for air entrance. The mass-flow inlet boundary condition was applied for this face because it is the best option for compressible flow enterings. For the Eulerian multiphase model, boundary conditions for phases are defined separately. In this problem description, the water flow rate was set as zero, where the air was selected as a constant value in the positive Y direction. The mass-flow inlet value was assigned according to the experimental setup. With the flow rate, also air temperature was defined as room temperature during experiments. Because the values vary according to the modeled experimental data, they are different for each comparison and will be described

in their own section. But the mass-flow inlet boundary condition is constant for all models.

Table 5.5. Boundary conditions and features

Boundary Conditions		Features
For flow enters and exits	Velocity inlet	To define the velocity and scalar variables
	Pressure inlet	To define the pressure and other scalar features
	Mass-flow inlet	To define a mass flow rate for compressible flows
	Pressure outlet	To define pressure at outlets and other scalar features
	Outflow	Suitable for situations that pressure and velocity are not known
	Degassing	Suitable where the dispersed phase leaves the domain but continuous phase not
For walls	Wall	To bound the regions
	Symmetry	Suitable for the region shows mirror symmetry for solution

5.4.4.2. Outlet Boundary Conditions

It is the essential criteria for the simulations of destratification via bubble column. Other outlet boundary condition options such as mass-flow outlet and symmetry showed that when the given air does not leave the system as observed in the experimental setup,

there are serious time inconsistencies in the mixing process compared to the experimental data. And other boundary condition comparisons mentioned will be discussed in the following sections. For only the Eulerian multiphase model, there is an option to satisfy this condition called “degassing” boundary conditions. In principle, this boundary condition allows only dispersed phase, which is air in this study, to escape from the boundary surface. When air leaves the domain, the mixing process is closer to the actual applications.

Table 5.6 Solution method and spatial discretizations

Solution Methods	
Pressure-Velocity Coupling	Coupled
Spatial Discretization	
Gradient	Least Squares Cell-Based
Pressure	Body Force Weighted
Momentum	Second Order Upwind
Volume Fraction	Second Order Upwind
Turbulent Kinetic Energy	Second Order Upwind
Specific Dissipation Rate	Second Order Upwind
Energy	Second Order Upwind
Transient Formulation	Second Order Upwind

5.4.4.3. Walls Boundary Conditions

Walls are the boundary conditions that bound the flow domain with some arrangements. In this study, there are two types of walls as inner and outer. The outer walls were defined as stationary walls. For the thermal condition, heat flux was selected.

The internal wall refers to a wall between the parts of the “air diffuser” and “fluid domain,” and “coupled” was chosen for thermal condition.

5.4.5. Solution of the Model

Solution method, spatial discretization methods, control, and limit parameters are assigned in this part. The methods that were used are listed in Table 5.6.

5.4.5.1. Controls and Limitations

Solution control values are listed in Table 5.7.

Table 5.7 Solution Control Values

Solution Controls	
Flow Courant Number	40
Explicit Relaxiation Factors	
Momentum	0.75
Pressure	0.75
Under-Relaxiation Factors	
Density	1
Body Forces	1
Volume Fraction	0.50
Turbulent Kinetic Energy	0.80
Spesific Dissipation Rate	0.80
Turbulent Viscosity	1
Energy	1

Besides that, a critical case is to assign limits to temperature for maximum and minimum values in solution control for models in that the energy equation is activated, as can be mentioned in the numerical methodology part. In this study, the temperature was limited from 0 ˚C to 40˚C based on the observations during experiments.

5.4.6. Initial Conditions

After the solution is initialized, the initial conditions can be assigned to the model. In this study, initial temperature values were set to the model based on the temperature values in experiments. As mentioned in the experimental setup chapter, there are six points where temperature data were read and recorded: at the depths of 5cm, 15cm, 30cm, 50cm, 70cm, and 85cm. To set temperature data to model, regions as volume were created in the water column and input as initial conditions. Except for these six points, the temperatures of other locations are not known as the exact values, so approximate values were set for the other locations on models. Location details are given in Table 5.8.

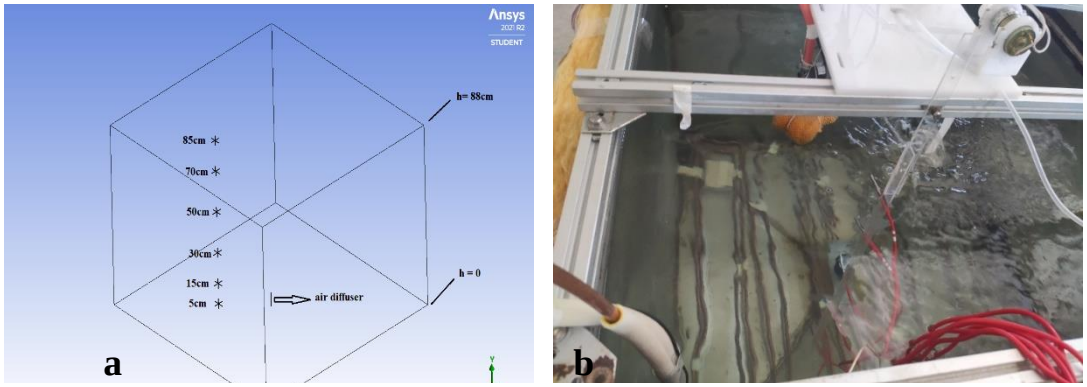

Figure 5.10. Locations of measuring points in the numerical (a) and experimental studies (b)

The measuring points in the numerical model and experiments can be seen in Figure 5.10. These measuring points were selected as it is because if it would be closer to the air diffuser, the measured temperatures can be misleading to observe the mixing process. In addition, if it would be closer to the walls, the wall boundary could affect the results.

5.4.7. Time Step Size and Simulation Time of the Model

Each model was run for 600 or 800 seconds with changing time step sizes. Generally, the first one minute was run with the time step size of 0.005 for the stability of the solution. Later on, the time was size increased gradually to 0.1 as maximum, and 20 iterations for all time step sizes.

Table 5.8 Locations of regions on the model and recorded data of experiments

Regions	Locations on models (m)	Locations of recorded data (m)
region-12	0.88 0.825	0.85
region-11	0.825 0.775	-
region-10	0.775 0.725	-
region-9	0.725 0.7m 0.675	0.7
region-8	0.675 0.525	-
region-7	0.525 0.5 0.475	0.5
region-6	0.475 0.325	-
region-5	0.325 0.3 0.275	0.3
region-4	0.275 0.175	-
region-3	0.175 0.15 0.125	0.15
region-2	0.125 0.075	-
region-1	0.075 0.05 0.025	0.05
region-0	0.025 0	-

5.4.8. Summary of Numerical Model Generation

This chapter summarizes the steps followed to generate a numerical model for simulation of the hydrodynamics of the mixing process of the thermally stratified water columns by air diffuser.

Geometry was generated in 3D and as a full scale of the water tank used in the experimental observations. Two bodies were achieved and defined separately: the “fluid domain” and “air diffuser” represent the water tank and air diffuser in experiments.

The meshing of the domain was performed in “sweep” for the air diffuser body and “hex dominant” for the fluid domain to obtain mesh cells in the shapes of hexahedrons due to the mesh type limitation of the Eulerian multiphase model application (*ANSYS FLUENT User’s Guide* 2021). The generated mesh consists of approximately 449316 cells. Regarding the mesh quality, average skewness and orthogonal quality criteria were considered, which were 0.047 and 0.9951 orderly. These two mesh quality criteria are evaluated between 0 and 1, where if the average skewness value approaches 0 and the orthogonal quality value approaches 1, the model is considered to have good mesh quality.

The simulation of the mixing process of the thermally stratified water column by air diffuser encloses the multiphase and turbulence models and energy equation application in Fluent. The SST k-ω turbulence model for the mixture was utilized with the default values. The Eulerian multiphase model was also applied with two phases: water and air. The water was defined as the primary phase, and the air was dispersed with a constant diameter.

Material properties of water and air, the two phases of the multiphase flow must be defined in the model. The density of air was taken as constant and equal to 1.225 kg/m3 whereas the density of water was specified as a function obtained from the sampling of the thermally stratified water in the tank before the experiments. Water density was assumed to depend on only temperature; thus, a formula describing the relationship between the water density and temperature (Equation (5.3) was specified. The temperature profile given in Figure 5.8 was input to Fluent. The viscosity of the water was defined using “Sutherland law” utilized in Fluent, where both observed maximum

and minimum temperature values and a reference viscosity have to be defined prior to the simulations.

As for the boundary conditions, the mas-flow inlet was assigned for the bottom face of the “air diffuser” body to allow air entrance to the fluid domain. The side and bottom faces of the body of the “fluid domain” were defined as stationary walls, and heat flux was defined as temperature property. The degassing boundary condition was used for the outlet boundary condition, which was found to be the most appropriate boundary condition for simulation of destratification via bubble column in the application of the Eulerian multiphase model. Only the dispersed phase, which was air in this study, is allowed to escape from the top boundary surface due to this boundary condition. When air exits the domain, the mixing process in simulation becomes more reflective of the actual applications.

The numerical model was performed in double precision due to the absence of multiphase flow application, and the solution was performed as transient flow. Solution method of pressure velocity coupling was chosen as coupled with the courant number of 40. Spatial discretization methods for solving the equation were applied as second-order upwind to increase the accuracy of the solution. In applying the energy equation, the temperature was limited for the stability of solution in the solution control limits panel, as in the range from 0˚C to 40˚C according to observations on the experiments.

CHAPTER 6

COMPARISON OF THE NUMERICAL MODELS WITH THE OBSERVATIONS

In this chapter, simulated numerical models and comparisons of them with the experimental observations will be discussed. To ensure the validity of the model, comparisons were made with four different experiments: air diffuser with the diameters of 2 mm,3 mm, and 4 mm with the flow rate of 400 l/h and also air diffuser with the diameter of 2 mm with the air flow rate of 200 l/h. Since this study aims to examine the mixing process of temperature stratified water columns, temperature values of the exact location at the same time were the main parameter used for comparison. The overview of the changed parameters for models and experiments can be shown in Table 6.1.

Table 6.1 The overview of changed parameters for the models with experiments

	Same Parameters for Experiments and Models			In Experiments	In Models
Code	Diameter of Air Diffuser (mm)	Bubble Diameter (mm)	Initial Temperature (˚C)	Air Volume Flow Rate (l/h)	Air Mass Flow Rate (kg/s)
2D400F	2	12	Table 6.2	400	4.54E-05
3D400F	3	15	Table 6.4	400	4.54E-05
4D400F	4	18	Table 6.6	400	4.54E-05
2D200F	2	12	Table 6.8	200	2.30E-05

6.1. Single Hole Air Diffuser having Diameter of 2mm and with 400 l/h Air Flow Rate, 2D400F

The first model and experiment comparison is for an air diffuser with a 2mm diameter and air flow rate of 400 liters per hour. The model was generated as explained in Chapter 5. Only bubble diameter, initial conditions for temperature distribution, and boundary conditions of air for mass-flow inlet were set according to the experiment.

Air flow rate, volume flux, was 400 liters per hour in the experiments, and in Fluent, air entrance was set in terms of mass flux. For this reason, the equation was used, assuming that the density of air is 1.225 kg/m^3.

$$\dot{m} = \rho * Q \tag{6.1}$$

So, the air mass flux in the experiments was 0.000136 kg/s; still, it was rearranged due to the air pump not working with full efficiency, as 4.5370e-05 kg/s (one-third of the experiments) in Fluent, and it was for all models with 400 liters per hour air flow rate in the corresponding experiments.

Also, for the air, the dispersed phase, air diameter was set as 0.0012m based on the measurements related to the experiment.

The initial temperatures changing between 4˚C and 30.7˚C were established with the "patch" method for defined regions in Fluent, as shown in Table 6.2. For region-1,region3, region-5, region-7, region-9, and region-12, experimental results were available and set the model directly. There was a lack of information for the exact values for other regions: they were still established based on observations during experiments and the relation between the measuring point values. To better understand this method, the given charts would be helpful in Figure 6.1.

The model was run for 600 seconds without any update during simulation except for time step size.

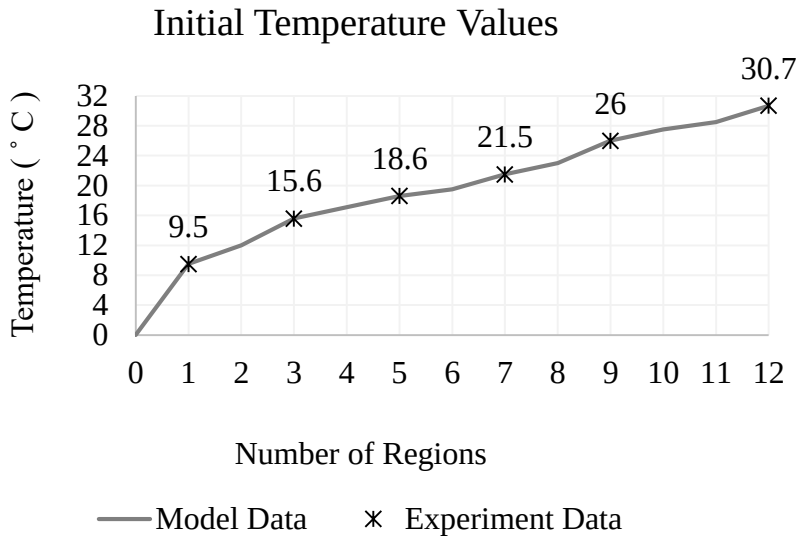

Figure 6.1. Initial temperature values in regions for 2D400F

After the simulation was completed, the temperature values were printed for six points and each second. For a full comparison, the location of these points was chosen as exactly the same at the points where the measurements were made in the experiments: 5cm, 15cm, 30cm, 50 cm, and 70cm.

Figure 6.2 shows the visualization of temperature distribution on the plane in line with the air diffuser (YZ plane and X=0.5meter) for the times of 0s, 150s,300s, and 600s. It represents the mixing process with colorful contours in the domain. The red contour lines represent the maximum temperature of 30˚C, whereas the blue ones belong to the minimum temperature of 4˚C. The temperature values expressed by the colors for contours are seen in the figure. While colored contours can be easily determined at different temperatures initially, the temperature change with the effect of the air diffuser over time is seen as a color change. It is the visualization of the mixing process of temperature stratified water column.

Table 6.2. Initial conditions for temperatures in regions for 2D400F

Regions	Dimension (m)	Experiment Data	Model Data
region-12	0.88 **0.85** 0.825	**30.7**	**30.7**
region-11	0.825 0.775		28.5
region-10	0.775 0.725		27.5
region-9	0.725 **0,7m** 0.675	**26**	**26**
region-8	0.675 0.525		23
region-7	0.525 **0.5** 0.475	**21.5**	**21.5**
region-6	0.475 0.325		19.5
region-5	0.325 **0.3** 0.275	**18.6**	**18.6**
region-4	0.275 0.175		17.1
region-3	0.175 **0.15** 0.125	**15.6**	**15.6**
region-2	0.125 0.075		12
region-1	0.075 **0.05** 0.025	**9.5**	**9.5**
region-0	0.025 0		4

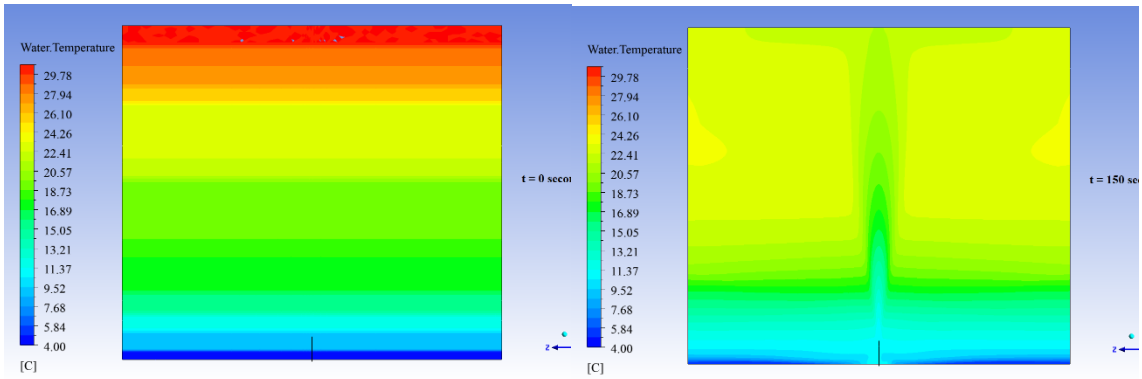

t = 0s

t = 150s

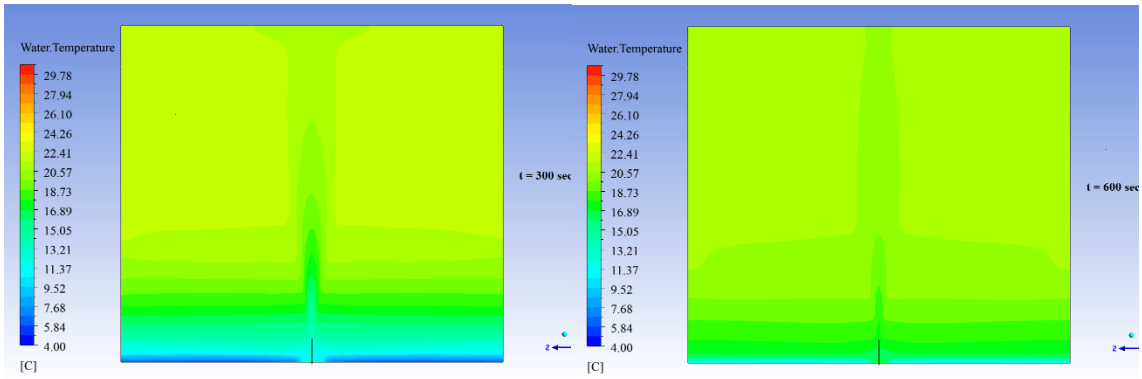

t = 300s

t = 600s

Figure 6.2. Temperature Distributions for t=0 , t=150s , t=300s, t=600s for 2D400F

Representations of air volume fraction, the velocity of air, and the velocity of water at 600 seconds are shown in Figure 6.3. It helps to understand the water velocity pattern generated by the air presence and behavior in the domain.

It is crucial to examine the data comparison as a time series to verify this kind of model. For this comparison, six points had selected, as mentioned earlier. In both experimental and numerical studies, the same points were selected to take the data obtained for each second over 10minutes.

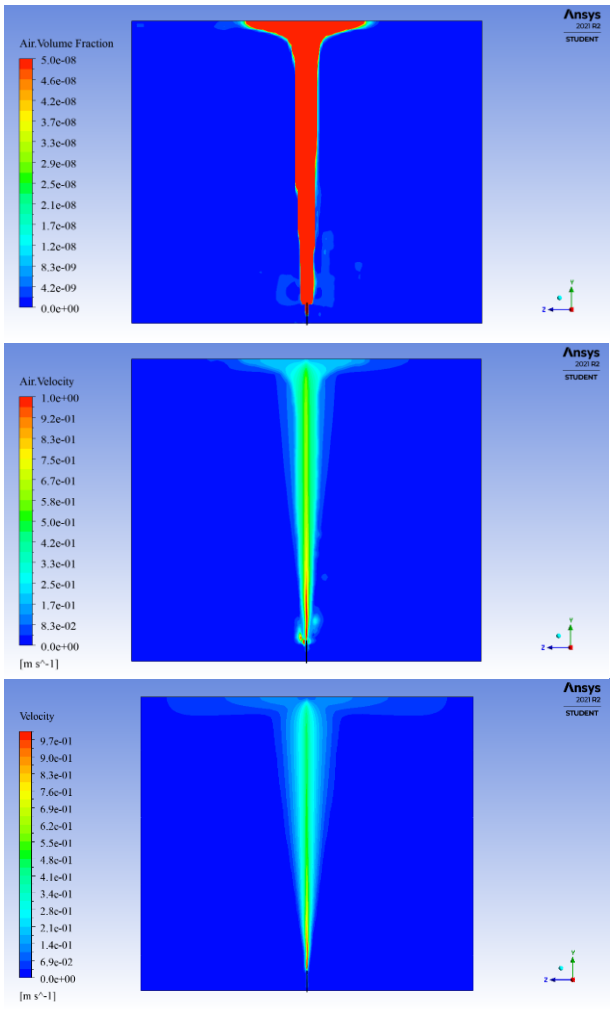

Figure 6.3. Representation of air volume fraction(a), the velocity of air(b), and the velocity of water(c) for t=600s for 2D400F

In addition to visual comparison on charts, The Root Mean Square Error (RMSE) and Mean Absolute Error (MAE) were calculated for temperatures to examine the difference between numerical and experimental results in more detail. The formulations of RMSE:

$$RMSE = \sqrt{\sum_{i=1}^{n} \frac{\left(T_{numerical} - T_{experimental}\right)^2}{n}} \tag{6.2}$$

and MAE:

$$MAE = \frac{1}{n}\sum_{i=1}^{n} \left| T_{numerical} - T_{experimental} \right| \tag{6.3}$$

were used for the calculations where the dataset includes 600 values for numerical and experimental data for every six points. The RMSE and MAE values for each measuring point are given in Table 6.3.

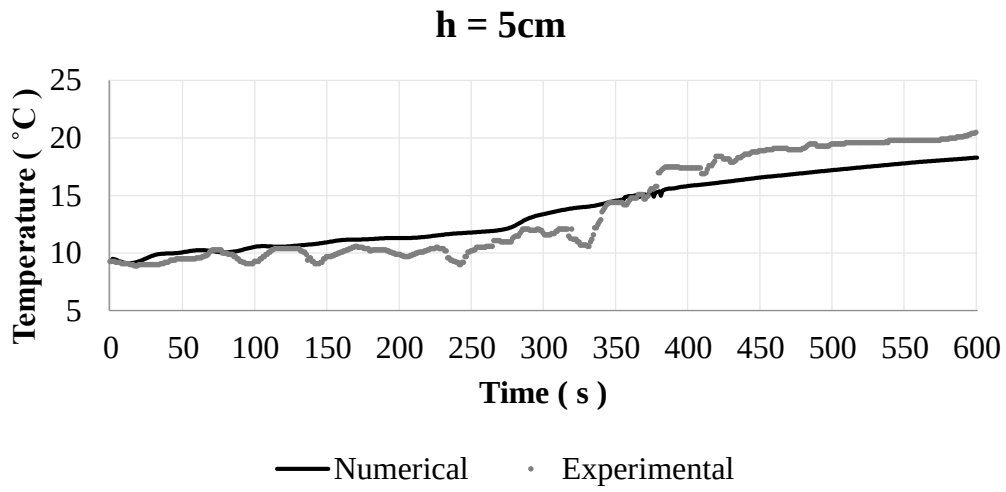

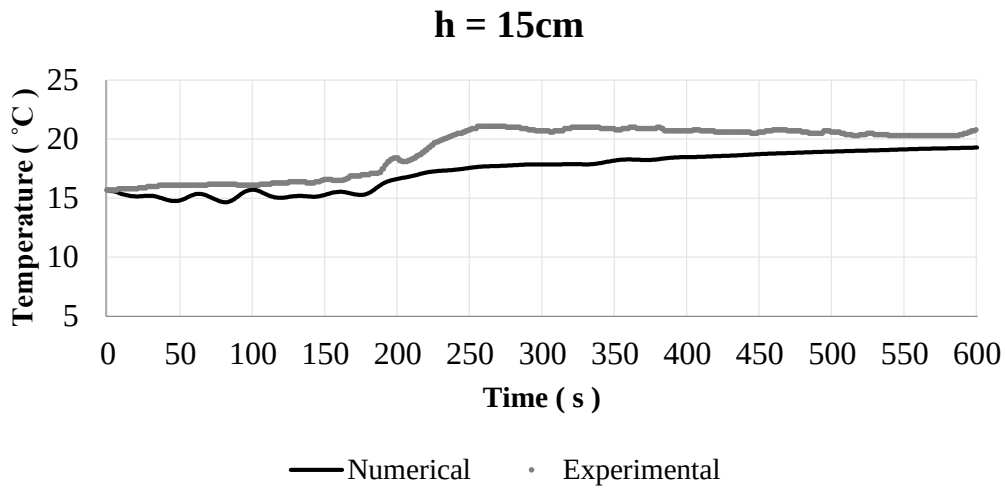

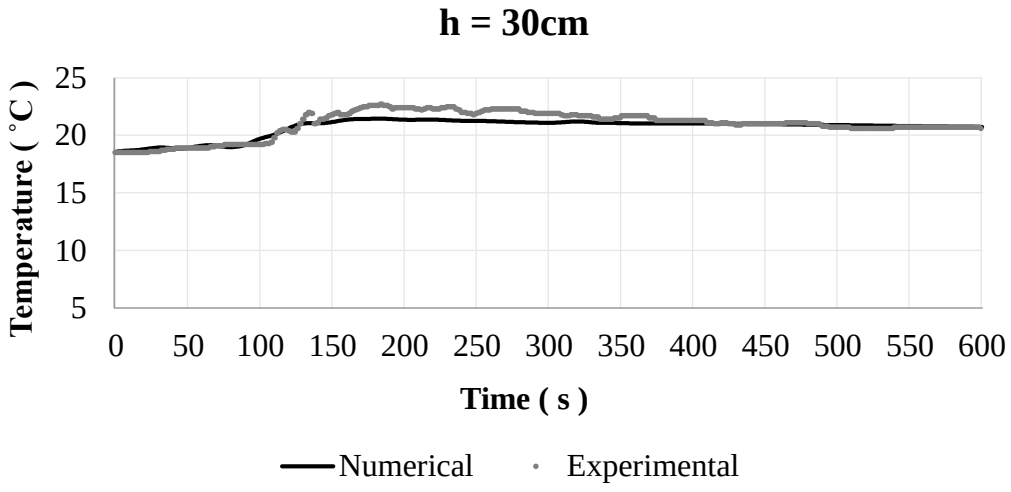

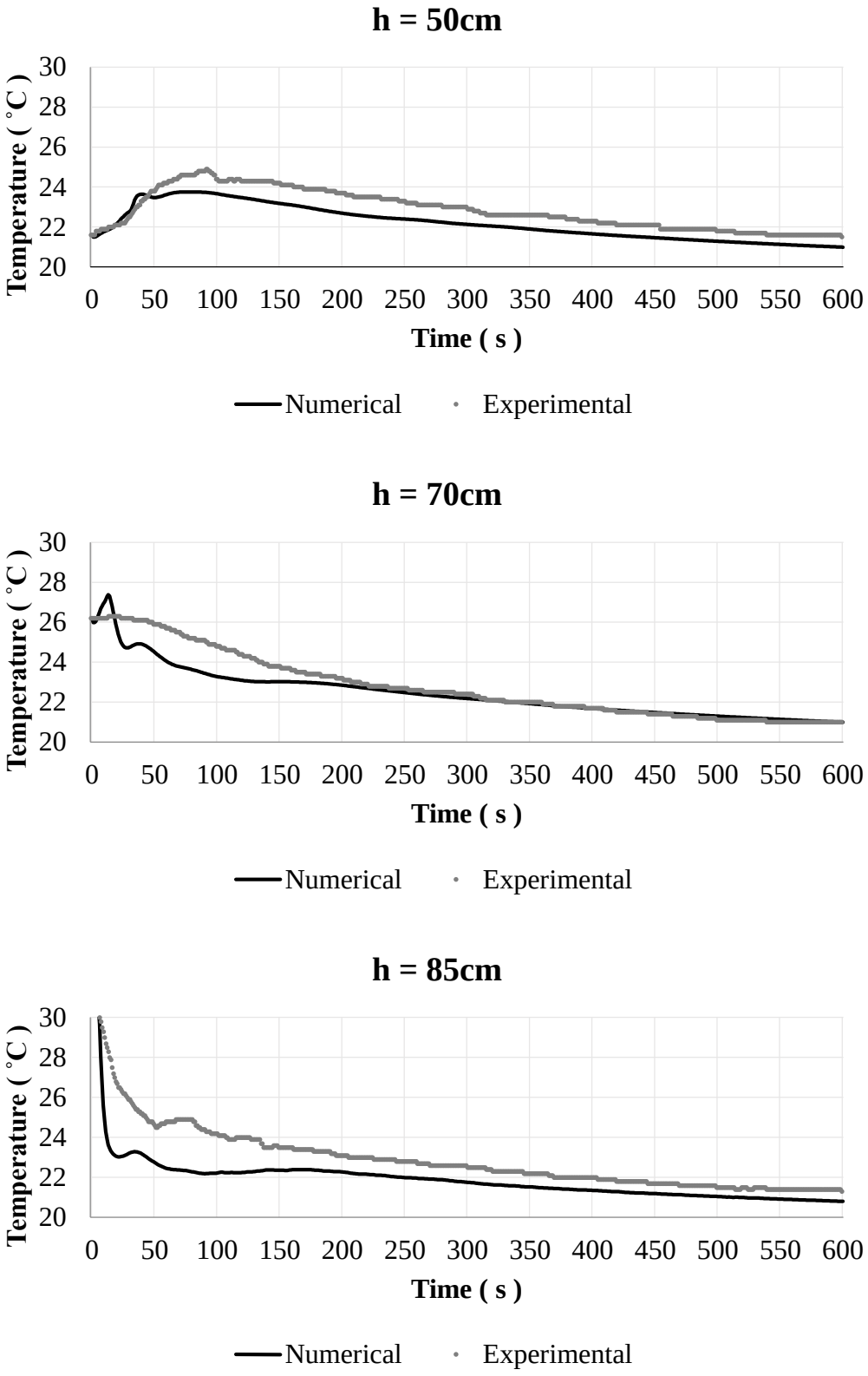

Figure 6.4. Comparison of numerical and experimental temperature results as time series for 2D400F

Table 6.3. RMSE and MAE values for 2D400F

Heights (cm)	Root Mean Square Error (RMSE)	Mean Absolute Error (MAE)
5	1.57	1.37
15	1.97	1.79
30	0.56	0.42
50	0.72	0.69
70	0.69	0.43
85	1.33	1.06

The RMSE values were calculated as 1.57˚C, 1.97 ˚C, 0.56 ˚C, 0.72 ˚C, 0.69 ˚C, and 1.33 ˚C orderly for the heights from bottom to top. To better comment on RMSE values, they were re-evaluated as percentages of the average temperatures at the experiments. As a result, it was found that are 8% for 5cm, 9% for 15cm, 4% for 85cm, and 3% for the 30 cm,50cm,70 cm.

The RMSE and MAE values show that the best accuracy is for 30cm, 50cm, and 70cm. It is also seen that the accuracy for the height of 5 cm and 15 cm is less than the others. Possible reasons for this may be the lack of information about the initial temperature values around these points or the position of the air diffuser in the experimental setup not being fully replicated in the model. A calibrated air mass flow can also be a cause.

In general, the RMSE and MAE values are acceptable for all heights, and the temperature changes of the numerical model and the experiment over 600 seconds are coherent according to the graphs.

6.2. Single Hole Air Diffuser having Diameter of 3mm and with 400 l/h Air Flow Rate, 3D400F

Another model was generated for the verification of the developed model base under different conditions. This time, the diameter of the air diffuser was assigned as 3mm, the air mass flow rate was set to the model as 4.5370e-05 kg/s (one-third of the experiments) again.

Table 6.4. Initial conditions for temperatures in regions for 3D400F

Regions	Dimension (m)	Experiment Data	Model Data
region-12	0.88 **0.85** 0.825	**32**	**32**
region-11	0.825 0.775		27.6
region-10	0.775 0.725		23.6
region-9	0.725 **0,7m** 0.675	**21.6**	**21.6**
region-8	0.675 0.525		21.3
region-7	0.525 **0.5** 0.475	**21**	**21**
region-6	0.475 0.325		20.1
region-5	0.325 **0.3** 0.275	**19.2**	**19.2**
region-4	0.275 0.175		17.5
region-3	0.175 **0.15** 0.125	**16.1**	**16.1**
region-2	0.125 0.075		12.5
region-1	0.075 **0.05** 0.025	**10**	**10**
region-0	0.025 0		7

Based on the measurements for the corresponding experiment, the air diameter was set as 1.5 mm for the dispersed phase in the Eulerian multiphase model. Initial conditions for temperatures were established in regions, as can be seen in Table 6.4. For region-1,region3, region-5, region-7, region-9, and region-12, experimental results were available and set the model directly. There was a lack of information for the exact values

for other regions: they were still established based on observations during experiments and the relation between the measuring point values.

The model was run for 600 seconds without any updating along the simulation except for time step size.

For temperature changing comparisons of numerical and experimental, results were taken for the six points described earlier. The display of the temperature distribution in the domain at different times can be seen in Figure 6.5. Red lines represent the maximum temperature of 32˚C, and the blue ones are for the minimum temperature of 7˚C, which was established to model as an initial condition in the domain. It is seen that there are no red contour lines that correspond to the maximum temperature and decrease the thickness of blue contour lines as time goes. When the final visualization is compared to the initial visualization, the destratification process is understood better.

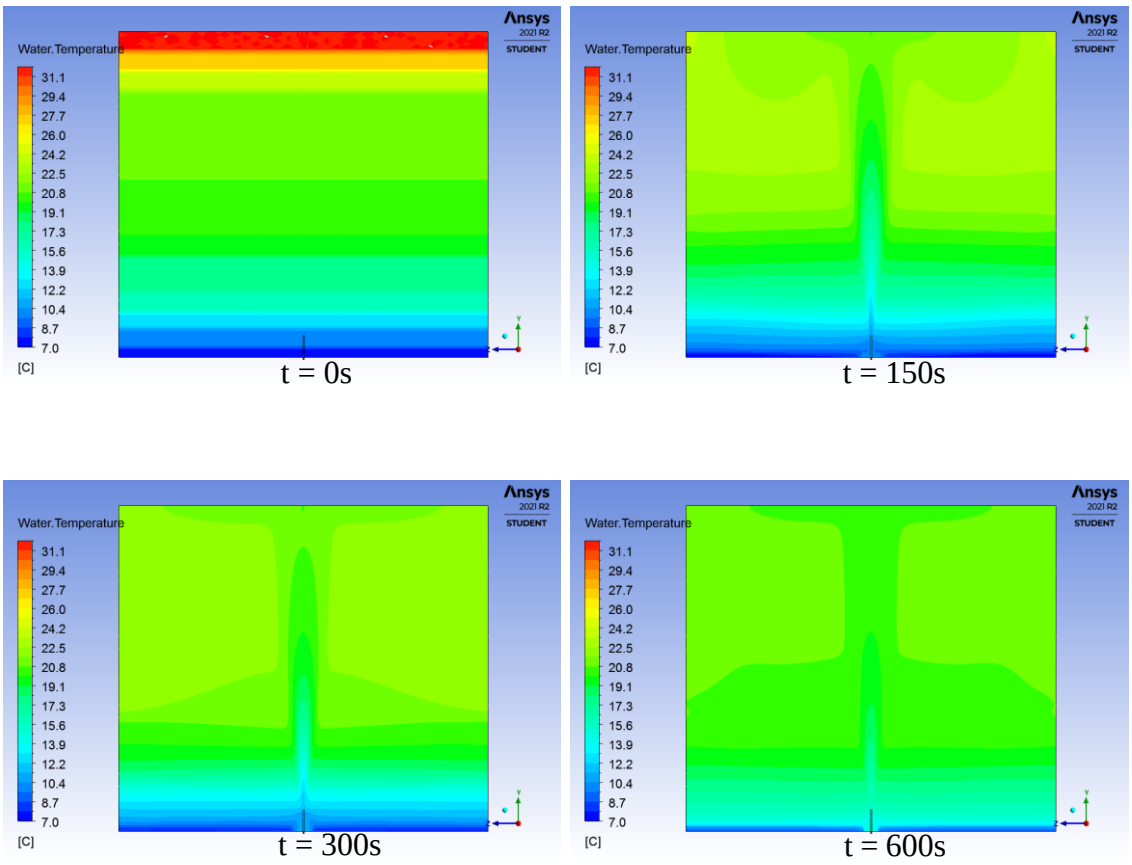

Figure 6.5. Temperature Distribution for t=0, t=150s, t=300s, t=600s for 3D400F

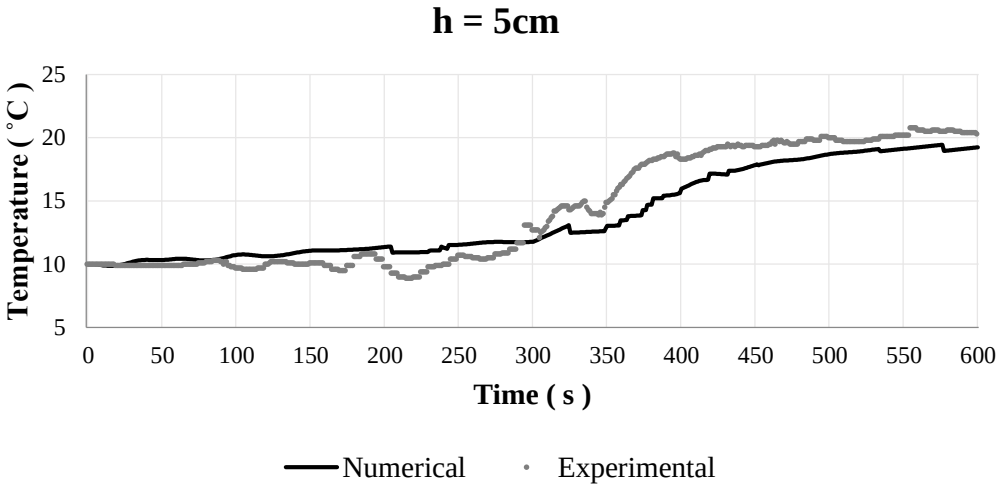
h = 5cm
Temperature (˚C)
25
20
15
10
5
0
50
100
150
200
250
300
350
400
450
500
550
600
Time (s)
Numerical
Experimental

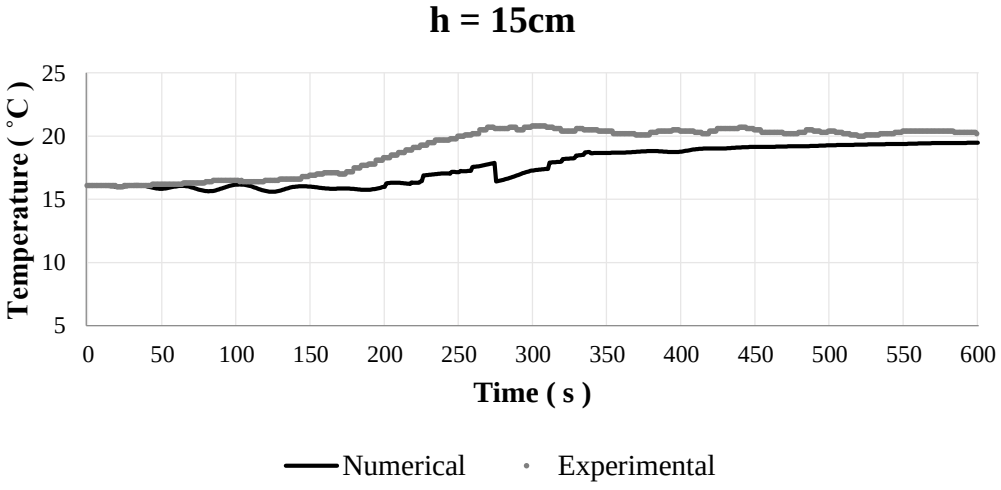
h = 15cm
Temperature (˚C)
25
20
15
10
5
0
50
100
150
200
250
300
350
400
450
500
550
600
Time (s)
Numerical
Experimental

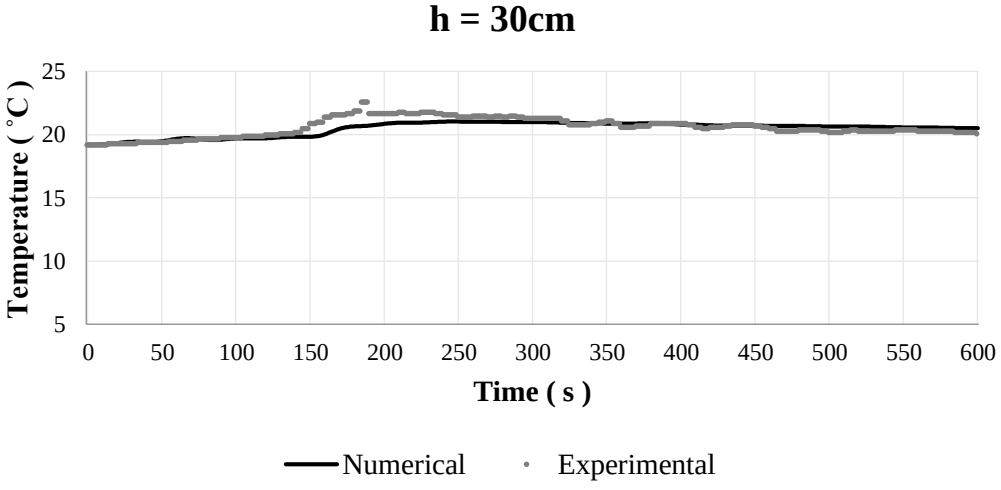
h = 30cm
Temperature (˚C)
25
20
15
10
5
0
50
100
150
200
250
300
350
400
450
500
550
600
Time (s)
Numerical
Experimental

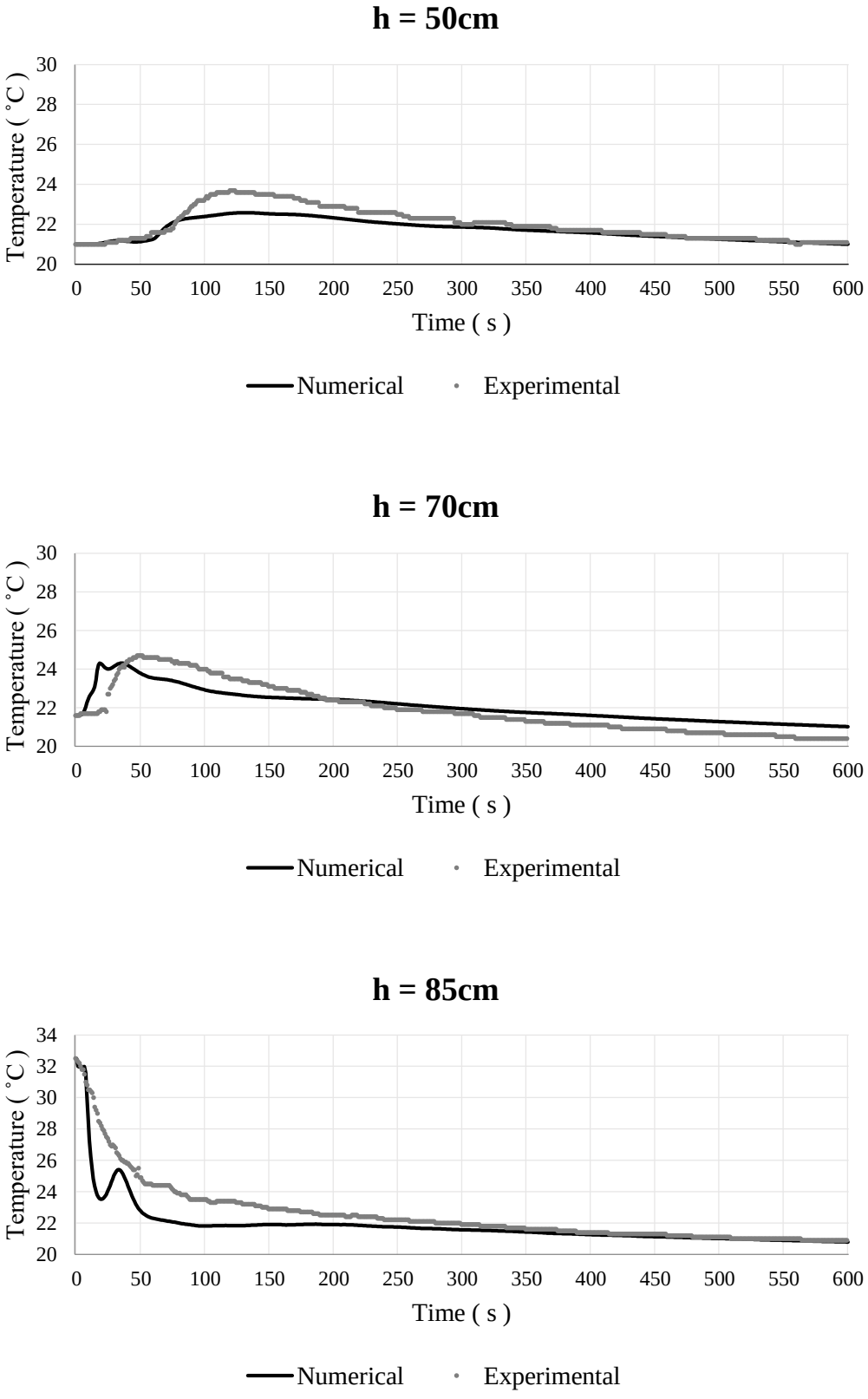

Figure 6.6. Comparison of numerical and experimental temperature results as time series for 3D400F

For comparison of numerical and experimental results as a time series, the charts were drawn time versus temperature for both experimental and numerical data for each second over 10 minutes, as shown in Figure 6.6.

According to the charts, the numerical best fit the experiment for 30cm,50 cm, and 85cm. The final temperatures in the model are almost the same at the experiment in a given time, and only some tiny different fluctuations occur between them; still, these are in the same behavior pattern. For other points, the final temperatures are so close that they are equal to or less than 1˚C. If the changing temperature pattern is examined, it is clear that the model is not perfect for 5cm and 15cm; at some time intervals, the difference between numerical and experimental results is around 3˚C - 4˚C. But generally, for all points, the numerical model is compatible with the experimental results.

Besides the comparison based on charts, the RMSE and MAE values were calculated for each measuring point and listed in Table 6.5.

Table 6.5 RMSE and MAE values for 3D400F

Height (cm)	Root Mean Square Error (RMSE)	Mean Absolute Error (MAE)
5	1.50	1.27
15	1.69	1.39
30	0.47	0.34
50	0.45	0.31
70	0.66	0.56
85	1.16	0.71

The RMSE values were calculated as 1.50˚C, 1.69 ˚C, 0.47 ˚C, 0.45 ˚C, 0.66 ˚C, and 1.16 ˚C orderly for the heights from bottom to top. To better comment on RMSE values, they were re-evaluated as percentages of the average temperatures in time-averaged at the experiments. Resultingly, they were found that be around %7 for 5cm and 15cm, 4% for 85 cm, and around 2% for 30cm, 50cm, and 70cm.

The RMSE and MAE values show that the best accuracy is for 30cm, 50cm, and 70cm. It is also seen that the accuracy for the height of 5 cm and 15 cm is less than the others. Possible reasons for this may be the lack of information about the initial temperature values around these points or the position of the air diffuser in the

experimental setup not being fully replicated in the model. A calibrated air mass flow can also be a cause.

In general, the RMSE and MAE values are acceptable for all heights, and the temperature changes of the numerical model and the experiment over 600 seconds are coherent according to the graphs.

6.3. Single Hole Air Diffuser Having Diameter of 4mm and with 400 l/h Air Flow Rate, 4D400F

For verification of the model, another experiment was carried out under the conditions of the air diffuser with a diameter of 4mm and air flow rate of 400 l/h. In the model, the diameter of the air diffuser was drawn as 4mm and the air flow rate as 4.54e-05 kg/s.

Based on the measurements for the corresponding experiment, the air diameter was set as 1.8 mm for the dispersed phase in the Eulerian multiphase model.

Initial conditions for temperatures changing from 5˚C to 31˚C were established in regions can be seen in Table 6.6. For region-1,region3, region-5, region-7, region-9, and region-12, experimental results were available and set the model directly. There was a lack of information for the exact values for other regions: they were still established based on observations during experiments and the relation between the measuring point values.

The model was run for 600 seconds without any updating along the simulation except for time step size.

After the simulation was completed, the destratification process in the water column with changing temperatures from 5˚C to 31˚C was examined, and the numerical results were compared to experimental ones. For comparison, the same method was applied in the comparisons of 2D400f and 3D400F.

The visual presentation of the destratification process in the model is given in Figure 6.7. The maximum and the minimum temperatures were 31˚C and 7˚C, and they

are represented by the colors of red and blue in the figure. The layered contour appearance, which expresses the temperature layers, has left its place to a single green color representing the temperature around 20˚C.

Table 6.6 Initial conditions for temperatures in regions for 4D400F

Regions	Dimension (m)	Experiment Data	Model Data
region-12	0.88 **0.85** 0.825	**31**	**31**
region-11	0.825 0.775		27.5
region-10	0.775 0.725		24.5
region-9	0.725 **0.7m** 0.675	**22.1**	**22.1**
region-8	0.675 0.525		20.8
region-7	0.525 **0.5** 0.475	**19.6**	**19.6**
region-6	0.475 0.325		18.3
region-5	0.325 **0.3** 0.275	**17.9**	**17.9**
region-4	0.275 0.175		17
region-3	0.175 **0.15** 0.125	**16.1**	**16.1**
region-2	0.125 0.075		12
region-1	0.075 **0.05** 0.025	**10.5**	**10.5**
region-0	0.025 0		5

Behind the visual representation, the temperature results in the model were examined in detail as time series to compare the results from the experiment. Both experimental and numerical temperature results were drawn as a graph in time series for the measuring points of 5cm, 15cm,50cm, 70 cm, and 85cm (Figure 6.8). For the measuring point of 30cm, numerical and experimental results have the perfect match, where both of them start at the temperature of 17.2˚C and complete the process at 19.5˚C in the same changing pattern. The same comment can be made for 70cm and 85 cm points, except for the changing patterns because the temperature difference is around 3˚C for some time intervals. Also, it can be said that the final temperature of the numerical model is less than the experimental ones for the 5cm and 15 cm, but it is not a big difference that can not be tolerated.

To compare the time series data overall, the RMSE and MAE values were calculated for each measuring point separately and given in Table 6.7.

The RMSE values were calculated as 1.79˚C, 1.84 ˚C, 0.40 ˚C, 0.73 ˚C, 0.61 ˚C, and 1.57 ˚C orderly for the heights from bottom to top. To better comment on RMSE values, they were re-evaluated as percentages of the average temperatures in time-averaged at the experiments. Resultingly, the RMSE values are changing around 2% and 3% for the middle points of 30cm,50cm, and 70cm. for 50 cm, it is 5%, and more than 5% for 5cm and 15cm.

The RMSE and MAE values show that the model best fits the experiment for 30cm, 50cm, and 70cm, where the worst is 15cm. In general, the RMSE and MAE values are acceptable for all measuring points, and the temperature changes of the numerical model and the experiment over 600 seconds are coherent according to the graphs.

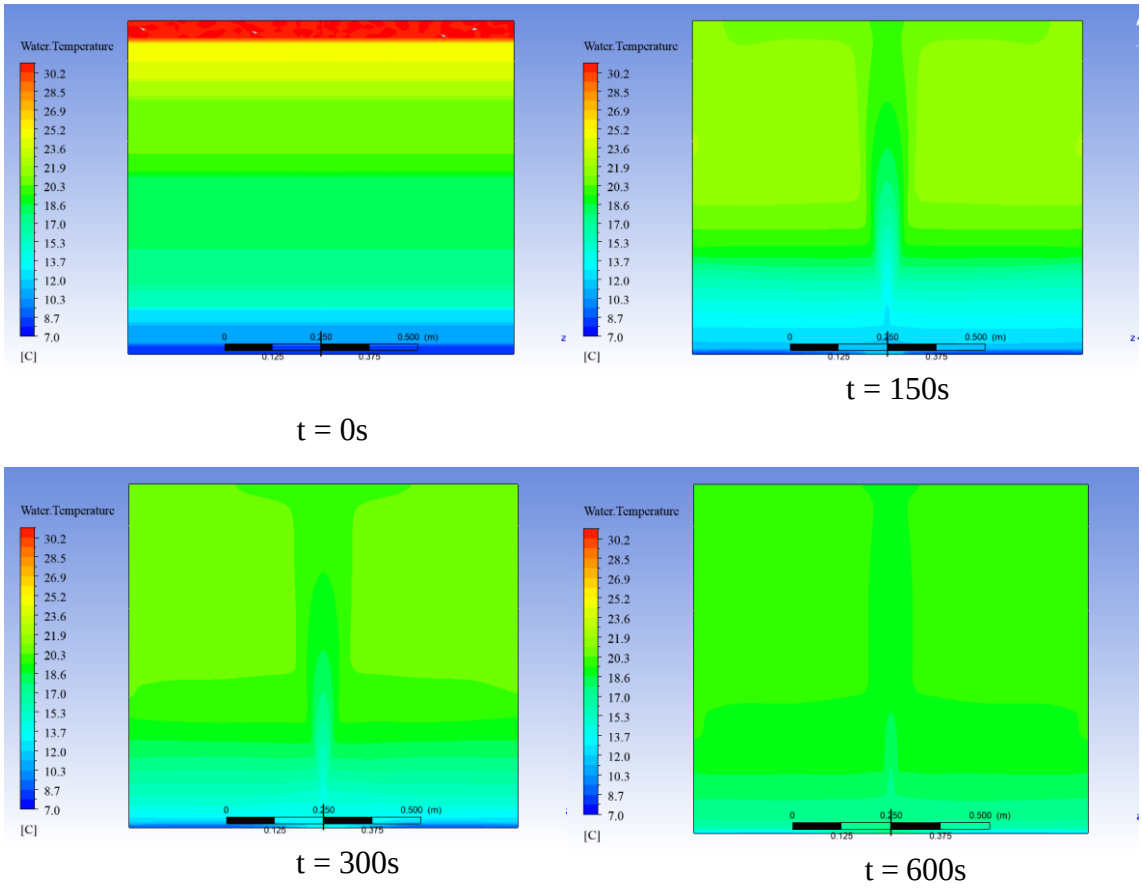

Figure 6.7 Temperature Distribution for t=0, t=150s, t=300s, t=600s for 4D400F

Table 6.7 RMSE and MAE values for 4D400F

Depths (m)	Root Mean Square Error (RMSE)	Mean Absolute Error (MAE)
0.05	1.79	1.61
0.15	1.84	1.78
0.3	0.40	0.32
0.5	0.73	0.68
0.7	0.61	0.38
0.85	1.57	1.13

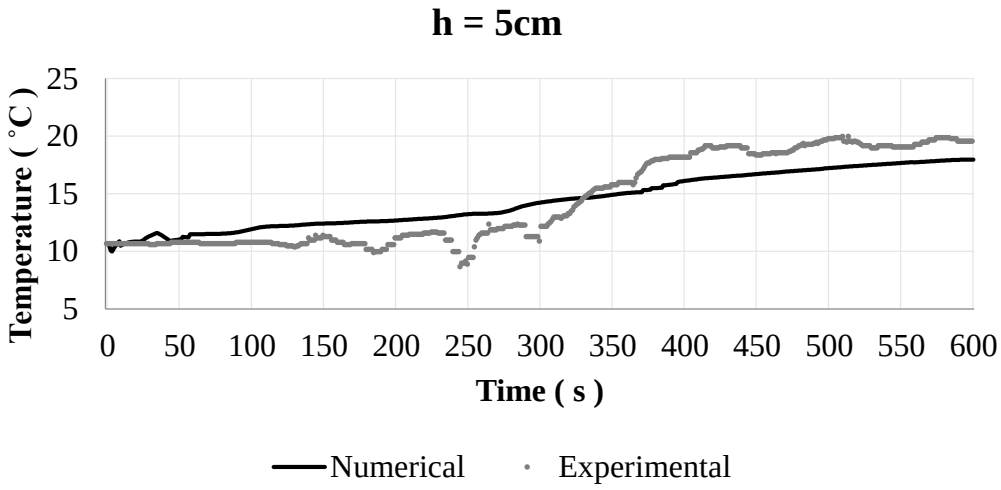
h = 5cm
Temperature (°C)
25
20
15
10
5
0
50
100
150
200
250
300
350
400
450
500
550
600
Time (s)
Numerical
Experimental

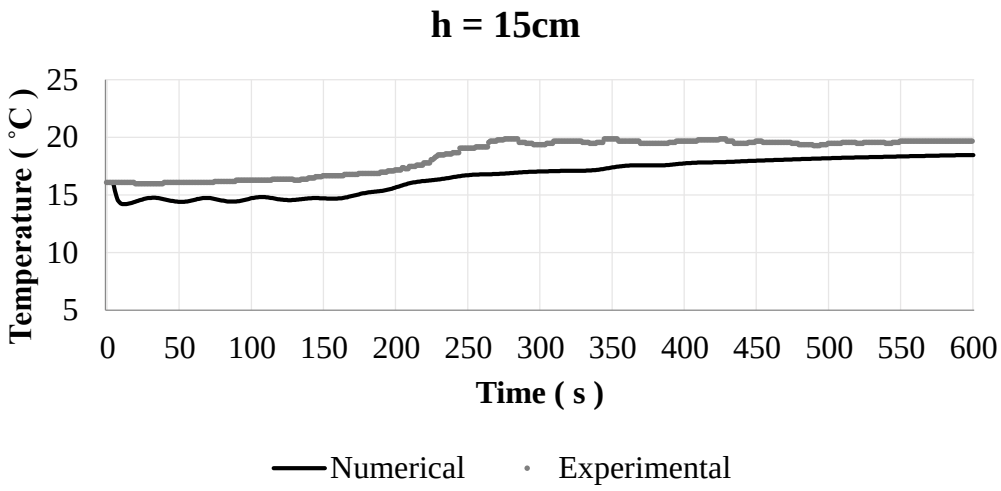
h = 15cm
Temperature (°C)
25
20
15
10
5
0
50
100
150
200
250
300
350
400
450
500
550
600
Time (s)
Numerical
Experimental

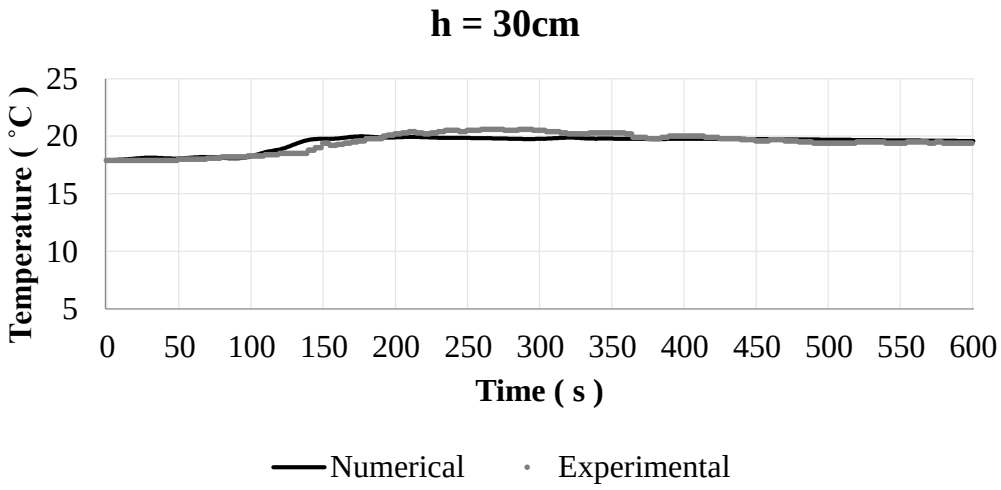
h = 30cm
Temperature (°C)
25
20
15
10
5
0
50
100
150
200
250
300
350
400
450
500
550
600
Time (s)
Numerical
Experimental

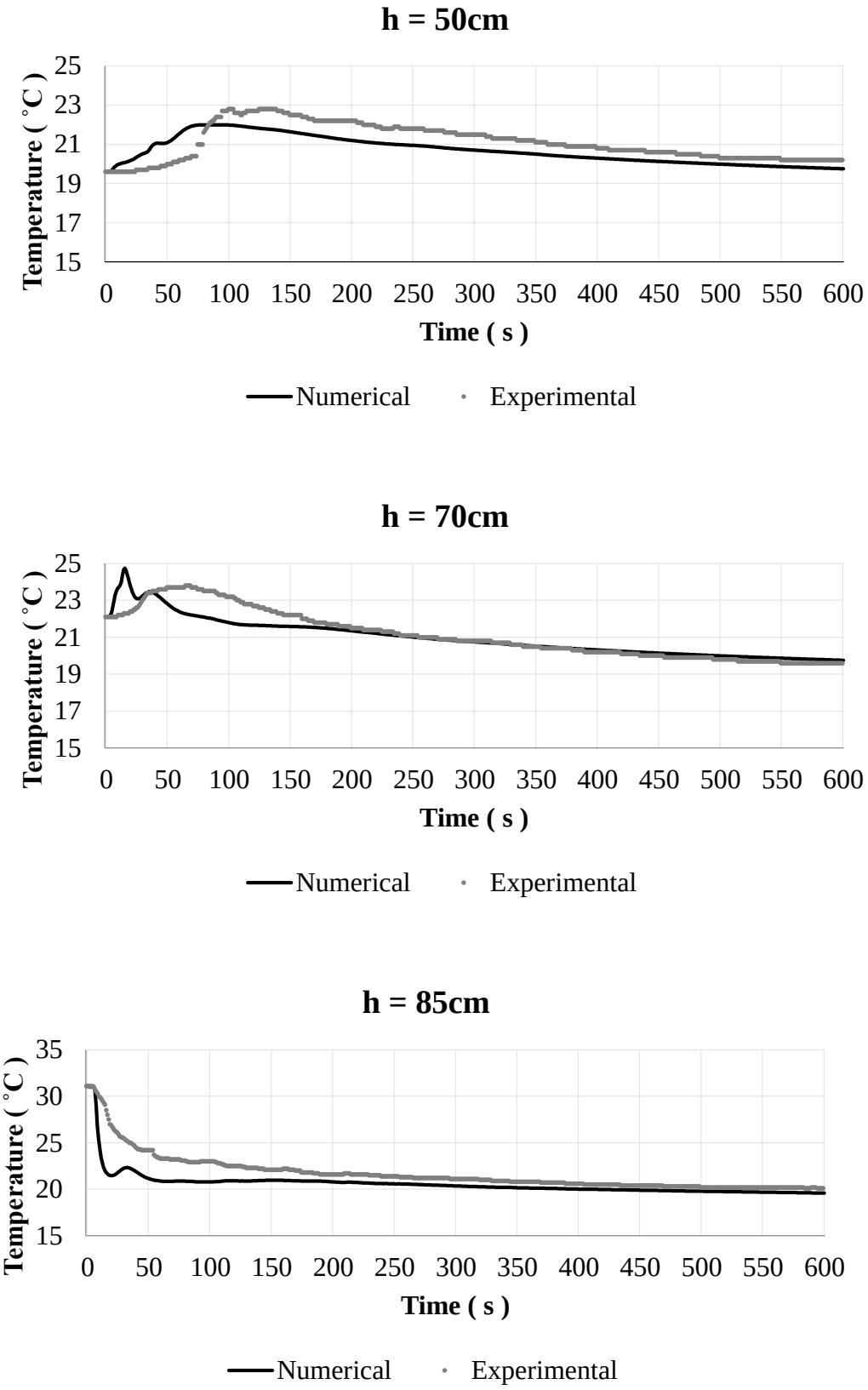

Figure 6.8. Comparison of numerical and experimental temperature results as time series for 4D400F

6.4. Single hole Air Diffuser Having Diameter of 2mm and with 200 l/h Air Flow Rate, 2D200F

So far, all numerical models were compared with the experiments for different diameters of air diffusers, but the same air flow rate of 400l/h was used. In this section, model verification is tested with another air flow rate of 200 l/hour with a diameter of 2mm. It is essential to run the model base under different conditions to obtain and determine the calibration parameters.

Some arrangements were made for the boundary condition of the air mass flow inlet. For the corresponding experiment, the air flow rate was 200l/h, as mentioned above. To integrate the term of mass flow inlet, the transition between the volume flux and mass flux in equation (6.1) was applied with the same assumption of air density equals 1.225kg/m^3. As a result, air mass flux was found as 6.81e-05 kg/s for the experiment. As with other models, air mass flux was entered into the model as one-third of that in the experiment since the air pump did not operate at full efficiency, which means that the air mass flow rate was set as 2.30e-05 kg/s in this model.

Based on the measurements for the corresponding experiment, the air diameter was set as 1.2 mm for the dispersed phase in the Eulerian multiphase model.

Initial conditions for temperatures changing from 0˚C to 30˚C were established in regions can be seen in Table 6.8. For region-1,region3, region-5, region-7, region-9, and region-12, experimental results were available and set the model directly. There was a lack of information for the exact values for other regions: they were still established based on observations during experiments and the relation between the measuring point values.

As a reminder, other models had been run for 600 seconds, but this was simulated more extensively time scale due to the lower air flow rate. Based on the observation of experiments, a lower air flow rate indicates a slower destratification process, so this model was run for 800 seconds without any updating during simulation except for the time step size.

After the simulation was completed, the destratification process in the water column with changing temperatures from 0˚C to 30˚C was examined, and the numerical

results were compared to experimental ones. For comparison, the same method was applied in the other comparisons, but data were evaluated for this model for 800 seconds, not 600 seconds.

The visual presentation of the destratification process in the model is given in Figure 6.9 at the starting, 250 seconds,500 seconds, and 800seconds. The maximum and the minimum temperatures were 30˚C and 0˚C, and they are represented by the colors of red and blue in the figure. Decreasing the number of layered contour appearances indicates the destratification process. When the display of the temperature contours is examined at 800seconds, it is clear that the destratification is not completed for the bottom section on the fluid domain.

To better understand the destratification process, experimental and numerical temperature data for a time series of 800 seconds was represented in graphs for the same six measuring points; 5cm, 15cm, 30cm, 50cm, 70cm, and 85cm (Figure 6.10).

Except for the 5cm and 15cm, the numerical model perfectly matches the corresponding experiment. For these measuring points, changing temperature patterns and final temperatures are well compatible, apart from the delay of the numerical model to experiment about 30 seconds at the beginning of the simulation for 50cm and 70cm and temperature fluctuations at 85cm. The exact temperature changes in time can be seen, but there is a difference of about 1˚C during the simulation for 15cm. Also, for 5cm, there is a significant difference in comparison, although they are at almost the same temperature at 800 seconds, which is the stability. While the temperature increase is more stable in the numerical model, this increase occurs with visible fluctuations in the experiment.

Table 6.8 Initial conditions for temperatures in regions for 2D200F

Regions	Dimension (m)	Experiment Data	Model Data
region-12	0.88 **0.85** 0.825	**29.5**	**30**
region-11	0.825 0.775		26.8
region-10	0.775 0.725		23.8
region-9	0.725 **0.7m** 0.675	**21.8**	**21.8**
region-8	0.675 0.525		21.9
region-7	0.525 **0.5** 0.475	**22**	**22**
region-6	0.475 0.325		20.9
region-5	0.325 **0.3** 0.275	**20.1**	**20.1**
region-4	0.275 0.175		19.2
region-3	0.175 **0.15** 0.125	**18.4**	**18.4**
region-2	0.125 0.075		14.2
region-1	0.075 **0.05** 0.025	**10**	**10**
region-0	0.025 0		0

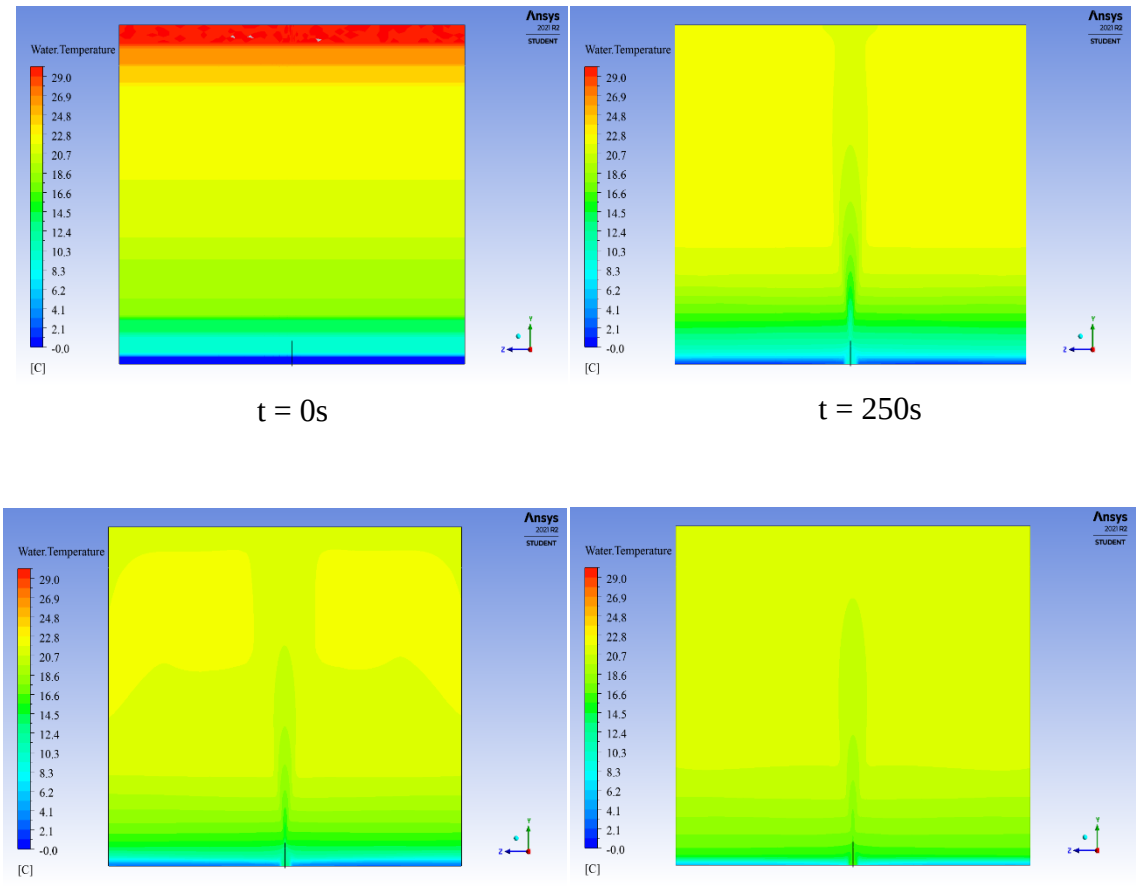

Figure 6.9 Temperature Distribution for t=0, t=250s, t=500s, t=800s for 2D200F

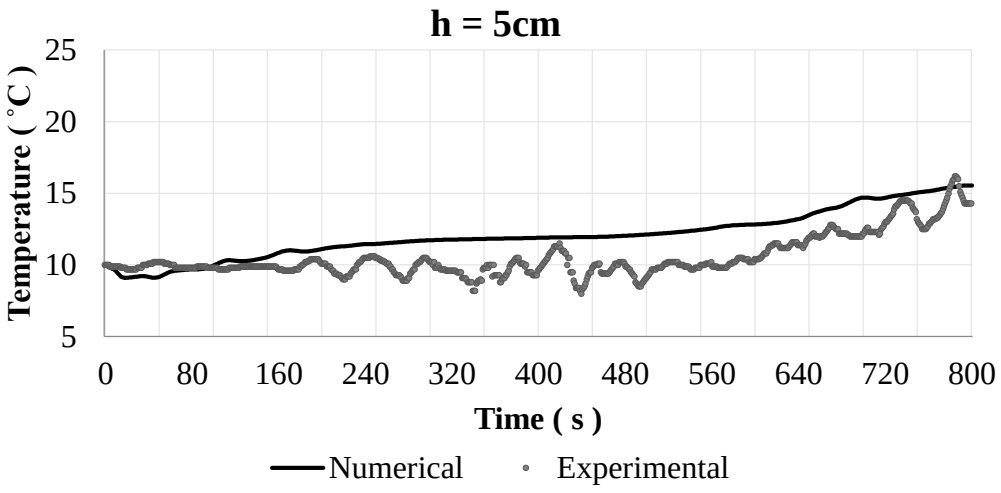

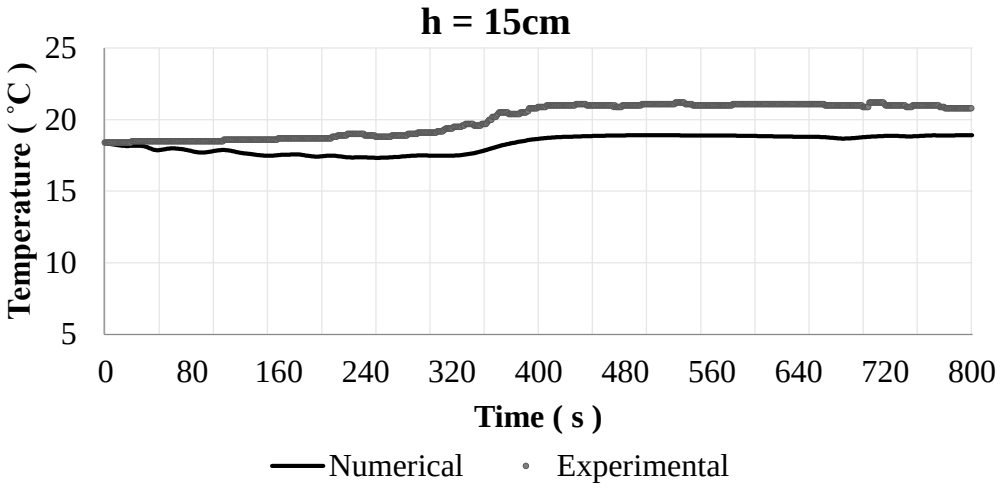
h = 15cm
Temperature (˚C)
25
20
15
10
5
0
80
160
240
320
400
480
560
640
720
800
Time (s)
Numerical
Experimental

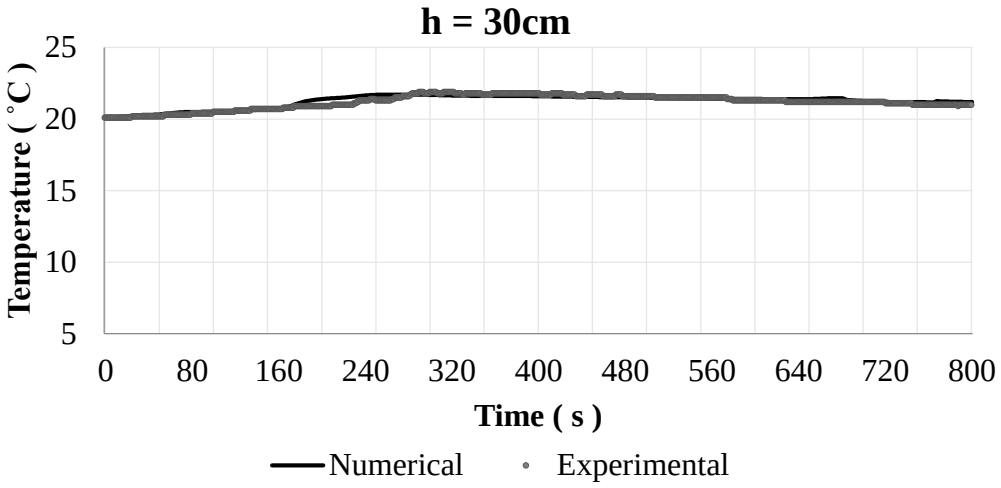
h = 30cm
Temperature (˚C)
25
20
15
10
5
0
80
160
240
320
400
480
560
640
720
800
Time (s)
Numerical
Experimental

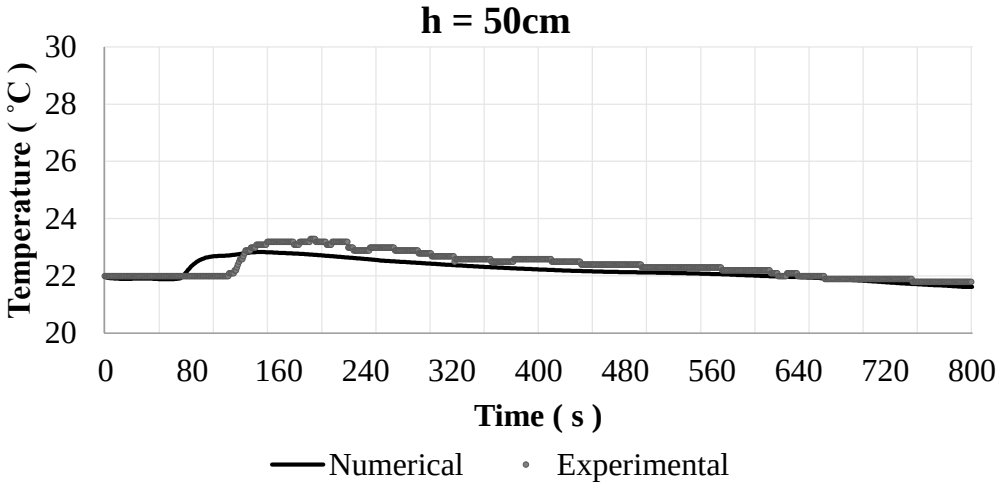
h = 50cm
Temperature (˚C)
30
28
26
24
22
20
0
80
160
240
320
400
480
560
640
720
800
Time (s)
Numerical
Experimental

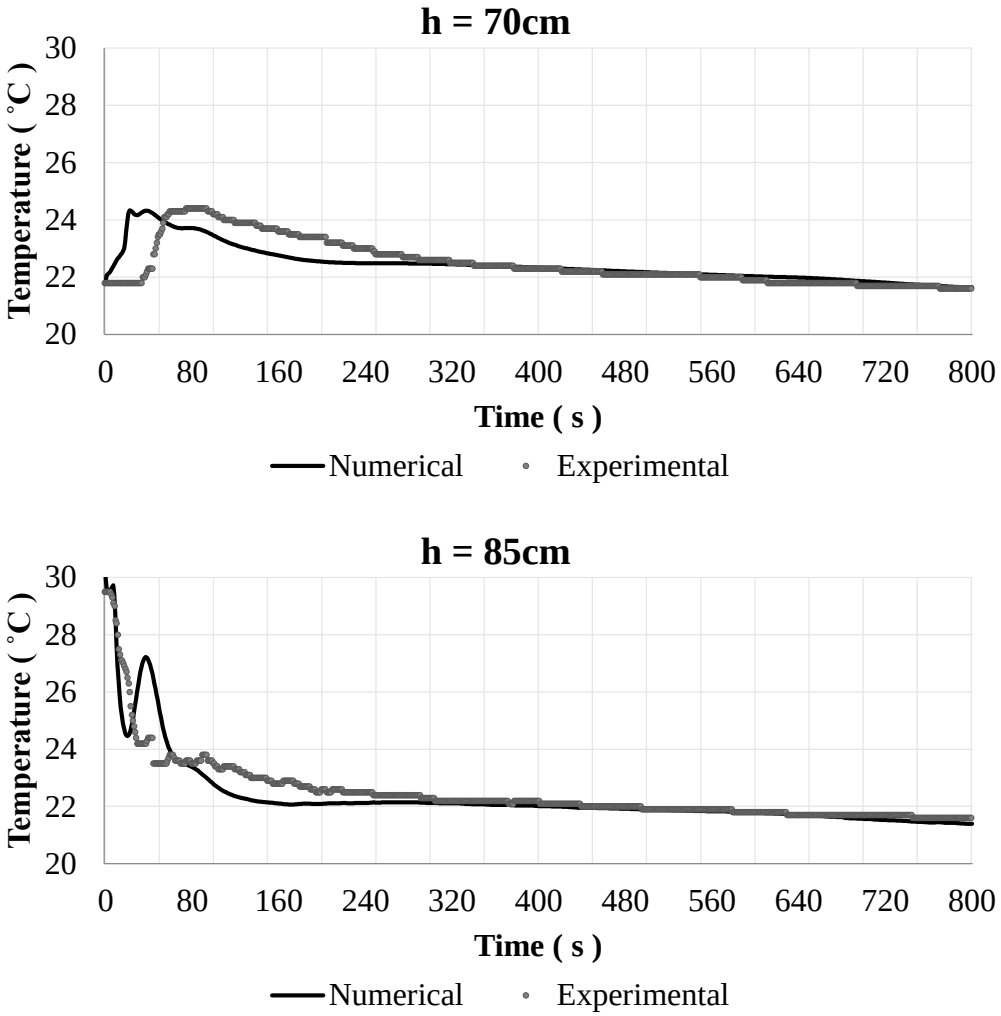

Figure 6.10. Comparison of numerical and experimental temperature results as time series for 2D200F

RMSE and MAE values were calculated for each measuring point separately and given in Table 6.9.

Table 6.9. RMSE and MAE values for 2D200F

Depths (m)	Root Mean Square Error (RMSE)	Mean Absolute Error (MAE)
0.05	1.86	1.64
0.15	1.83	1.71
0.3	0.19	0.15
0.5	0.30	0.25
0.7	0.59	0.35
0.85	0.60	0.33

The RMSE values were calculated as 1.86˚C, 1.83 ˚C, 0.19 ˚C, 0.30 ˚C, 0.59 ˚C, and 0.6 ˚C orderly for the heights from bottom to top. To better comment on RMSE values, they were re-evaluated as percentages of the average temperatures in time-averaged at the experiments. As a result, while they change from 0.88% to 2.4% for the upper layers, which are 30cm,50cm,70cm, and 85 cm, on the contrary of these low values, 16% for 5cm is the most significant ratio and 8.6% for 15cm.

The RMSE and MAE values show that the model best fits the experiment for 30cm, 50cm, 70cm, and 85cm, where the worst is 15cm. In general, the RMSE and MAE values are acceptable for all measuring points, and the temperature changes of the numerical model and the experiment over 800 seconds are coherent, according to the graphs.

6.5. Comparisons with Multiple Hole Air Diffusers

Until this part, comparisons between numerical model and observations had been made with a single hole air diffuser. A multiple hole air diffuser (see Figure 3.2) was performed in this section to verify the numerical model under different conditions.

6.5.1. Five Holes Air Diffuser Having Diameter of 2mm and with 400 l/h Air Flow Rate, 2D400F5

For numerical model verification with multiple hole air diffusers, the experiment has five holes air diffuser with a diameter of 2 mm and 400 l/h air flow rate. Initial conditions for temperatures changing from 7˚C to 30˚C were established in regions can be seen in Table 6.10. For region-1,region3, region-5, region-7, region-9, and region-12, experimental results were available and set the model directly. There was a lack of information for the exact values for other regions: they were still established based on observations during experiments and the relation between the measuring point values. The model was run for 600 seconds without any updating along the simulation except for time step size.

Table 6.10 Initial conditions for temperature in regions for 2D400F5

Regions	Dimension (m)	Experiment Data	Model Data
region-12	0.88 **0.85** 0.825	**29.8**	**29.8**
region-11	0.825 0.775		26.5
region-10	0.775 0.725		24.5
region-9	0.725 **0,7m** 0.675	**23.1**	**23.1**
region-8	0.675 0.525		21.5
region-7	0.525 **0.5** 0.475	**19.8**	**19.8**
region-6	0.475 0.325		19
region-5	0.325 **0.3** 0.275	**18.2**	**18.2**
region-4	0.275 0.175		17.5
region-3	0.175 **0.15** 0.125	**16.8**	**16.8**
region-2	0.125 0.075		13
region-1	0.075 **0.05** 0.025	**9.8**	**9.8**
region-0	0.025 0		7

The temperature results in the model were examined in detail as time series to compare the results from the experiment. Both experimental and numerical temperature results were drawn as a graph in time series for the measuring points of 5cm, 15cm,50cm,

70 cm, and 85cm (Figure 6.11). For measuring points of 30cm,50cm, and 70cm, the same pattern could be seen in temperature changing but with some minor time inconsistencies. Except for 5cm, there was a perfect match in final temperatures in the same specific time interval of 600 seconds in all other heights.

Besides that, the comparison as time series, also RMSE and MAE values were calculated in Table 6.11. The RMSE values were calculated as 2.01℃, 1.09℃, 0.53℃, 0.67℃, 0.73℃, and 1.52℃ orderly from 5cm to 85cm. The best fit was observed at 30cm with the 0.53℃ error corresponding to the %2.5 of the average temperature observed during the experiment. In general, the RMSE and MAE values are acceptable for all measuring points, and the temperature changes of the numerical model and the experiment over 600 seconds are coherent according to the graphs. Based on the results, it is clear that the numerical model is also suitable for the simulations of the multiple hole air diffusers.

Table 6.11 RMSE and MAE values for 2D400F5

Depths (cm)	Root Mean Square Error (RMSE)	Mean Absolute Error (MAE)
5	2.01	1.74
15	1.09	0.94
30	0.53	0.39
50	0.67	0.55
70	0.73	0.45
85	1.52	1.01

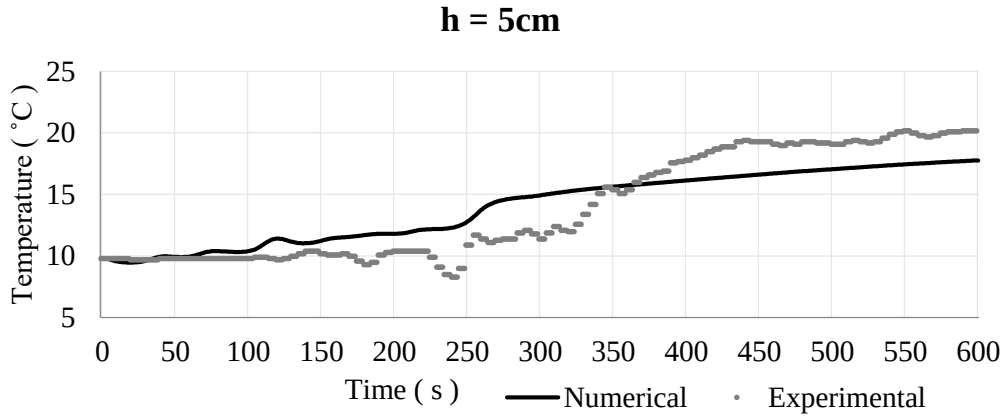

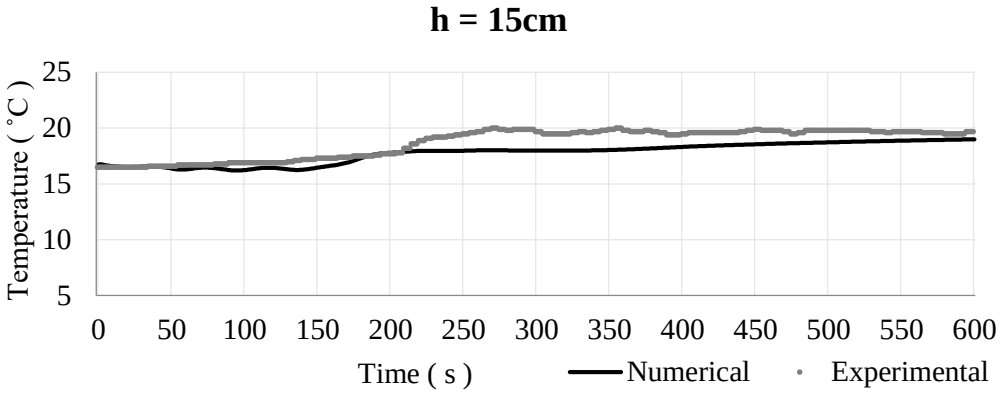
h = 15cm
Temperature (˚C)
25
20
15
10
5
0 50 100 150 200 250 300 350 400 450 500 550 600
Time (s)
Numerical
Experimental

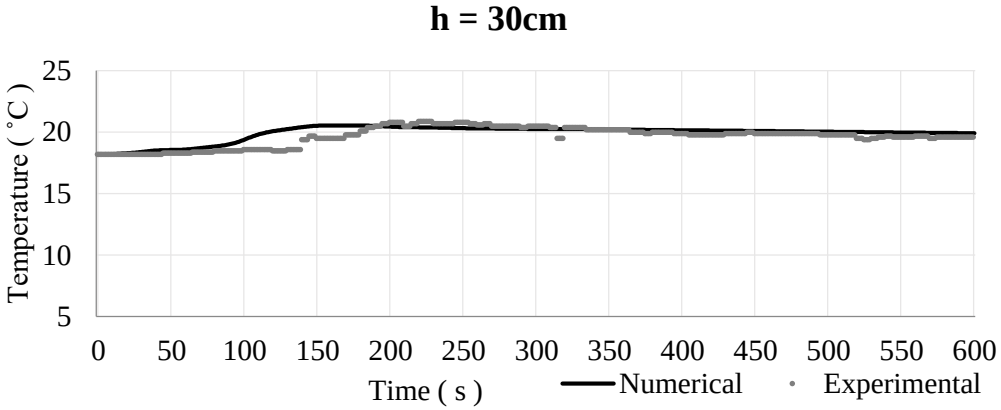
h = 30cm
Temperature (˚C)
25
20
15
10
5
0 50 100 150 200 250 300 350 400 450 500 550 600
Time (s)
Numerical
Experimental

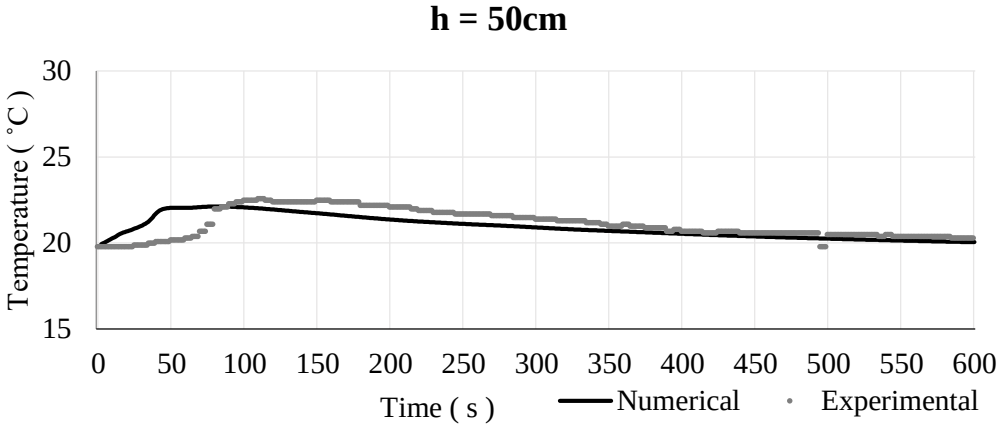
h = 50cm
Temperature (˚C)
30
25
20
15
0 50 100 150 200 250 300 350 400 450 500 550 600
Time (s)
Numerical
Experimental

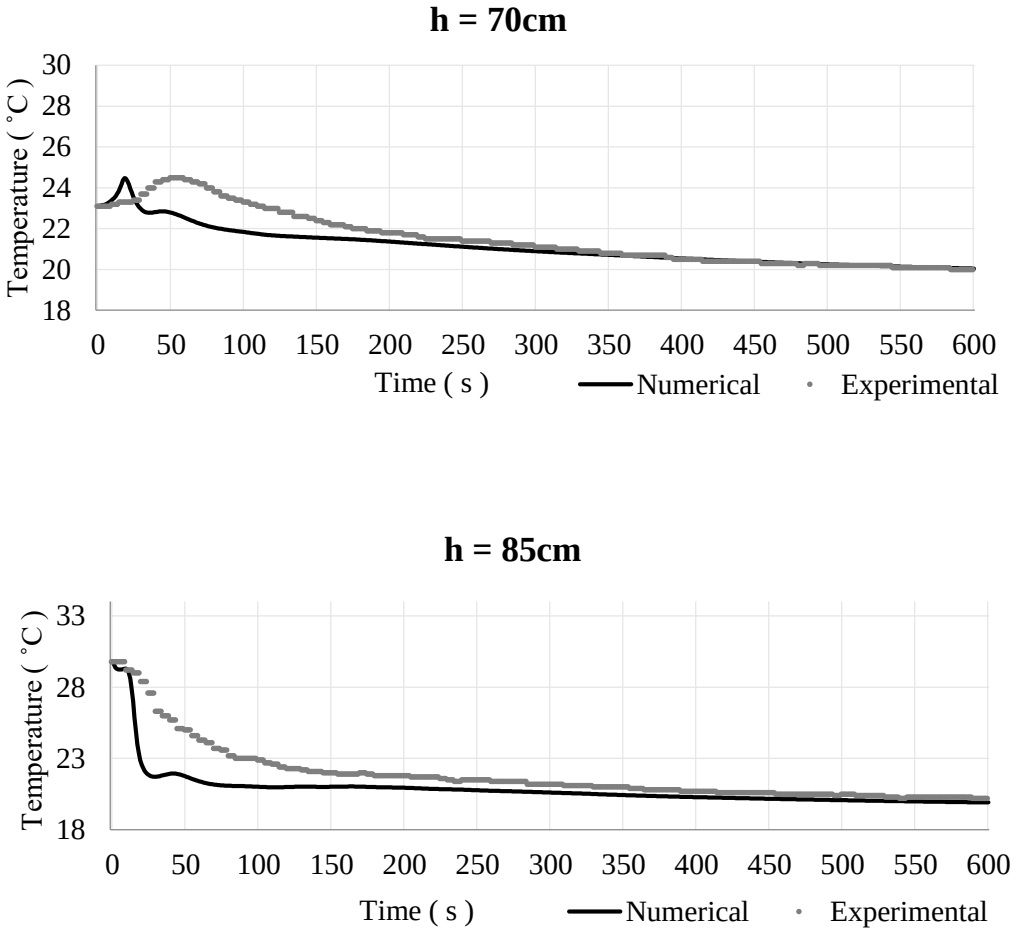

Figure 6.11 Comparison of numerical and experimental temperature results as time series for 2D400F5

6.5.2. Twelve Hole Air Diffuser Having Diameter of 2mm and with 400 l/h Air Flow Rate, 2D400F5

As a reminder, in section 3.1.1, the number of hole effects on the mixing process had been investigated experimentally. No considerable impact had been observed in mixing time in Figure 3.6 and destratification efficiency in Table 3.4. In this section, the effect of the number of holes of the air diffuser was examined numerically. Another model was run under the same conditions as the previous part (6.5.1) for this observation. The same initial temperatures (Table 6.10) and air flow rate were assigned to the regions for the numerical model with the twelve hole air diffuser.

The results were presented as time series in Figure 6.12, comparing the air diffuser with the 5 holes and 12 holes. When the graphs are examined, it can be seen that there was no difference between the results of 5 holes and 12 holes in all measuring points. The final temperatures were the same in all measuring points. Also, the temperature changing patterns were almost identical except for a minor difference at 5cm. As a result, the effect of the number of holes on the destratification process was examined numerically and experimentally. It is concluded that the hole number was not an effective parameter for mixing the thermally stratified water columns.

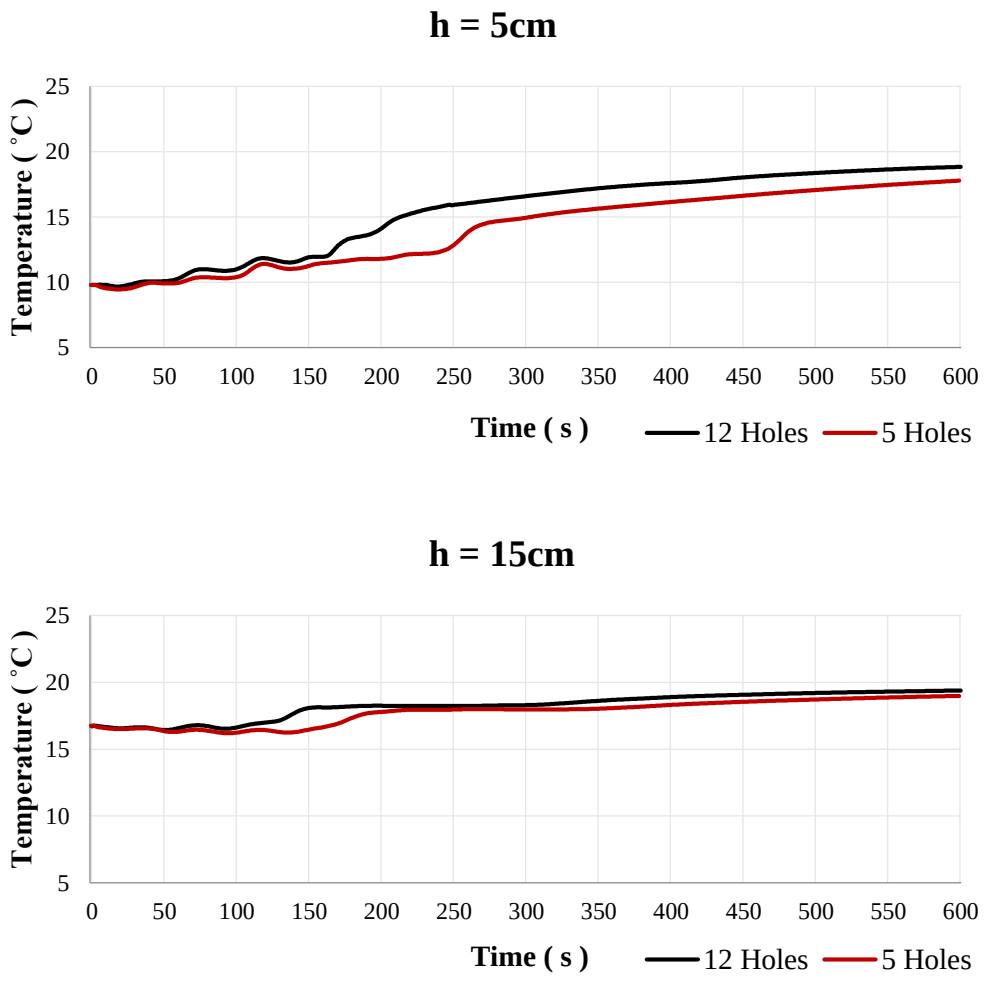

h = 30cm

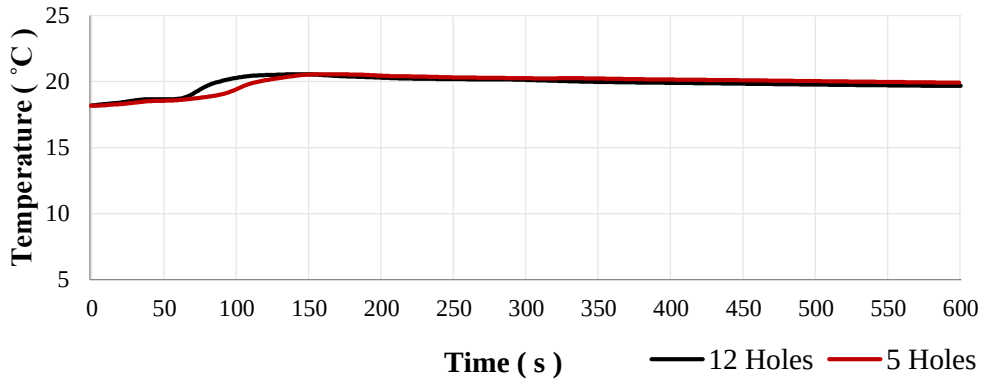

h = 50cm

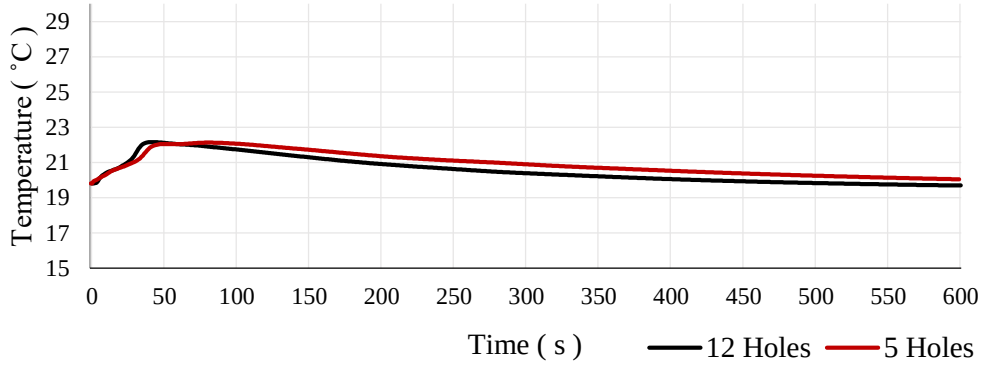

h = 70cm

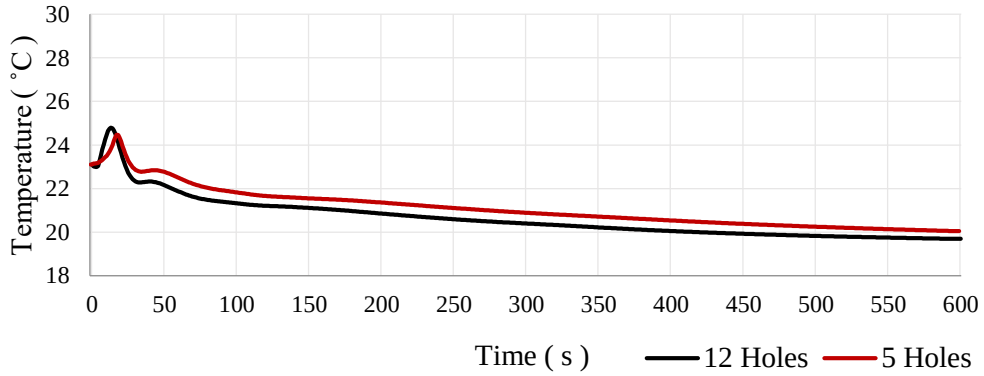

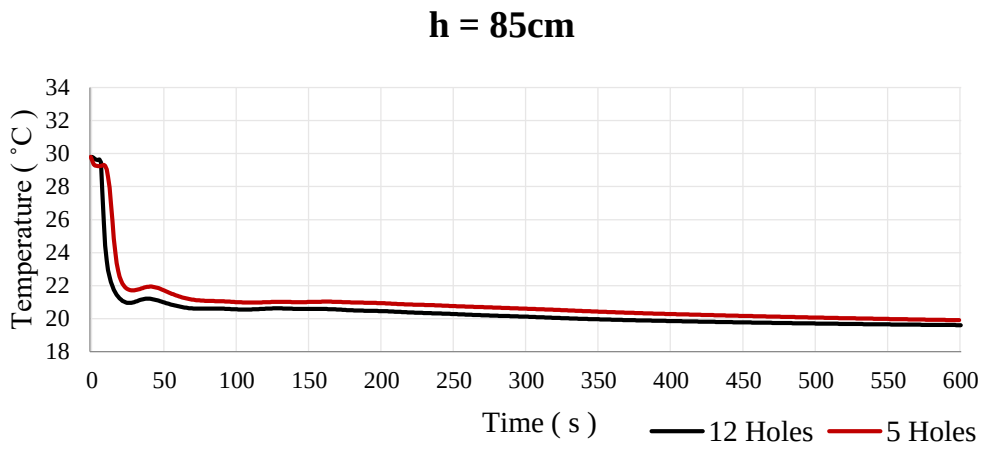

Figure 6.12 Comparison of the air diffusers with multiple holes of 5 and 12

6.6. Summary of Model Verification

The model base explained in Chapter 5 was re-set for four conditions to compare results with corresponding experiments; changes were done only for air diffuser diameter, air flow rate, and bubble diameter to see the accuracy of the model base and application limits. The conditions were selected according to the air flow rate and diameter of the air diffuser. For the same air flow rate, 400l/h, three different air diffusers with diameters of 2mm,3mm, and 4mm were generated; for the same diameter of air diffuser, two different air flow rates were used as 200l/h and 400l/h.

To evaluate the model accuracy in general, the pre-calculated RMSE values were summed for each measurement point and given in Table 6.12.

For a general evaluation of the RMSE value, it can be said that the smaller value represents the better accuracy of the model.

According to RMSE values, the model base has the best performance for the condition of air diffuser with 3mm and air flow rate of 400l/h; because of that, the smallest RMSE was observed for 5cm. At the same point, RMSE was calculated as 1.86˚C for 2D200F. However, it is acceptable that this value is bigger than the other models due to temperature fluctuations in the corresponding experiment, as shown in Figure 6.10.

Table 6.12 Overview of pre-calculated RMSE values

	Root Mean Square Error of each model for same measuring points	
Code	**For 5cm**	**For 15cm**
2D400F	1.57	1.97
3D400F	1.50	1.69
4D400F	1.79	1.84
2D200F	1.86	1.83
2D400F5	2.01	1.09
Code	**For 30cm**	**For 50cm**
2D400F	0.56	0.72
3D400F	0.47	0.45
4D400F	0.40	0.73
2D200F	0.19	0.30
2D400F5	0.53	0.67
Code	**For 70cm**	**For 85cm**
2D400F	0.69	1.33
3D400F	0.66	1.16
4D400F	0.61	1.57
2D200F	0.59	0.60
2D400F5	0.73	1.52

RMSE values differ from 1.69 to 1.97; the maximum efficiency of the model is observed for 3D400F, where the minimum is 1.69. While there is no observed cause for this difference, the values are in the range required for model validation.

For 30cm, 50cm, and 70cm, middle layers of the domain, RMSE values differ from 0.4 to 0.73 in all models. These low RMSE values indicate the model results are closer to the experimental results in these layers when compared to other measuring

points. When it comes to model 2D200F, the RMSE values are the smallest ones, especially for 30cm and 50cm. This situation can be caused by the corresponding experiment having less temperature stratified layer when compared to other experiments.

In conclusion, verifying models shows that the base model is applicable for different diffuser diameters and air flow rates for the destratification of temperature stratified water column by air diffuser.

CHAPTER 7

COMPARISONS FOR SUB-MODELS OF TURBULENCE AND MULTIPHASE IN FLUENT

This study examines the mixing process of the temperature stratified water column by air diffuser and generates a numerical model serving this. Two main issues occur; choosing the most convenient multiphase and turbulence model to fit experimental studies best. Chapter 6 includes the generated models and comparisons of them with the related experiments, and in chapter 5, the base model steps and parameters are introduced, also in chapter 4, the theory behind the numerical modeling of multiphase flows and turbulence flow was explained. In this chapter, In this chapter, model selection for turbulence and multiphase flows are discussed.

As mentioned before, the selection of the multiphase model and turbulence model is critical. The first selection of the multiphase model will be explained since it affects the simulation of the hydrodynamics directly according to the *Ansys Fluent Theory Guide* and.

As a reminder, for all simulations of this chapter, the energy equation was activated for temperature assignments.

7.1. Choosing the Multiphase Model

Fluent has four available options for simulation of the multiphase flows, as explained before in chapter 4; discrete particle method, the volume of fluid model, mixture model, and Eulerian model. According to limitations (*ANSYS FLUENT User's Guide* 2021) and problem descriptions, the discrete phase method and the volume of fraction method were eliminated, so the model for multiphase flow simulation was restricted only for the mixture and the Eulerian model. Since the Eulerian model requires

more computational power and has more complexity, the first choice for the multiphase flow was the mixture model.

7.1.1. Mixture Model Studies and Comparisons

This section includes two different simulations, which are identical except for the boundary conditions. Both simulations were established to compare the experiment of the 2mm air diffuser diameter and 200 l/h air flow rate.

The fluid domain, geometry, and mesh were generated as described in sections 5.1, 5.2, and 0 orderly. In Fluent, the solver type was chosen as “pressure-based” and “transient.” The gravitational acceleration was set as -9.81 m^2/s in the Y direction.

As a turbulence model, SST k-ω was selected, and the parameters for the mixture model are given in Table 7.1.

Table 7.1 Mixture Model Parameters

	Multiphase Model
Type	Mixture
Volume Fraction Parameters	Implicit
Number of Phases	2
Phase-1 (primary)	Water
Phase-2 (secondary)	Air, with a constant diameter of 1.2mm
Phase Interaction	Drag Force schiller-naumann Slip Velocity manninen-et-al
	Interfacial Area ia-symmetric

For this study, the secondary phase was air, with a constant diameter of 1.2mm means the bubble diameters. This value was assigned based on the measurement of the corresponding experiment, where the primary phase was water with rearranged properties, which will be explained following.

The material properties of water and air were the same as listed in Table 5.3. Properties of air were taken as defaults in the Fluent database, where some water properties were updated due to the absence of different temperatures of the fluid domain. The viscosity and density of water were considered temperature-dependent. For the density of water, equation (5.3) was set to model, as shown in Figure 5.8. Also, for the viscosity of water, the "Sutherland Law" was used with a reference temperature and reference viscosity value, as can be seen in Figure 5.9.

The boundary condition for air entrance to the domain, the mass-flow inlet option, was selected, suitable for compressible flows (*Ansys Fluent Theory Guide* 2021). The mixture multiphase model enables setting the parameters for phases separately, so for the primary phase, water, "0" was set; means no water entrance to the domain. For dispersed phase air, the value of 2.30e-05 kg/s was set with a temperature of 20˚C. These values were determined according to the corresponding experiment. In the experiment, the air flow rate was 200l/h, and it was rearranged using equation (6.1) for the mass-flow inlet boundary condition. Air mass flow rate was calculated as 6.81e-05 kg/s for the experiment, and one-third of this value was set to the model. The temperature value of air in the model was fixed the same as the room temperature during the experiment.

For the sides of the fluid domain, the wall boundary condition was selected with the properties of stationary wall and heat flux.

The importance of the selection boundary condition will be discussed with the results in the last of this head. The options for the outlet boundary condition can be listed as follows:

- Pressure outlet,
- Outflow
- Mass-flow outlet,
- Symmetry

The options of pressure outlet and outflow were eliminated due to their behavior characteristics. When the pressure-outlet was chosen, some problems were observed

about backflow, which affects the air entrance to the domain; the outflow boundary condition is applicable to models with unknown parameters, like pressure, at outlets. So the remaining two options, mass-flow outlet, and symmetry were used for two separate simulations, and the results are the issue of this chapter.

As initial temperatures, the values were used in Table 6.8 since the corresponding experiment of this model is the same.

The simulations were run for different times depending on their mixing process, but the same time step size,0.05, was used.

7.1.1.1. Results of the Simulation with the Boundary Condition of Symmetry for the Outlet

This simulation was established as explained above, and the symmetry boundary condition was set for the outlet, the upper face of the "fluid domain" body. Theoretically, the symmetry boundary condition is considered for the wall boundary. When the symmetry is defined, the mirror symmetry is obtained for that boundary. In this study, since the thermal conditions and air volume fraction specifications were unknown for the outlet, the symmetry boundary condition would be appropriate and applied for trial.

The initial temperature conditions were introduced to the model, ranging from 0 degrees to 30 degrees from the bottom to the top. The simulation was run for 300 seconds in total, and the display of the temperature distribution contours at initial, 100 seconds, 200 seconds, and final, can be shown in Figure 7.1. It is clear that, 300 seconds would be sufficient for complete mixing, red and blue contours representing the maximum and minimum temperatures disappeared after 100 seconds. At 300 seconds, the colored contours, the temperature layers, became too indistinct to be distinguished.

Behind the visualization, charts were obtained (Figure 7.2), drawn at the same measuring points for numerical and experimental results as a time series. When the charts are examined, the inconsistency of the numerical model is apparent. Although the model for the middle layers seems to be compatible with the experiment, it is clear that there are serious temperature differences when examined in detail. For example, at 70cm at 100seconds, the temperature in the model is 20˚C, whereas the experiment is at 24˚C.

Also, the inconsistency between the experiment and numerical model can be seen for 85cm. In the numerical model, the temperature of the mixed domain is about 20˚C, indicating from the final temperatures of all measuring points. The most significant inconsistency was observed at 5cm, which reached the completed mixing temperature in 300 seconds when the test temperature was around 10˚C for the same time.

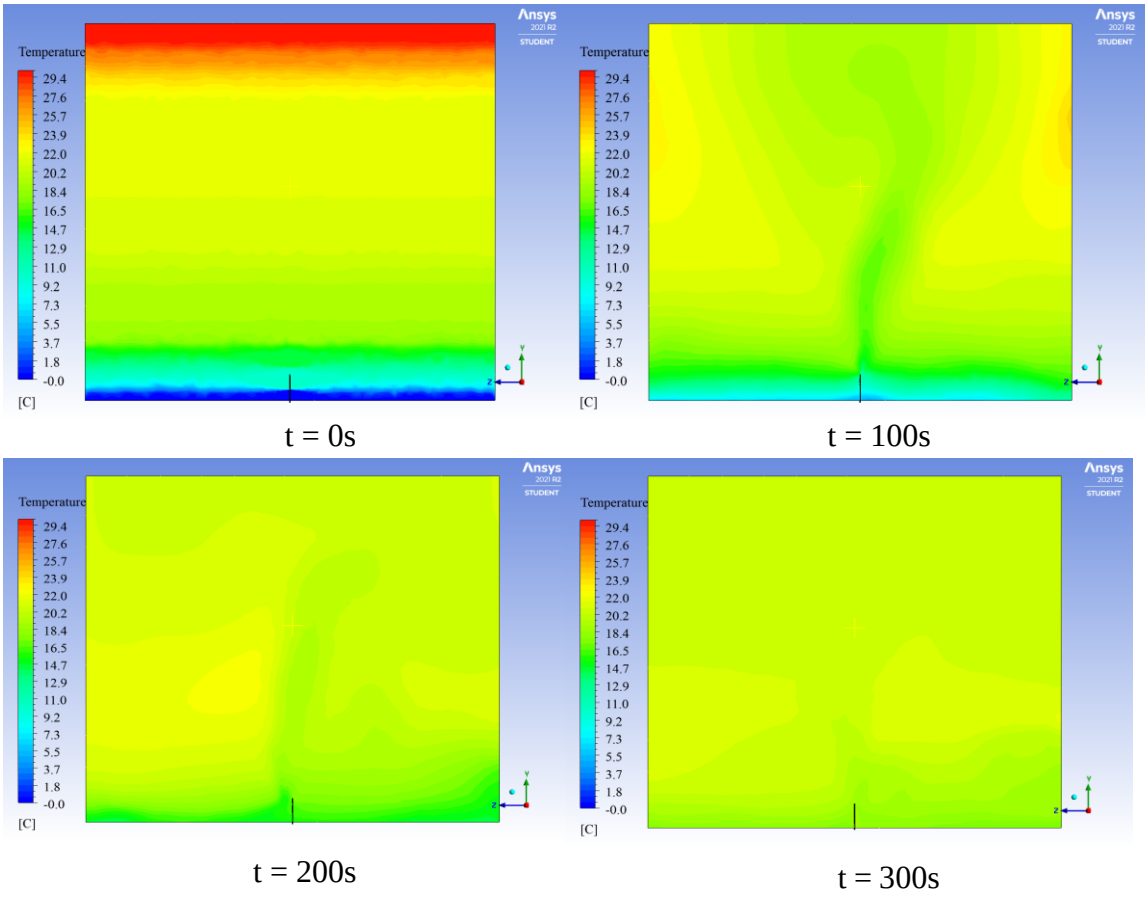

Figure 7.1. Temperature distribution contours for the simulation with the symmetry boundary condition at different times

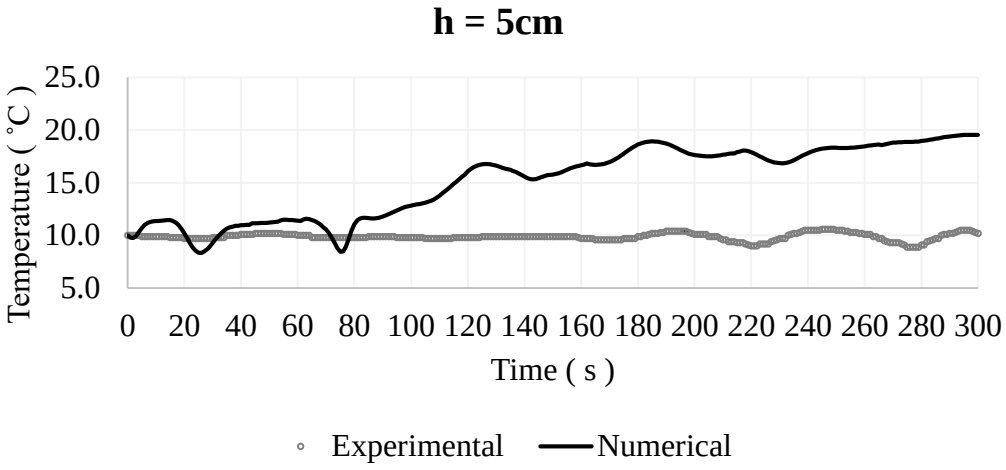
h = 5cm
Temperature (˚C)
25.0
20.0
15.0
10.0
5.0
0 20 40 60 80 100 120 140 160 180 200 220 240 260 280 300
Time (s)
Experimental
Numerical

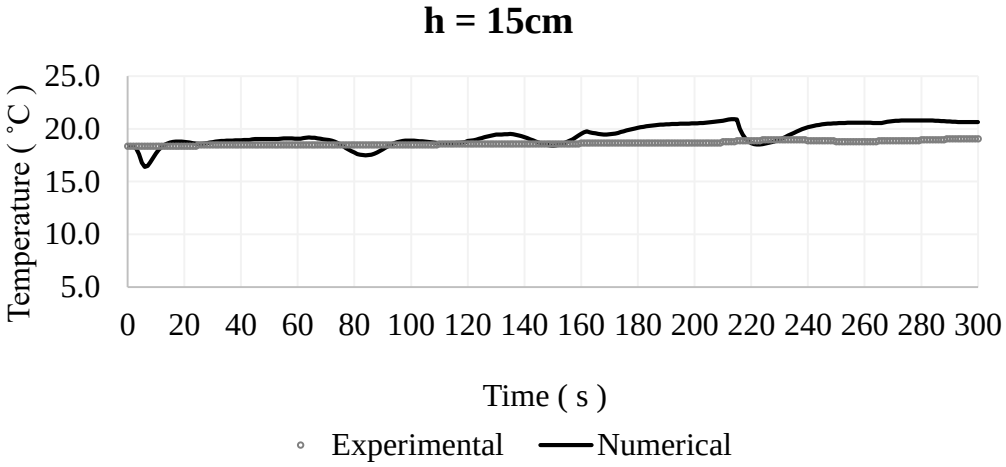
h = 15cm
Temperature (˚C)
25.0
20.0
15.0
10.0
5.0
0 20 40 60 80 100 120 140 160 180 200 220 240 260 280 300
Time (s)
Experimental
Numerical

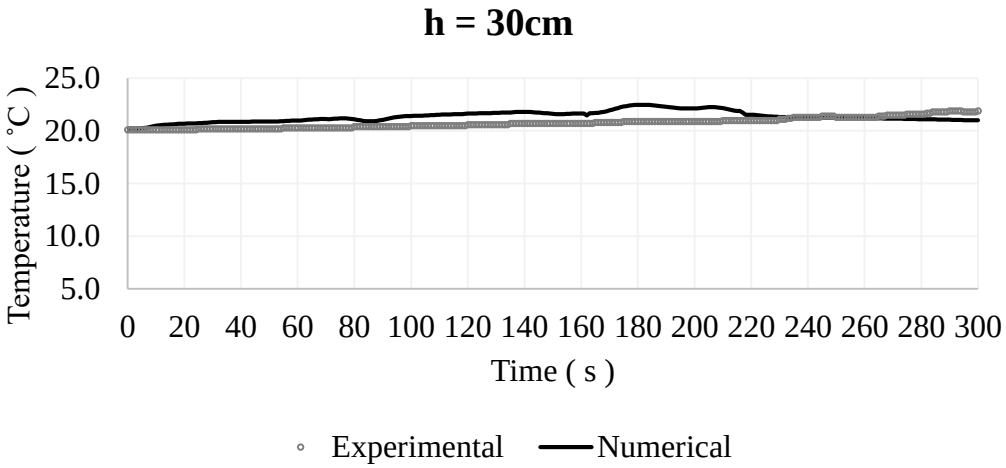
h = 30cm
Temperature (˚C)
25.0
20.0
15.0
10.0
5.0
0 20 40 60 80 100 120 140 160 180 200 220 240 260 280 300
Time (s)
Experimental
Numerical

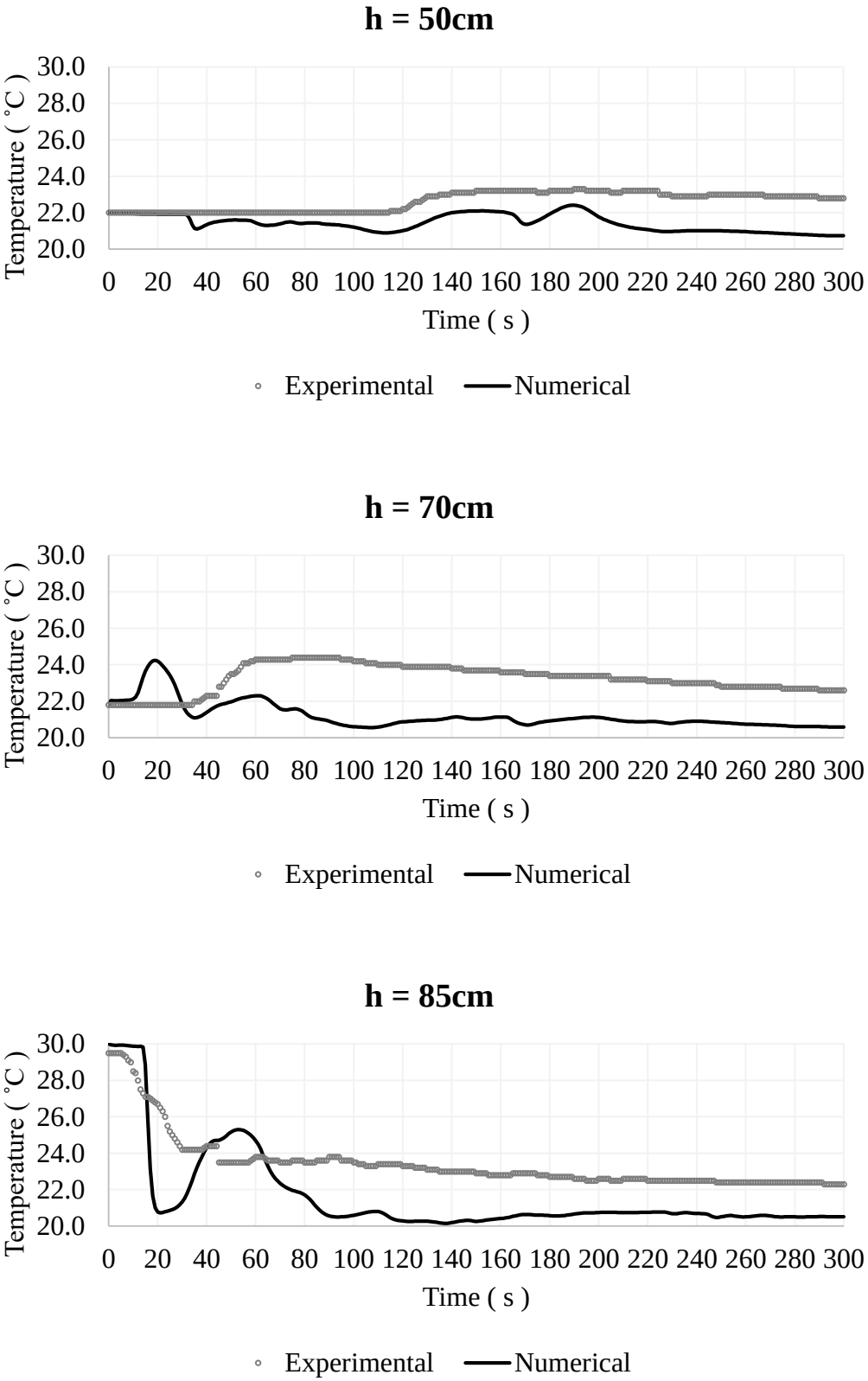

Figure 7.2 Temperature results of experimental and numerical in time series for symmetry boundary condition

After the results were taken, it was observed that the main problem causing that quick mixing was the air behavior in the domain. The given air from the bottom of the water column did not leave the domain and circulate through the domain, so the mixing process was completed against the experimental studies. The visualization of the air volume fraction in the plane with the lines of the air diffuser at 100seconds and 300 seconds can be shown in Figure 7.3.

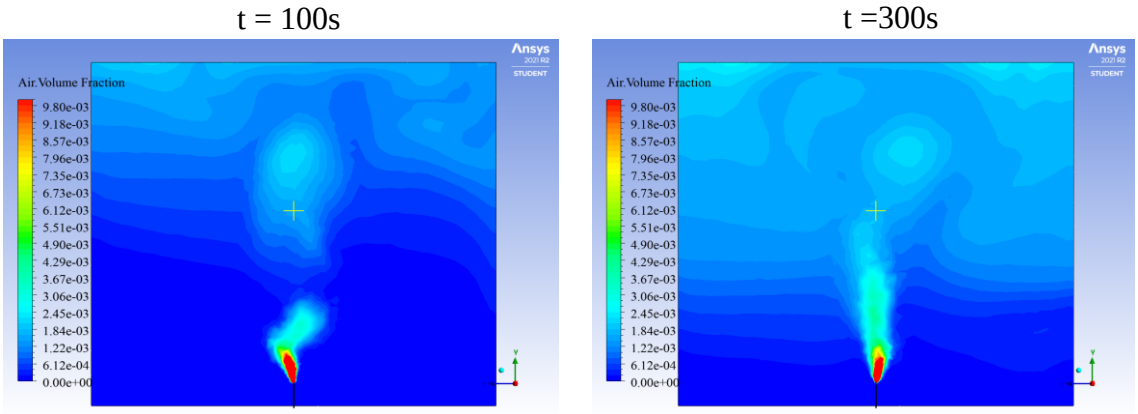

Figure 7.3. Air volume fractions in the domain at t=100 s and t=300s

To see the effects of the turbulence model, some changes and arrangements were applied, but there was no noticeable difference in simulation results. Then it was decided that the symmetry boundary condition for the outlet is not suitable for this study since it does not allow air to exit the domain. To develop the model, the new trial was done with the mass-flow outlet boundary condition for the outlet.

7.1.1.2. Results of the Simulation with the Boundary Condition of Mass-flow Outlet for the Outlet

This simulation was established as explained above, and the mass flow outlet boundary condition was set for the outlet, the upper face of the “fluid domain” body. It was chosen to serve the idea that the given air, dispersed phase, leaves the domain. Since the mixture multiphase model allows to set boundary conditions for each phase separately, the mass flow rate was set as zero for water, meaning that no water leaves the domain, as it is in the experimental studies. For the dispersed phase, the air, it was allowed to leave the field.

The initial temperature conditions were introduced to the model, ranging from 0 degrees to 30 degrees from the bottom to the top. The simulation was run for 600 seconds in total, and the display of the temperature distribution contours at initial, 150 seconds, 300 seconds, and final, can be shown in Figure 7.4. It is clear that, 600 seconds would be sufficient for complete mixing, red and blue contours representing the maximum and minimum temperatures disappeared after 600 seconds, but in the corresponding experiment, the complete mixing time was around 1200 seconds. At final, the colored contours, the temperature layers, became too indistinct to be distinguished. Also, as seen by the colored layers, a thin red layer represents around 30 degrees on the top surface of the domain, which is entirely irrelevant for the actuals.

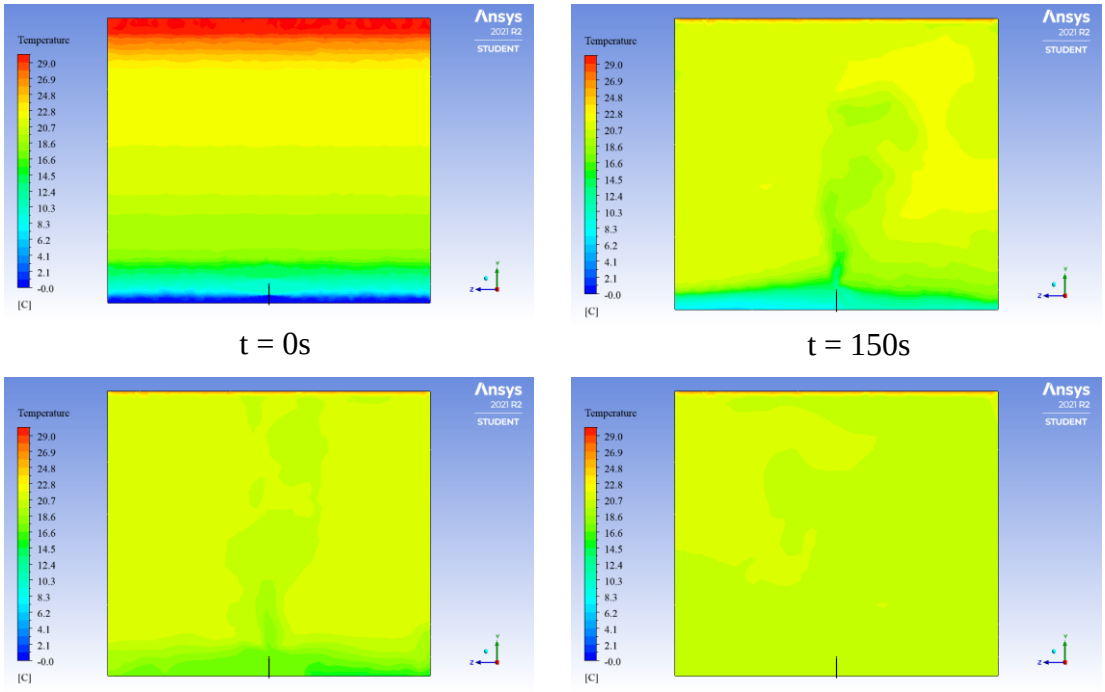

t = 0s t = 150s

t = 450s t = 600s

Figure 7.4. Temperature distribution contours for the simulation with the mass-flow outlet boundary condition at different times

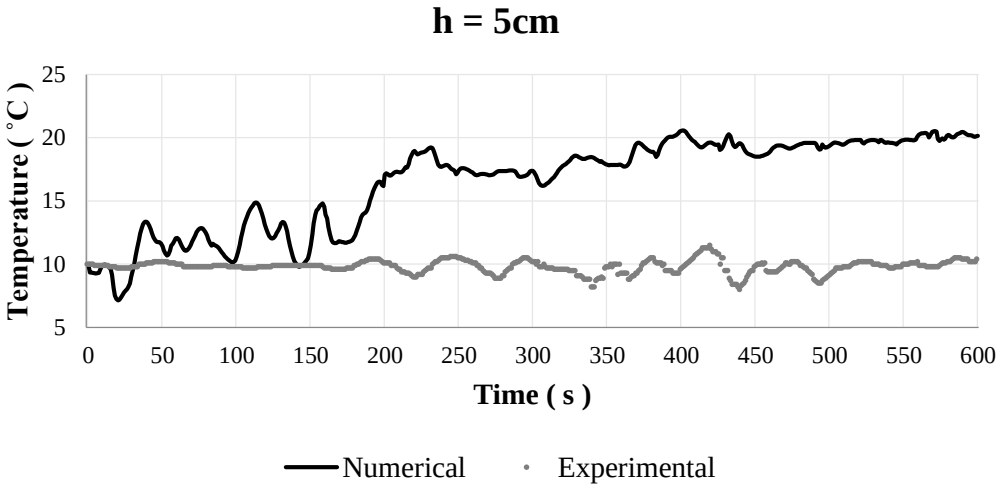
h = 5cm
Temperature (˚C)
25
20
15
10
5
0
50
100
150
200
250
300
350
400
450
500
550
600
Time (s)
Numerical
Experimental

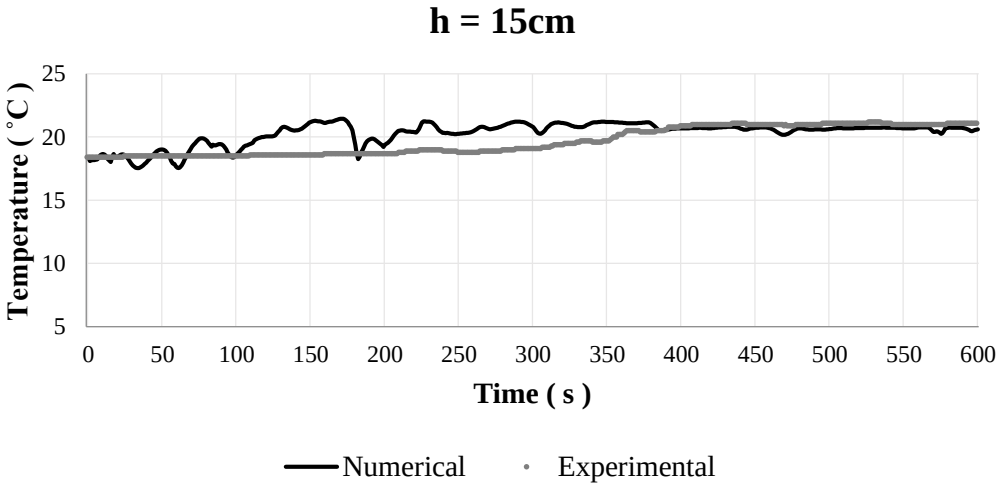
h = 15cm
Temperature (˚C)
25
20
15
10
5
0
50
100
150
200
250
300
350
400
450
500
550
600
Time (s)
Numerical
Experimental

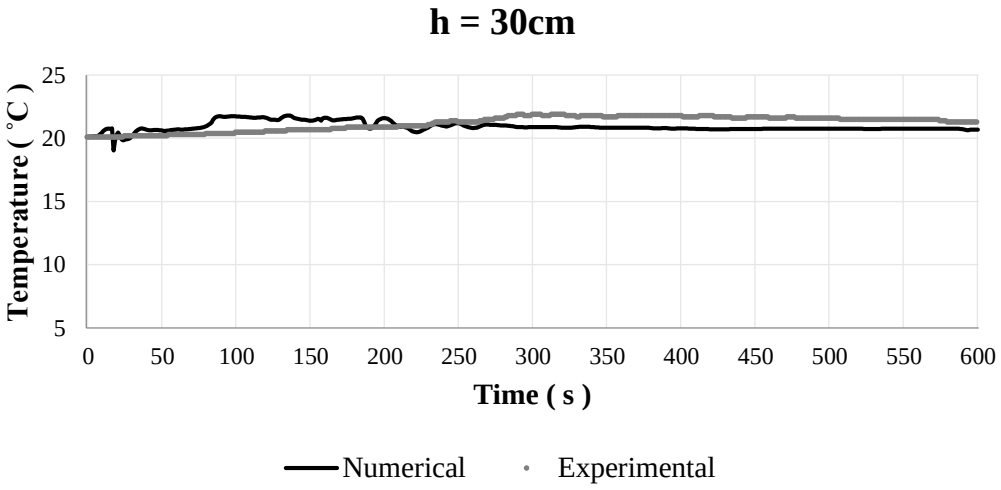
h = 30cm
Temperature (˚C)
25
20
15
10
5
0
50
100
150
200
250
300
350
400
450
500
550
600
Time (s)
Numerical
Experimental

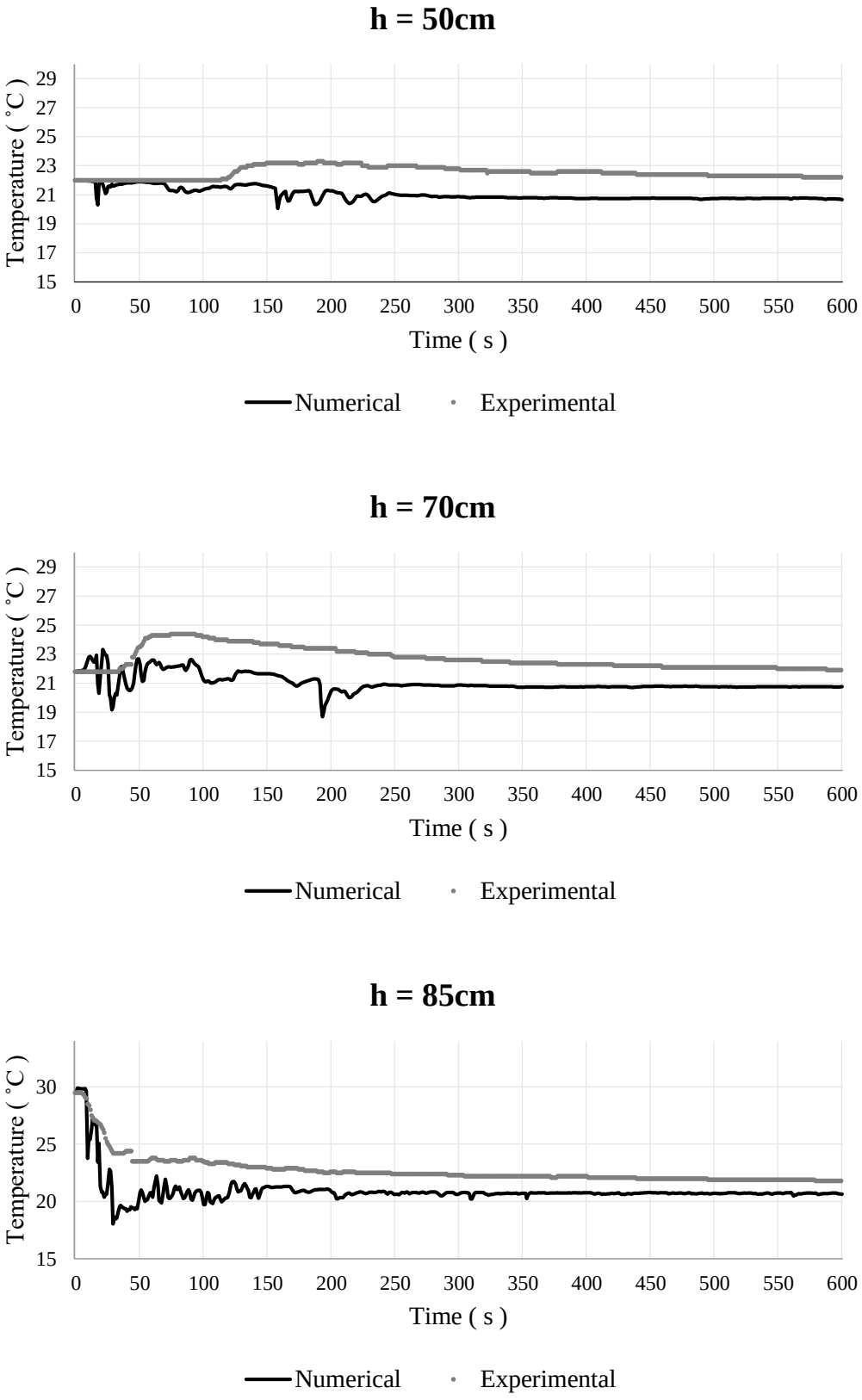

Figure 7.5 Temperature results of experimental and numerical in time series for mass-flow outlet boundary condition

For comparisons of numerical and experimental results in time series, charts are given in Figure 7.5. When examined from the graphics, the first striking feature is that there are too many temperature fluctuations in the numerical model compared to the experiments at almost every measurement point. At 70cm and 85cm, there were temperature differences around 6˚C - 7˚C at the same time. Also, it can be seen that the changing temperature patterns, in terms of increasing and decreasing trends, of the numerical model, were dissimilar to the experimental ones at 50cm and 70cm. Apart from these, the most significant difference was in 5cm. At the final time of the simulation, 600 seconds, the temperature was around 20˚C, which is the temperature of the fluid domain mixed entirely in the numerical model; in contrast, it was 10.5˚C in the corresponding experiment.

Also, RMSE and MAE values were calculated for each measuring point and provided in Table 7.2.

Table 7.2 RMSE and MAE values for mass-flow outlet boundary condition

Heights (cm)	Root Mean Square Error (RMSE)	Mean Absolute Error (MAE)
5	7.594	6.764
15	1.190	0.945
30	0.793	0.736
50	1.637	1.508
70	1.868	1.767
85	2.061	1.833

Besides the contour display and charts, RMSE and MAE values also show the incompatibility of the numerical model and the corresponding experiment. The maximum RMSE value was detected at 5cm; when the RMSE value is re-arranged as the ratio of the maximum temperature value in the experiment for the exact location, it was found as 66%. If RMSE is re-evaluated as the ratio of the time-averaged temperature value in the experiment for the exact location, it was calculated as 77%. Under these findings, it is hard to talk about the accuracy of the numerical model.

When the effect of boundary conditions on the accuracy of the numerical model is argued, the mass-flow outlet boundary condition gives more reliable results according

to the relevant experiment. Nevertheless, the result of the mixture model with mass-flow outlet boundary condition is not sufficient to say that the numerical model results are acceptably compatible. Consequently, it was decided that the problem can be caused by the multiphase model selection, not the boundary condition selection in the mixture multiphase model. For this reason, the other option for modeling the multiphase flows, the Eulerian model, was applied. The simulation results with the Eulerian multiphase model and comparison of it with the experimental results under the conditions of air diffuser with 2mm and air flow rate of 400l/h had already been provided in section 6.1. The comparison of the RMSE and MAE values of the mixture model (in Table 7.2) and the Eulerian multiphase model (Table 6.3) shows that the Eulerian model is the most suitable for this study. Hence, the Eulerian model was decided as the multiphase model. After deciding on the multiphase model, the appropriate turbulence model in the Eulerian model will be discussed in the next section.

7.2. Choosing the Turbulence Model

Each turbulence model in Fluent uses the equations with some specifications, so different turbulence models may give different results. The detailed information about turbulence models in Fluent was provided in chapter 4. Since this study includes both numerical and experimental studies and comparisons of the numerical models to the experimental ones, the selection of turbulence models has an important role.

All different turbulence models discussed in this section were set on identical numerical models that have the only difference between them is the turbulence model. Turbulence model comparison was carried out for the time interval of 60 seconds and 240 seconds oo the specific model instead of the simulation for 600 seconds. The chosen specific model was explained and discussed in section 6.1. and general information about the model setup and solver was provided in chapter 5.

There are three options available for the turbulence model under the Eulerian multiphase model since the specific model mentioned above was set for the Eulerian model. These turbulence models are k-Ɛ, k-ω, and Reynold stress models.

In section 6.1, the model has already been simulated with the k-ω turbulence model. The solution and result files of that simulation at 60 seconds were recorded and transferred to another Fluent solver. Then the new simulation was started with the data at 60 seconds and changed turbulence models. For comparison, the simulation was run for 180 seconds from 60 seconds to 240 seconds for all three turbulence models. The accuracy of the turbulence models was evaluated by the comparison of the results with the experimental ones for the same time interval of 60 and 240 seconds. Finally, the three data sets were obtained for three different turbulence models of k-Ɛ, k-ω, and Reynold stress, which were compared with the experimental results.

Turbulence models were compared to experimental results for specified time intervals as time series, given in Figure 7.6.

Except for the measuring point of 85cm, there is no significant difference in turbulence models, but it can be said that the simulation with the Reynold stress model (RSM) has more temperature fluctuations due to it solves extra five equations in 3D models (*Ansys Fluent Theory Guide* 2021) where the k-Ɛ and k-ω turbulence model solve the two-equation. According to the charts, the results of k-Ɛ and k-ω turbulence models are so close to each other, whereas the RSM is a bit closer to the experimental results.

For better examination, RSM and MAE values of each turbulence model comparing the experimental results were calculated for all measuring points and provided in Table 7.3.

The comments on RMSE values are more precise than the chart comments. For 5cm, the best fit is for RSM, and the worst is for the k-Ɛ model. The ratio of the RMSE values to time-averaged temperatures in the experiment are 11%, 15%, and 10% as in the order of k-ω, k-Ɛ and RSM.

For 15cm, the difference between turbulence models is less than in 5cm, but the precision order is the same as 5cm, which is of RSM, k-ω, and k-Ɛ from the best to the worst.

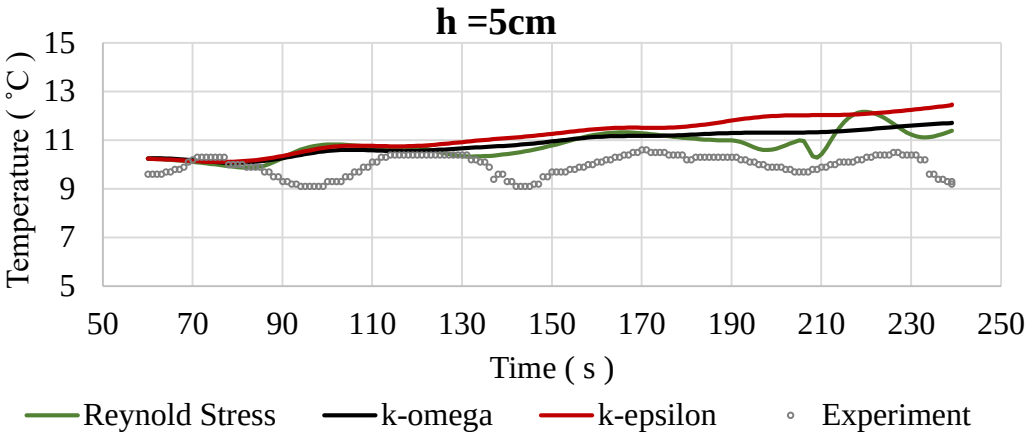
h =5cm
Temperature (°C)
15
13
11
9
7
5
50 70 90 110 130 150 170 190 210 230 250
Time (s)
Reynold Stress
k-omega
k-epsilon
Experiment

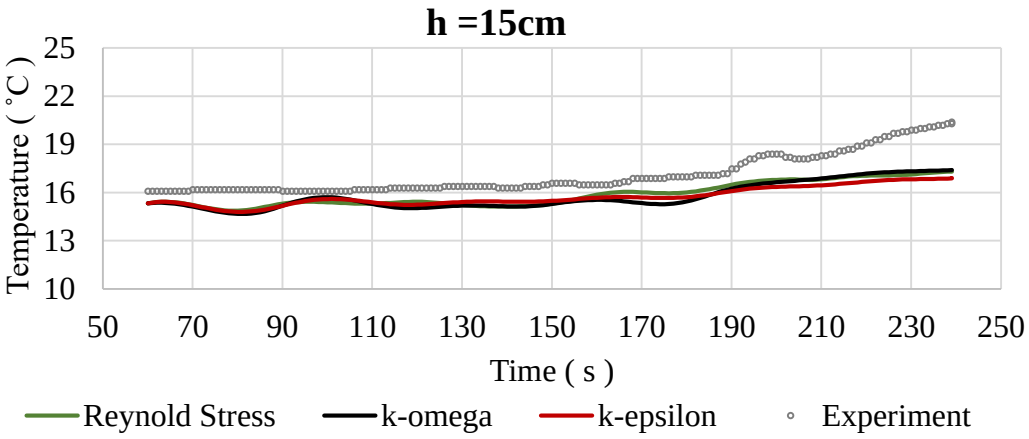
h =15cm
Temperature (°C)
25
22
19
16
13
10
50 70 90 110 130 150 170 190 210 230 250
Time (s)
Reynold Stress
k-omega
k-epsilon
Experiment

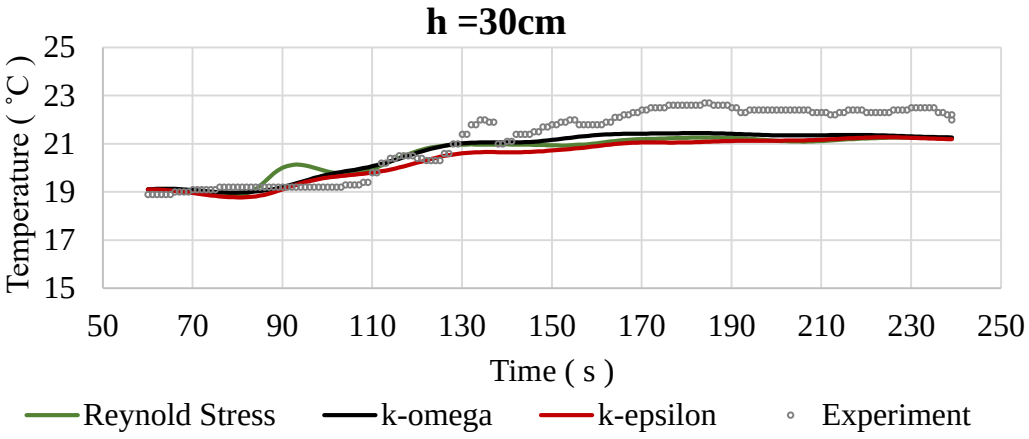
h =30cm
Temperature (°C)
25
23
21
19
17
15
50 70 90 110 130 150 170 190 210 230 250
Time (s)
Reynold Stress
k-omega
k-epsilon
Experiment

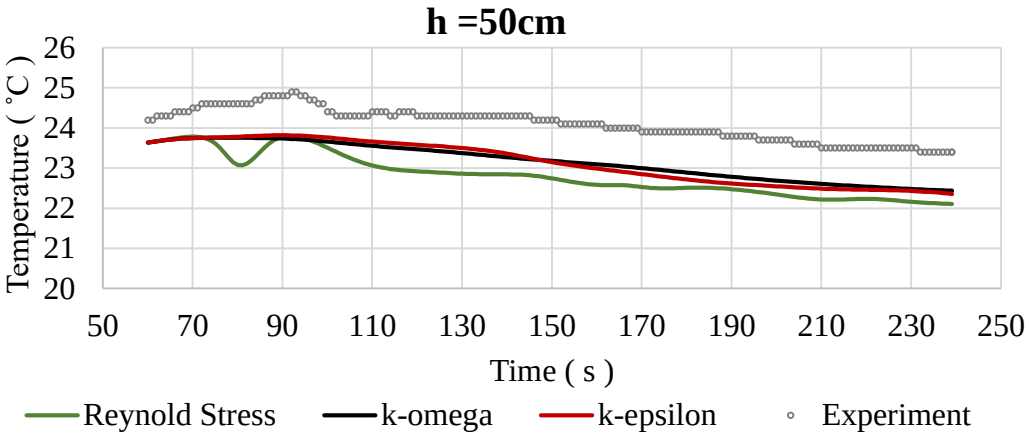

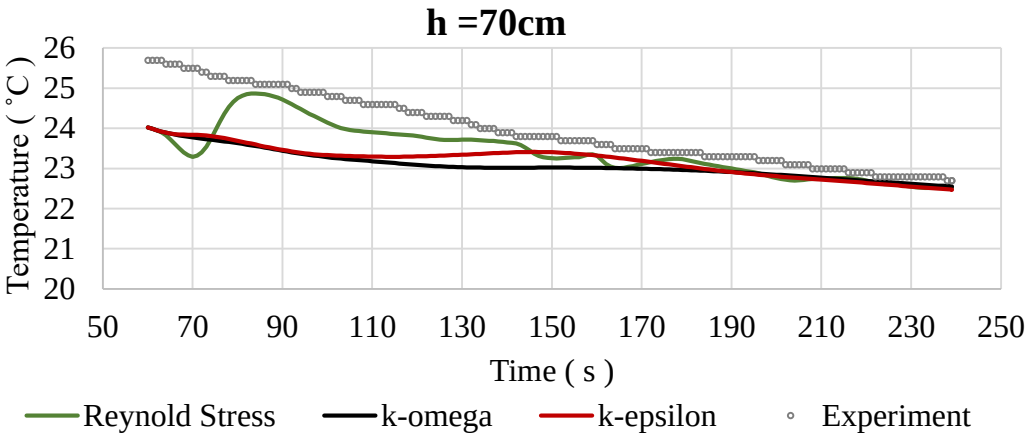

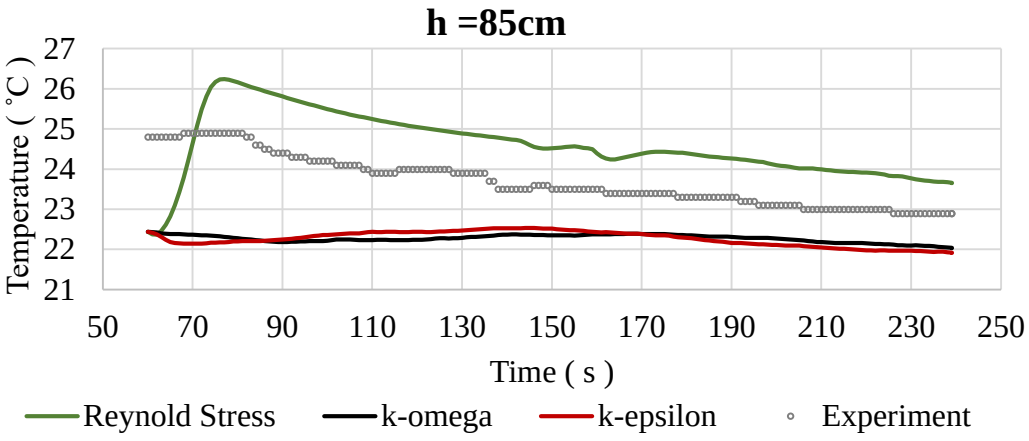

Figure 7.6. Turbulence model comparisons with experimental data

For 30cm and 50cm, the results show that the k-ω have the best accuracy than the others, whereas the RSM have the best for the heights of 70cm and 85cm.

Table 7.3. RMSE and MAE values for turbulence model comparison

Height (cm)	**Root Mean Square Error (RMSE)**		
	k-ω model	k-Ɛ model	Reynold stress model (RSM)
5	1.09	1.47	1.01
15	1.46	1.55	1.37
30	0.75	0.95	0.90
50	0.94	0.97	1.30
70	1.04	0.95	0.70
85	1.55	1.55	1.14
Height (cm)	**Mean Absolute Error (MAE)**		
	k-ω model	k-Ɛ model	Reynold stress model
5	0.94	1.28	0.86
15	1.36	1.37	1.24
30	0.63	0.81	0.78
50	0.93	0.95	1.28
70	0.88	0.77	0.53
85	1.43	1.43	1.10

As a result of this comparison, the RSM was the turbulence model that gave the closest results to the other turbulence model for 4 of the 6 measurement points. The k-ω turbulence model has more effective performance than the k-Ɛ turbulence model for 5 of the 6 measuring points. Hence, the k-Ɛ turbulence model was eliminated, and the remaining options for turbulence model selection were RSM and the k-ω model. One of them, the k-ω turbulence model, was selected because the Reynolds stress model requires more computational power and time since it solves seven equations for the solution.

7.3. Summary of Turbulence and Multiphase Model Selection

This chapter discussed sub-models for turbulence and multiphase flows with their limitations and precision for this study.

Two different multiphase models, the mixture and the Eulerian, and two different boundary conditions for the mixture model were examined. It was observed that the

symmetry boundary condition for the outlet was entirely inappropriate for this kind of study. The mass-flow outlet boundary condition in the mixture multiphase model represented the better approximation to the experimental results but not enough since this study aims to obtain a numerical model for precise temperatures values at a specific time for both experimental and numerical studies. To criticize the application of the mass-flow outlet boundary condition in this section, it would have given better results if User-Defined-Functions (UDF) were written to define the leaving of air from the domain. After the comparisons, the Eulerian multiphase model was selected for simulations having more effective performance since there is a boundary condition, named "degassing," available only in the Eulerian multiphase model and allows for air to leave the domain without any extra arrangements.

Three turbulence models, k-Ɛ, k-ω, and Reynolds stress model (RSM), were examined in selecting the Eulerian multiphase model. After trials and evaluations, it was observed that the RSM has the best performance, the k-ω tracks the RSM, and the k-Ɛ is the worst one. Since the RSM has complexity and solves seven equations in three-dimensional models, it consumes more computational power and time than the other two-equation models, which are k-ω and k-Ɛ. Hence, the k-ω turbulence model was selected for the simulations.

CHAPTER 8

DISCUSSION AND CONCLUSION

This thesis aims to develop a validated numerical model for the concept of the artificial destratification of the thermally stratified water column by air diffusers. The numerical model studies were performed via the ANSYS Fluent software. Also, a series of experiments were carried out in the Hydraulics Laboratory at the Izmir Institute of Technology for model verification.

In the experimental studies, six experiments were performed using different configurations of air diffusers having different hole diameters and air flow rates to investigate the sensitivity of the destratification process to these parameters. Based on the nondimensional parameters in the literature, the destratification efficiency was calculated and compared to the literature. As a result, it was observed that when the air flow rate is increased, the destratification duration decreases at some heights of the water column, but the destratification efficiency has not been affected by this parameter directly. The mixing time in total was not affected by the increasing diameter of the air diffuser; still, the relationship between air diffuser diameter and destratification efficiency was observed to be linear. The comparison of observed and simulated temperature time series was discussed for each experiment through error analysis and calculated RMSE and MAE values were compared.

After a thorough analysis for the best model selection for the simulation of hydrodynamics in the experimental setup, the Eulerian model was selected as the best multiphase model for the purposes of the study. At first, based on the provided limitations, the mixture and the Eulerian multiphase model were considered to simulate the multiphase flows. For the mixture multiphase model, two boundary conditions of "symmetry" and "mass-flow outlet" were applied for the outlet corresponding to the top of the water tank, which is open to the atmosphere in experiments. While the "symmetry" boundary condition was found to be entirely unsuitable for such applications, the "mass-flow outlet" gave results closer to the experimental ones; still, for the mass flow outlet condition, there was too much time inconsistency to be tolerated compared to the

experiment. Eventually, the appropriate multiphase model was chosen as the Eulerian model. This selection was primarily due to the boundary condition option “degassing” that gave the best results for our physical problem where the destratification process was mainly dominated by the air bubbles.

Next, the most appropriate turbulence model was selected. For this purpose, turbulence models available in the Eulerian multiphase model were tested; k-Ɛ, k-ω, and Reynolds stress (RSM) models. After comparing the RMSE values calculated for each turbulence comparison with the experimental results, it was found that the Reynolds stress model gave the best results, with the range of RMSE values from 0.7 to 1.37, and the k-ω turbulence model came second with insignificant differences, with the RMSE values from 0.75 to 1.46 (corresponding to 2-5% of the maximum temperature). Considering the extensive computational power and time Reynolds stress model required for the simulation of our model domain, the k-ω turbulence model was selected during the simulations.

After the calibration of the model, a comparison of the simulated and observed temperature values indicated a good performance of the numerical models. Considering the error calculations, the RMSE values differed from 0.2 to 1.97 for general. The best agreement between the model and the observations was achieved in the upper hypolimnion, the middle layers of the water columns. For epilimnion, the average RMSE was observed as around 1 for all simulations and 1.8 on average for the bottom hypolimnion.

FUTURE WORKS

The planned future works include two headings as developing the numerical model and application of the numerical model to real-case studies.

In numerical models discussed in this thesis, the bubble diameter was assigned as a constant for the multiphase model, where this constant diameter data was taken from the measurements during the experiments. However, the multiphase flow modeling in Fluent allows the examination of the hydrodynamics of bubbles, meaning that the changing bubble diameters and distribution of them in the primary phase. Due to the

limited time frame and insufficient computational power, large parameters of the dispersed phase were not included in this study. If these parameters are applied, the hydrodynamic bubble behavior in the thermally stratified water column could be examined in detail.

The other planned and has already begun study is the investigation of the Tahtalı reservoir since temperature, water intake discharge, and velocity information are available. The actual dimensions of the reservoir were scaled in 1/100 based on the similarity of nondimensional Froude number, and the domain was generated and meshed in Fluent. However, this is a little bit complex model due to the inputs and outputs of the fluid domain. This planned study aims to build designing parameters for the artificial destratification of the Tahtalı reservoir by air diffuser.

REFERENCES

Anderson, John D. 1995. *Computational Fluid Dynamics : The Basics with Applications*. McGraw-Hill.

Andersson, Bengt, Ronnie Andersson, Love Håkansson, Mikael Mortensen, Rahman Sudiyo, and Berend Van Wachem. 2011. "Computational Fluid Dynamics for Engineers." *Computational Fluid Dynamics for Engineers* 9781107018952 (January): 1–189. https://doi.org/10.1017/CBO9781139093590.

Andersson, Bengt, Chemical Engineering, Ronnie Andersson, Chemical Engineering, Chalmers Uni-, Epsilon Hightech, Engineering Data Resources, 2012. *Computational Fluid Dynamics*.

Ansys Fluent Theory Guide. 2021. *ANSYS Inc., USA*. Vol. 15317. http://scholar.google.com/scholar?hl=en&btnG=Search&q=intitle:ANSYS+FLUENT+Theory+Guide#0.

ANSYS FLUENT User 's Guide. 2021. *Knowledge Creation Diffusion Utilization*. Vol. 15317.

Asaeda, Takashi, and Jörg Imberger. 1993. "Structure of Bubble Plumes in Linearly Stratified Environments." *Journal of Fluid Mechanics* 249: 35–57. https://doi.org/10.1017/S0022112093001065.

Ashton, George D. 1974. "COLD REGIONS RESEARCH AND ENGINEERING LABORATORY."

Benndorf, J. 1988. "G. D. Cooke, E. B. Welch. S. A. Peterson and P. R. Newroth: Lake and Reservoir Restauration. Boston, Butterworth Publishers, 1986, 392 S., Zahlr. Abb. u. Tab., Hardcover L 96.–, ISBN 0-250-40643-8." *Acta Hydrochimica et Hydrobiologica* 16 (5): 557–557. https://doi.org/10.1002/AHEH.19880160520.

Biesheuvel, A., and S. Spoelstra. 1989. "The Added Mass Coefficient of a Dispersion of Spherical Gas Bubbles in Liquid." *International Journal of Multiphase Flow* 15 (6): 911–24. https://doi.org/10.1016/0301-9322(89)90020-7.

Bruun, Per M. 1975. "Discussions of 'Engineering Challenges of Dredged Material

Disposal.'" *Journal of the Waterways, Harbors, and Coastal Engineering Division* 101 (4): 461–63. https://doi.org/10.1061/AWHCAR.0000298.

Clift, R, JR Grace, and ME Weber. 2005. "Bubbles, Drops, and Particles." https://sci-hub.ru/https://books.google.com/books?hl=tr&lr=&id=UUrOmD8niUQC&oi=fnd&pg=PP1&ots=pHwXXIbK6W&sig=VYkBv801Fhoj7Vgd4iZhenvyQX8.

Cox, Paul Alan, Sandra Anne Banack, and Susan J. Murch. 2003. "Biomagnification of Cyanobacterial Neurotoxins and Neurodegenerative Disease among the Chamorro People of Guam." *Proceedings of the National Academy of Sciences of the United States of America* 100 (23): 13380–83. https://doi.org/10.1073/PNAS.2235808100.

Crowe, Clayton T. 2005. "Multiphase Flow Handbook." *Multiphase Flow Handbook*, September. https://doi.org/10.1201/9781420040470.

Derksen, Jos, and Harry E.A. Van Den Akker. 1999. "Large Eddy Simulations on the Flow Driven by a Rushton Turbine." *AIChE Journal* 45 (2): 209–21. https://doi.org/10.1002/AIC.690450202.

Elçi, S. 2008. "Effects of Thermal Stratification and Mixing on Reservoir Water Quality." *DOI 10.1007/S10201-008-0240-X* 9 (2): 135–42. https://doi.org/10.1007/s10201-008-0240-x.

Elçi, S., and B. Ekmekçi. 2016. "Observational and Numerical Methods for Quantifying and Modeling of Turbulence in a Stratified Reservoir." *Journal of Applied Fluid Mechanics* 9 (4): 1603–14. https://doi.org/10.18869/acadpub.jafm.68.235.25112.

Elger, Donald F., C. T. Crowe, and John A. Roberson. 1996. "Engineering Fluid Mechanics," 540.

Gatski, T. B., M. Yousuff. Hussaini, and John L. (John Leask) Lumley. 1996. "Simulation and Modeling of Turbulent Flows.," 329.

Goossens, L.H.J. 1979. "Reservoir Destratification with Bubble Columns." Delft University Press. https://repository.tudelft.nl/islandora/object/uuid%3Ad181ff21-1a58-4d45-b921-d2772a55b083.

Griffiths, Dilwyn J., and Martin L. Saker. 2003. "The Palm Island Mystery Disease 20 Years on A Review of Research on the Cyanotoxin Cylindrospermopsin." *Environmental Toxicology* 18 (2): 78–93. https://doi.org/10.1002/TOX.10103.

Hank, Sarah, Richard Saurel, Olivier Le Metayer, Sarah Hank, Richard Saurel, and Olivier Le Metayer. 2011. “A Hyperbolic Eulerian Model for Dilute Two-Phase Suspensions.” *Journal of Modern Physics* 2 (9): 997–1011. https://doi.org/10.4236/JMP.2011.29120.

Hilborn, E. D., W. W. Carmichael, R. M. Soares, M. Yuan, J. C. Servaites, H. A. Barton, and S. M.F.O. Azevedo. 2007. “Serologic Evaluation of Human Microcystin Exposure.” *Environmental Toxicology* 22 (5): 459–63. https://doi.org/10.1002/TOX.20281.

Hinze, J. O. 1975. *Turbulence*. 2d ed. New York: McGraw-Hill.

Hirt, C. W., and B. D. Nichols. 1981. “Volume of Fluid (VOF) Method for the Dynamics of Free Boundaries.” *Journal of Computational Physics* 39 (1): 201–25. https://doi.org/10.1016/0021-9991(81)90145-5.

Holland, J. P., and C. H. , Jr Tate. 1984. “Investigation and Discussion of Techniques for Hypolimnion Aeration/Oxygenation.” https://apps.dtic.mil/sti/citations/ADA148701.

Hussain, N. A., and B. S. Narang. 1984. “Simplified Analysis of Air-Bubble Plumes in Moderately Stratified Environments.” *Journal of Heat Transfer* 106 (3): 543–51. https://doi.org/10.1115/1.3246713.

Kim, Sung Hoon, Jae-yun Kim, Heekyung Park, and No-Suk Park. 2010. “Effects of Bubble Size and Diffusing Area on Destratification Efficiency in Bubble Plumes of Two-Layer Stratification.” *Journal of Hydraulic Engineering* 136 (2): 106–15. https://doi.org/10.1061/(ASCE)hy.1943-7900.0000152.

Kipke, K. 1983. “Analysis and Simulation of Mixing of Stratified Lakes or Reservoirs,” no. 305.

Kobus, Helmut E, and Research Engineer. 1968. “ANALYSIS OF THE FLOW INDUCED BY AIR-BUBBLE SYSTEMS.” *Coastal Engineering Proceedings* 2 (11): 65–65. https://doi.org/10.9753/ICCE.V11.65.

Larsen, Ian. 1962. “Pneumatic Barrier Against Salt Water Intrusion.” *Transactions of the American Society of Civil Engineers* 127 (4): 475–87. https://doi.org/10.1061/TACEAT.0008615.

Launder, B. E., and D. B. Spalding. 1972. “Lectures in Mathematical Models of Turbulence.” *Academic Press*, 176.

Lopez De Bertodano, Martin A. 1998. “Two Fluid Model for Two-Phase Turbulent Jets.” *Nuclear Engineering and Design* 179 (1): 65–74. https://doi.org/10.1016/S0029-5493(97)00244-6.

Manninen, Mikko, Veikko Taivassalo, Sirpa Kallio, and Åbo Akademi. 1996. “On the Mixture Model for Multiphase Flow.”

Mcdougall, Trevor J. 1978. “Bubble Plumes in Stratified Environments.” *Journal of Fluid Mechanics* 85 (4): 655–72. https://doi.org/10.1017/S0022112078000841.

Menter, Florian R. 2009. “Review of the Shear-Stress Transport Turbulence Model Experience from an Industrial Perspective.” *Https://Doi.Org/10.1080/10618560902773387* 23 (4): 305–16. https://doi.org/10.1080/10618560902773387.

Pastorok, Robert A., Marc W. Lorenzen, and Thomas C. Ginn. 1962. “Environmental Aspects of Artificial Aeration and Oxygenation of Reservoirs: A Review of Theory, Techniques, and Experiences - Technical Reports - USACE Digital Library.” 1962. https://usace.contentdm.oclc.org/digital/collection/p266001coll1/id/5865/.

ROBERSON, J. A., and C. T. CROWE. 1975. “ENGINEERING FLUID MECHANICS.,” no. (1975). https://doi.org/10.1201/9781315272337.

Schmitt, François G. 2008. “About Boussinesq’s Turbulent Viscosity Hypothesis: Historical Remarks and a Direct Evaluation of Its Validity.” https://doi.org/10.1016/j.crme.2007.08.004ï.

Socolofsky, Scott A., and E. Eric Adams. 2005. “Role of Slip Velocity in the Behavior of Stratified Multiphase Plumes.” *Journal of Hydraulic Engineering* 131 (4): 273–82. https://doi.org/10.1061/(ASCE)0733-9429(2005)131:4(273).

Sokolichin, A., and G. Eigenberger. 1994. “Gas-Liquid Flow in Bubble Columns and Loop Reactors: Part I. Detailed Modelling and Numerical Simulation.” *Chemical Engineering Science* 49 (24): 5735–46. https://doi.org/10.1016/0009-2509(94)00289-4.

Tennekes, H. (Hendrik), and John L. (John Leask) Lumley. 1972. “A First Course in

Turbulence," 300.

Theodore, Louis. 1971. *Transport Phenomena for Engineers*. Scranton: International Textbook Co.

Torrest, Robert, and John Wen. 1976. "Mixing and Circulation of Lakes and Reservoirs with Air Plumes." *NH Water Resources Research Center Scholarship*, January. https://scholars.unh.edu/nh_wrrc_scholarship/178.

Verrsteg, H., and Malalasekera W. 2007. "An Introduction to Computational Fluid Dynamics: The Finite Volume Method : Versteeg, H., Malalasekera, W.: Amazon.Com.Tr: Kitap." 2007. https://www.amazon.com.tr/Introduction-Computational-Fluid-Dynamics-Finite/dp/0131274988.

Walters, D. Keith, and Davor Cokljat. 2008. "A Three-Equation Eddy-Viscosity Model for Reynolds-Averaged Navier-Stokes Simulations of Transitional Flow." *Journal of Fluids Engineering, Transactions of the ASME* 130 (12): 1214011–114. https://doi.org/10.1115/1.2979230.

Wilcox, David C. 2006. *Turbulence Modeling for CFD*. DCW Industries.

Wilkinson, David L. 1979a. "TWO-DIMENSIONAL BUBBLE PLUMES." *ASCE J Hydraul Div* 105 (2): 139–54. https://doi.org/10.1061/jyceaj.0005151.

———. 1979b. "Two-Dimensional Bubble Plumes." *Journal of the Hydraulics Division* 105 (2): 139–54. https://doi.org/10.1061/JYCEAJ.0005151.

Wörner, M. 2003. "A Compact Introduction to the Numerical Modeling of Multiphase Flows."

Yum, Kyungtaek, Hoon Kim Sung, and Heekyung Park. 2008. "Effects of Plume Spacing and Flowrate on Destratification Efficiency of Air Diffusers." *Water Research* 42 (13): 3249–62. https://doi.org/10.1016/j.watres.2007.06.035.

Zhang, D., N. G. Deen, and J. A.M. Kuipers. 2006. "Numerical Simulation of the Dynamic Flow Behavior in a Bubble Column: A Study of Closures for Turbulence and Interface Forces." *Chemical Engineering Science* 61 (23): 7593–7608. https://doi.org/10.1016/J.CES.2006.08.053.

Zic, K., and H. G. Stefan. 2009. "Lake Aerator Effect on Temperature Stratification

Analyzed by ‘MINLAKE’ Model.” *Http://Dx.Doi.Org/10.1080/07438148809354816* 4 (2): 85–90. https://doi.org/10.1080/07438148809354816.